Interaction of Aerosol, Clouds, and Radiation on the Regional Scale

Zur Erlangung des akademischen Grades eines
DOKTORS DER NATURWISSENSCHAFTEN
der Fakultät für Physik des
Karlsruher Instituts für Technologie (KIT)

genehmigte
DISSERTATION
von

Dipl. Met. Max Jonas Bangert
aus
Eberbach

Tag der mündlichen Prüfung:	27.04.2012
Referent:	Prof. Dr. Christoph Kottmeier
Korreferent:	Prof. Dr. Thomas Leisner

Abstract

The interaction of aerosol particles with clouds still is one of the largest uncertainties in modern climate projection and weather forecast. Depending on their chemical composition and size, atmospheric aerosol particles act as cloud condensation nuclei CCN and ice nuclei IN during cloud formation. They determine the initial size distribution of the cloud droplets and ice crystals. As a consequence, aerosol particles have an impact on the optical properties and microphysical processes of clouds, thus inducing various feedback processes influencing precipitation, radiation, and the state of the atmosphere.

In this thesis, the online-coupled model framework COSMO-ART is extended to investigate the interaction of atmospheric aerosol particles with clouds on the regional scale taking the formation and anthropogenic and natural emission of aerosol particles into account. With the new model version it is possible to simulate the formation of cloud droplets and ice crystals on the basis of the physical and chemical properties of the aerosol particles, as well as the subsequent impact on cloud microphysical processes and optical properties.

The impact of natural and anthropogenic aerosol particles on cloud properties and precipitation is studied and quantified for Western Europe in two case studies, which focus on different aspects of the aerosol-cloud interaction.

In the first study it is shown that the cloud droplet number concentration of clouds is correlated with the structure of the terrain, and a terrain slope parameter TS is presented to classify this dependency, which can be used to improve the parameterization of subgrid-scale updrafts in the activation parameterizations of climate models. It is highlighted that the spatial distributions of clouds and CCN are closely related. High aerosol and CCN number concentrations are found in the vicinity of clouds at high altitudes, where the nucleation of secondary particles is enhanced. The net response of the hourly precipitation rate to changes in the aerosol is quantified for a period of two days. It is shown that changes in the aerosol trigger positive and negative changes in the precipitation rate of almost the same amount with a slight tendency to an increase in

precipitation due to less CCN and vice versa. On the average, clouds with a liquid water path of approximately $0.85\,\mathrm{kg\,m^{-2}}$ are most susceptible to aerosol changes.

In the second study the impact of dust particles on clouds, radiation, and 2-meter temperature is investigated for a Saharan dust event that occurred in Europe in May 2008. The impact of dust particles on liquid clouds is low during the event because of the dominant anthropogenic and sea-salt CCN. Adding a hygroscopic coating to the dust particles lowers the maximum water saturation during cloud formation and, hence, does not increase their impact on liquid clouds significantly. The impact of dust on ice clouds at temperatures below 235 K also is negligible because of the dominant homogeneous freezing of the numerous liquid aerosol particles. The largest impact of dust particles on cloud properties is found in the temperature range between 235 K and 273 K. At these temperatures, the dust particles increase the ice crystal concentration significantly and have an impact on the glaciation of mixed-phase clouds. Consequently, the optical properties of the clouds are modified, which causes a decrease of the incoming shortwave radiation at the surface. As a result, the 2-meter temperatures decrease up to -1 K. It is shown that during the day the difference in the 2-meter temperatures caused by the dust-cloud interaction is comparable in magnitude to the direct impact of dust particles on radiation. The overall impact of the dust on clouds and radiation causes systematically lower 2-meter temperatures of up to -1.8 K in the dust-affected regions in Europe during daytime. At night, the 2-meter temperature is increased in some parts of Europe due to the direct impact of the dust on longwave radiation. It is found that the simulated change in 2-meter temperature due to the interaction of the dust with clouds and radiation can explain a systematic bias in numerical weather forecasts during the period of the dust event.

Contents

1. Introduction

The atmosphere of the Earth is composed of gases and suspended liquid and solid particles with different sizes, shapes, and chemical compositions. The best known particles of the atmosphere are the droplets and crystals of clouds and precipitation, since they can be seen easily by the human eye and experienced daily. Nevertheless, most of the particles in the atmosphere have much smaller sizes and are only perceived occasionally, when the particle concentration is very high. These particles are referred to as atmospheric aerosol particles.

Aerosol particles and clouds are of special interest to mankind, because they govern the atmospheric branch of the hydrological cycle by the formation of precipitation, and on the other hand, they strongly modify the radiation budget of the atmosphere by scattering and absorption of radiation, which has an influence on the overall energy budget of the atmosphere-earth system. As a consequence, anthropogenic and natural changes of the amount, distribution, or properties of aerosol particles and clouds are, regionally and globally, of great social and economic importance.

1.1. Particles in the Atmosphere

Atmospheric aerosol particles have diameters ranging from a few nanometers to several micrometers. Their sources are nucleation from gaseous precursors, which are usually generated by photochemical processes, or direct emissions by anthropogenic activities or by the natural release of particles at the surface. The first group is referred to as secondary aerosol particles and the latter as primary aerosol particles. Primary aerosol particles have diameters in the order of a few micrometers and include, for instance, mineral dust and sea salt particles. Secondary particles usually consist of mixtures of sulfate, ammonium, nitrate, organic matter, and water. Freshly nucleated particles have diameters of a few nanometers but grow by condensation of vapors or by coagulation with other particles to diameters in the order of several hundred nanometers. Particles in

the size range between approximately 0.1 μm and 2 μm have the longest lifetime in the atmosphere in the order of several days, since larger particles sediment rapidly under the influence of gravity.

Aerosol particles can grow by the condensation of water vapor onto the particles. If moist air is supersaturated with respect to water, for example as a result of adiabatic cooling in an updraft, some particles are able to grow quickly to diameters of 10 μm. These particles are then referred to as cloud droplets. Aerosol particles that grow to the size of cloud droplets are termed 'activated' and the corresponding rapid growth of the particles is referred to as 'activation' of the aerosol particles. Whether or not an aerosol particle can be activated depends on its size and chemical composition.

Further growth of cloud droplets is governed by the collision and coalescence of the droplets, since condensational growth of droplets slows down with increasing droplet size. The efficiency of collision and coalescence of droplets strongly depends on their size distribution. During their growth, the fall velocity of the droplets increases and once the droplet exceeds approximately 50 μm in diameter, the updrafts inside the cloud are not sufficient to keep the drops suspended. These large drops will precipitate and reach the surface, unless they fall through subsaturated air and evaporate. They are usually termed raindrops.

At temperatures lower than approximately -35 °C, droplets can freeze spontaneously and form ice crystals. Apart from this so-called homogeneous freezing, ice particles can form at higher temperatures, if solid aerosol particles, e.g. mineral dust or soot particles, initiate the freezing of super-cooled droplets or directly serve as deposition nuclei. These mechanisms are referred to as heterogeneous freezing. Ice particles occur in the atmosphere in various sizes and shapes. Small ice particles with a dimension of less than 5 mm that are grown by the deposition of water vapor are usually termed ice crystals, whereas large precipitating ice particles are referred to as snow, graupel, or hail depending on their size and density. The formation and growth of these large ice particles with sizes from several millimeters up to a few centimeters at the maximum are governed by the collision of ice particles with each other, termed aggregation, as well as by collisions of ice crystals with cloud droplets and raindrops, termed riming.

In short, the formation of aerosol particles, clouds, and precipitation is a sequence of chemical and physical processes involving liquid and solid particles with sizes of several orders of magnitude. As a consequence, aerosol particles, clouds, and precipitation have

to be considered a coupled system to understand their interaction and quantify their potential impact on the state of the atmosphere.

1.2. Aerosol-Cloud Interaction

At the end of the 19th century, Aitken (1880) and Coulier and Mascart (1875) discovered that cloud droplets only form when aerosol particles serve as cloud condensation nuclei, CCN. This was consistent with the finding of Thomson (1871), who showed that the water vapor pressure for which a droplet is in equilibrium with its environment increases massively with decreasing droplet size, causing small droplets to evaporate very quickly. Aitken (1880) also noted that the activation of these particles depends on their chemical composition. He found that natural salts as well as particles produced by burning sulfur, which is the case when burning fossil fuels, are very efficient CCN. As a consequence, he hypothesized that the optical and microphysical properties of fogs and clouds are influenced massively by anthropogenic activities. The theoretical basis of the activation of hygroscopic aerosol particles was derived by Köhler (1936), who described the water vapor pressure at which an solution droplet is in equilibrium with its environment as a function of its size and chemical composition.

Based on the latest findings on droplet nucleation, Wegener (1911) hypothesized that the freezing of water in the atmosphere is also driven by solid particles serving as a nuclei for ice formation. He pointed out that, in contrast to the droplet nucleation, the surface properties of the particles, rather than their chemical composition, determine whether they can act as an ice nuclei IN and hypothesized that dust particles dispersed from the ground are effective ice nuclei, because of their crystalline structure similar to the structure of ice.

Wegener (1911), Bergeron (1935), and Findeisen (1938) postulated that precipitation is produced in a cloud by the efficient growth of ice particles by deposition at the expense of water droplets in the cloud due to the difference in the saturation water vapor pressure over water and ice. Based on their work, first experiments were carried out to modify the properties of clouds and the initiation of precipitation by seeding the cloud with artificial ice nuclei (e.g. silver iodide) from airplanes (Kraus and Squires, 1947).

From atmospheric measurement data, revealing that droplet concentrations in cumuli over the continent and over the ocean vary significantly and that ice-free clouds over

the continent seemed to be inefficient in producing rain, Twomey and Squires (1959) concluded that this is caused by variations in the CCN population. They pointed out that continental clouds exhibit large droplet concentrations, because continents are major sources of CCN and that as a result of the greater number concentrations, the droplets are smaller than in maritime clouds, which in turn may explain why ice-free continental clouds are less efficient in producing rain.

Squires (1958) also hypothesized that the low cloud droplet concentrations over the ocean are partly caused by the presence of giant sea salt particles which inhibit other smaller particles from acting as a CCN by decreasing the maximum water vapor pressure reached during cloud formation. This competition of aerosol particles for water vapor and its impact on the maximum water vapor pressure reached during cloud formation were described theoretically by Twomey (1959) for an ascending isolated air parcel.

With the knowledge of the strong coupling of aerosol particles, clouds, and precipitation, the impact of anthropogenic perturbation of the atmospheric aerosol on weather and global climate moved into the scientific focus. Twomey (1977) pointed out that the increasing pollution of the atmosphere causes an increase in cloud optical thickness (Fig. 1.1) due to the shift of the cloud droplet size distribution towards smaller and more numerous droplets, which has a significant impact on the reflection of solar radiation by thin clouds in particular and might cause an increase of the planetary albedo and, as a consequence, may have a long-term cooling effect on the global climate.

Apart from this change in the cloud optical properties, Albrecht (1989) hypothesized that the impact of aerosol perturbations on warm rain formation affects the low-level cloudiness over the oceans. In detail, he pointed out that an increase in the aerosol concentration causes a reduction in drizzle, which causes the liquid water content of shallow clouds to maintain longer and potentially increases the cloud lifetime (Fig. 1.1). As a consequence, the increase in cloud cover increases the global albedo. In contrast to the enhancement in cloud reflectivity associated with a decrease in droplet size, however, the net effect on global climate is more complicated to estimate, because the budget of terrestrial radiation is also modified by an increase in cloud cover. Nevertheless, the increase in the atmospheric aerosol concentration and its impact on the optical properties and microphysical processes of clouds are expected to cause a net cooling effect, which is assumed to be of the same order of magnitude than the heating effect, caused by the emission of trace gases like CO_2 (Charlson et al., 1992).

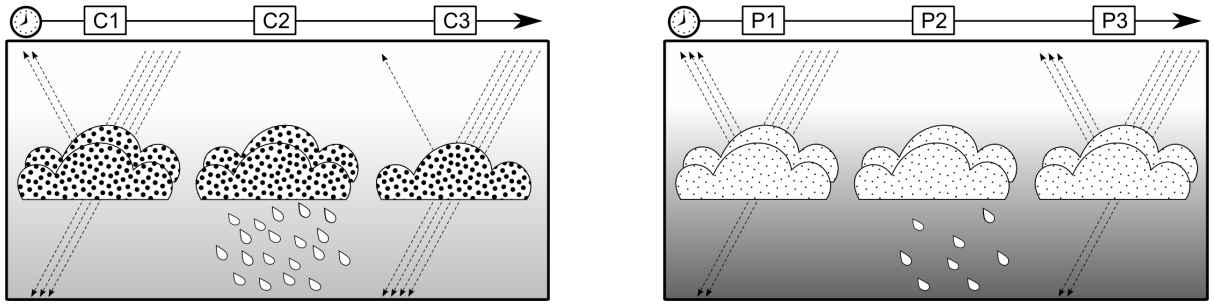

Fig. 1.1.: Illustration of the impact of aerosol particles on clouds as proposed by Twomey (1977) and Albrecht (1989). Initially, the optical thickness and albedo of the clouds are higher for high aerosol concentrations (C1 in comparison to P1) because of the smaller cloud droplets, known as Twomey effect or first indirect aerosol effect. Smaller cloud droplets are less efficient in forming precipitation by collision and coalescence (P2 in comparison to C2). As a result, the cloud cover can be maintained longer, which results in a higher cloud optical thickness and albedo for high aerosol concentrations (P3 in comparison to C3), known as Albrecht effect or second indirect aerosol effect.

1.3. Aerosol-Cloud Interactions in Numerical Atmospheric Models

With the establishment of numerical models as a powerful new tool to solve the three-dimensional equations of hydrodynamics, first attempts were made to consider the impact of the aerosol-cloud interaction on clouds, weather, and climate and to quantify the complex feedback processes.

In numerical model studies difficulties are due to the fact that individual studies can only resolve processes on a specific scale due to the limited availability of computer power. As a consequence, numerical studies have to represent physical processes on smaller scales in terms of admittedly oversimplified parameters and can account for the impact of processes on larger scales only by appropriate boundary conditions. This is a major problem in simulating the aerosol-cloud interaction, because the related processes cover scales from nanometers to kilometers, but are of similar importance to the quantification of the impact on weather and climate.

For this reason, numerical atmospheric models had to focus on individual processes of the aerosol-cloud interaction. Typically, these were either the cloud microphysical processes studied with cloud-resolving models, CRMs, for spatial domains up to a few square kilometers or the impacts on the global radiation budget and consequently climate studied with global circulation models, GCMs. In CRM simulations, the distribution of

aerosol was assumed to be constant within the domain in most studies, which can be justified by the small model domains and short time scales. In GCMs the temporal and spatial variation of the aerosol had to be considered, but GCMs are constrained to very coarse spatial resolutions and simplified representations of the aerosol, the related chemical processes, and the cloud microphysics because of the limited computer resources.

The first studies using GCMs to quantify the radiative impact of the aerosol-cloud interaction on climate revealed a reduction of the net incoming radiation at the top of the atmosphere (defined as negative "radiative forcing") and therefore a cooling effect of the atmosphere-earth system of approximately -1 $\mathrm{W\,m^{-2}}$ (Boucher and Lohmann, 1995, e.g.), but with an uncertainty in the same order of magnitude. In these studies, sulfur was used as a surrogate for atmospheric aerosol and coupled with the cloud droplet number concentration by empirical relations. The treatment of aerosol and clouds improved significantly during the last years, by including more sophisticated cloud microphysics as well as aerosol particles with varying chemical composition and size distribution (Lohmann and Feichter, 2005). Modern GCMs include physically based parameterizations of the aerosol activation (Ghan et al., 2011) and are able to qualitatively capture the response of the average cloud properties of stratiform liquid clouds to variations in the aerosol (Quaas et al., 2009). But even though the spatial resolutions of GCMs improved with the development of modern high-performance computer systems, they are still too coarse to resolve cloud systems and the high variability of the atmospheric aerosol, with typical horizontal resolutions exceeding 100 km. As a result, the uncertainties in the quantification of the climate impact of the aerosol-cloud interaction are still high.

The current estimates of the radiative forcing attributed to individual components of the atmosphere, as presented in the last report of the Intergovernmental Panel on Climate Change (IPCC, 2007), are given in Fig. 1.2. Long-lived greenhouse gases like carbon dioxide and methane have the strongest positive forcing and, hence, a warming effect on climate. Their radiative forcing, which is influenced massively by anthropogenic activities, is well understood and the uncertainties are low in comparison to their magnitude. The radiative forcing related to the interaction of the aerosol with radiation and clouds is estimated to be negative and, hence, has a cooling effect on climate, which partly counteracts the warming effect due to the greenhouse gases. But as stated in the IPCC report (IPCC, 2007), the magnitude of the aerosol effect and especially the interaction with clouds are very uncertain, due to our poor understanding of the complex feed-

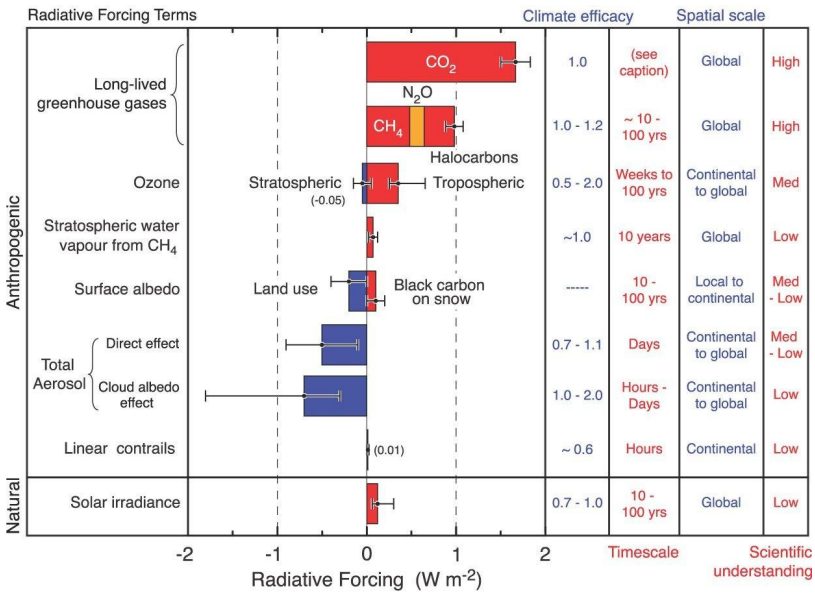

Fig. 1.2.: Global mean radiative forcings of individual components of the atmospheric system from 1750 to 2005 as estimated in the fourth IPCC assessment report (IPCC, 2007). The time scales are estimates for the period of time the radiative forcing would persist after the emissions of the components ceased. For CO_2 no estimate is given. (Taken from IPCC, 2007)

back processes. Consequently, our knowledge of the aerosol-cloud interaction has to be strongly improved to understand and quantify the impact of anthropogenic activities on the Earth's climate.

One reason for our poor understanding of the aerosol-cloud interaction is the variety of cloud types and their complex responses to variations of the aerosol. To improve our understanding of the microphysical processes in clouds and how they respond to aerosol variations, studies using CRMs were carried out. The impact of aerosol changes on the formation of precipitation is one of the most discussed processes (Khain, 2009; Stevens and Feingold, 2009; Small et al., 2009; Levin and Cotton, 2009; Rosenfeld et al., 2008) in the scientific literature. Simulations of single clouds and cloud clusters showed that depending on the cloud type, the influence of aerosol changes on cloud microphysics can affect precipitation amounts very differently, especially in the case of mixed-phase clouds (Khain, 2009, and references therein). Stevens and Feingold (2009) pointed out that the impact of aerosol variation on clouds and precipitations is highly non-linear due to feedback mechanisms with cloud microphysics, cloud dynamics, and the enviroment of the cloud. As a consequence, an increase in the CCN concentration can cause either

an increase or a decrease in the precipitation amount depending on the cloud type and the environmental conditions. Although CRMs are a powerful tool to understand the microphysics and cloud dynamics, they are limited to small domains and short time scales. As a result, some feedback processes with surrounding clouds cannot be considered, which may explain contradictory estimations of the precipitation response to aerosol variations of different CRM studies (Stevens and Feingold, 2009).

1.4. Mesoscale Modeling of Aerosol-Cloud Interactions

Studies using GCMs and CRMs cannot resolve processes on horizontal scales from a few to some hundred kilometers (mesoscale) due to too coarse grid meshes and too small model domains, respectively. This is a major shortcoming with regard to the interaction of aerosol and clouds, because clouds are strongly affected by processes on the mesoscale where the diurnal cycle is the most relevant time scale. There are squall lines, fronts, tropical and extratropical cyclones, and topographically driven processes like mountain waves, and sea and land breezes, for instance. Consequently, these processes have to be considered in numerical studies to improve our understanding of the aerosol-cloud interaction and to quantify the impact of natural and anthropogenic aerosol variations on cloud optical properties and precipitation.

Recent studies demonstrated that mesoscale numerical models can represent the interaction of aerosol particles with clouds and the advantages of their use with different complexities of the aerosol representation. In the studies of Cheng et al. (2007); Ivanova and Leighton (2008); Mühlbauer and Lohmann (2009); Li et al. (2009); and Cheng et al. (2010) aerosol dynamics was accounted for and coupled with cloud microphysics. These studies investigate the impact of different aerosol concentrations defined as initial conditions for the simulations, on the distribution of precipitation for different case studies, but the emission and photochemical formation of aerosol particles are not considered.

The distribution of aerosol particles on the mesoscale is very variable in space and time, due to the very localized sources and the limited lifetime of aerosol particles in the troposphere in the order of hours to days. In addition, spatial distribution of aerosol particles is not independent of the cloud distribution (Engstrom and Ekman, 2010), because both are influenced by the same dynamic features, such as the daily cycle of the boundary layer height and the dynamics associated with front systems or convection. For this

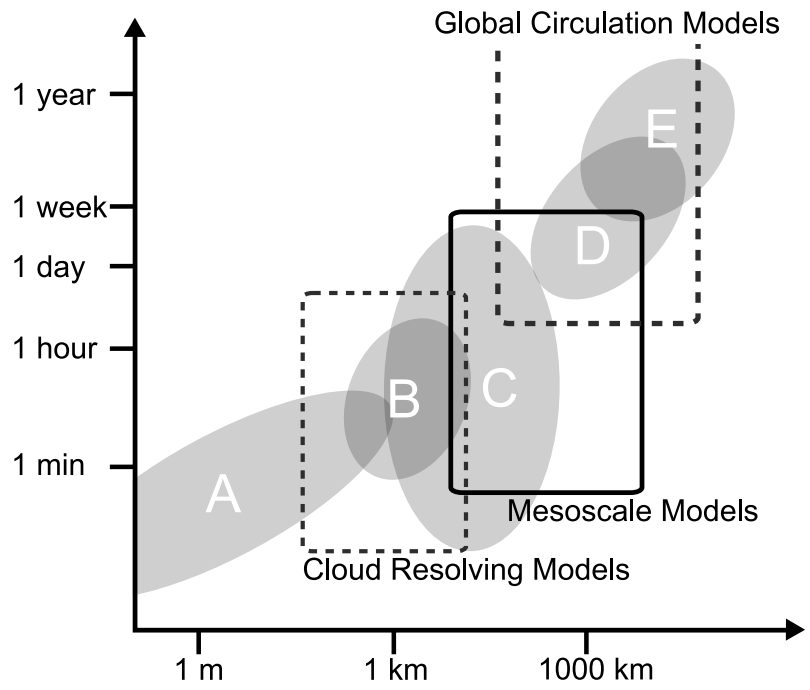

Fig. 1.3.: Scales of atmospheric processes and model systems: A turbulence and single particles; B convection; C mesoscale processes; D lows and highs; E planetary waves. The axes are logarithmic in time [s] and distance [m]. Figure adapted from DWD (2012).

reason, mesoscale models have to explicitly simulate aerosol particles as a prognostic variable on the basis of natural and anthropogenic emissions and, in doing so, can help understand the correlations in the distributions and properties of aerosol particles and clouds.

Solomos et al. (2011) investigated the interaction of sea salt and mineral dust particle emissions with clouds in the south-eastern Mediterranean, photochemical formation of anthropogenic particles was not considered. A simple sulfur cycle using given climatological monthly means of the oxidants producing sulfuric acid, which is able to nucleate aerosol particles or condensate, is treated together with emissions of mineral dust and sea salt by Zubler et al. (2011b,a) in a simulation with a rather coarse horizontal resolution of 50 km to investigate the impact of the anthropogenic increase in the aerosol burden over Europe on a decadal time scale.

The formation and growth of secondary aerosol, which is dominant in the atmosphere in terms of number concentration, strongly depends on gasphase chemical processes, especially on the photochemical production of low-volatile sulfuric acid vapor. Besides sulfuric acid vapor, the growth and chemical composition of aerosol particles depends on

the concentration of gaseous ammonia, nitric acid vapor or semi-volatile organic vapors. As a consequence, a comprehensive treatment of gasphase chemical processes is crucial to the simulation of the atmospheric aerosol distribution, and, since the activation of aerosol particles strongly depends on their size and chemical composition, also to the simulation of the aerosol-cloud interaction.

In contrast to typical air quality applications, the simulation of feedback processes among gases, aerosol particles, clouds, and the state of the atmosphere require an online coupling of the gas-phase and aerosol modules with the meteorological core of the model framework, which means that the prognostic equations of aerosol particles, gases, and hydrometeors are solved in consistency with temperature, pressure, and wind on the same grid within a simulation time step. In general, only a few model systems exist, which fulfill this requirement (Zhang, 2008) and only two are capable of simulating aerosol-cloud interactions (e.g. Ghan et al., 2011).

One model system is an extended version of WRF/CHEM (*W*eather *R*esearch & *F*orecasting Model, including gas phase and aerosol *CHEM*istry) developed by Chapman et al. (2009), who extended the one-moment bulk microphysics scheme by a prognostic treatment of the cloud droplet number concentration and by the mechanistic aerosol activation parameterization of Abdul-Razzak and Ghan (2002). With this model system the interaction of aerosol particles with the liquid cloud phase can be investigated. Based on WRF/CHEM simulation results for the northeastern United States, Ntelekos et al. (2009) pointed out that increasing concentrations of aerosols can lead to either enhancement or suppression of precipitation and that shifts of the rainfall accumulation distribution occur when realistic aerosol, including emissions and chemical reactions, concentrations are included in their simulations. Zhang et al. (2010) studied the chemistry-aerosol-cloud-radiation feedbacks over the continental U.S. in January and July 2001 and detected a slight decrease in precipitation which originated from ice-free clouds. Forkel et al. (2011) studied the response of the chemical composition of the atmosphere to changes in temperature and clouds triggered by the aerosol-cloud-radiation interaction using with WRF/CHEM framework.

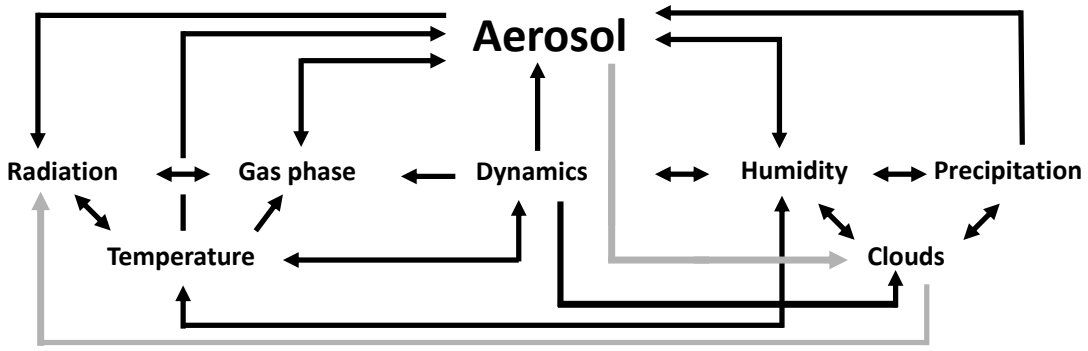

Fig. 1.4.: Feedbacks considered in COSMO-ART. Gray arrows indicate feedbacks introduced in this study.

1.5. The Model Framework Used in This Thesis

In this thesis the regional-scale model system COSMO-ART (*Co*nsortium for *S*mall-scale *Mo*deling – *A*erosols and *R*eactive *T*race gases, Vogel et al., 2009) is used and developed further. COSMO-ART is based on the non-hydrostatic model system COSMO (Baldauf et al., 2011), which is online-coupled with comprehensive modules for the description of gas phase chemistry and aerosol processes. COSMO is used for operational weather forecast by the national weather service of Germany DWD (*D*eutscher *W*etter*D*ienst) and, hence, validated well. COSMO-ART includes parameterizations of the aerosol optical properties and due to online coupling, the model system can be used to study and quantify the feedback processes among atmospheric chemistry, aerosol particles, radiation, and the state of the atmosphere. As a first step towards a representation of the aerosol-cloud interaction in COSMO-ART, Bangert (2008) extended the cloud scheme by prognostic cloud droplet number concentrations and a parameterization of aerosol activation. Vogel et al. (2009) validated the model in terms of the simulated aerosol mass concentration for Europe and quantified the impact of anthropogenic aerosols on atmospheric radiation and temperature. They found a reduction of $6\,\mathrm{W\,m^2}$ in global radiation and a decrease of the 2 m-temperature of 0.1 K for the area of Germany. Studies quantifying the impact of natural aerosol particles on atmospheric radiation and temperature were presented by Stanelle et al. (2010) for dust particles in Africa and Lundgren (2010) for sea salt particles in the Mediterranean. A comprehensive validation of the model system in terms of trace gas concentrations and aerosol chemical composition and size distribution was presented by Knote et al. (2011).

In this thesis the representation of aerosol-cloud interactions in COSMO-ART was developed further by introducing state-of-the-art parameterizations for all processes related to the aerosol-cloud interaction, such as aerosol activation, homogeneous and heterogeneous freezing of aerosol particles, cloud microphysics, and cloud optical properties. Table 1.1 compares the new extended COSMO-ART with two comparable model systems in their most recent versions. To this date, the new COSMO-ART version has provided for the most comprehensive treatment of the chemistry-aerosol-cloud-radiation interaction in a mesoscale model system. It can simulate all components of the atmospheric systems, including gases, aerosol particles, and cloud hydrometeors as well as their interactions with a comparable level of complexity. A simplified overview of the feedbacks considered in COSMO-ART is given in Fig. 1.4.

1.6. Objectives of this Thesis

In this thesis the new extended model version of COSMO-ART is introduced and used to answer scientific questions arising from our current knowledge of the aerosol-cloud interaction.

The activation of soluble inorganic aerosol particles to cloud droplets is understood well and can be described by the classical Köhler equations (Köhler, 1936). The activation of particles with a significant organic fraction is not yet described well, mainly because organic aerosol is hard to characterize (Jimenez et al., 2009). The activation of insoluble particles like dust and soot particles was neglected for a long time in atmospheric studies, but can be described by novel approaches (Kumar et al., 2009). If the size distribution and properties of the aerosol particles are known, the corresponding cloud droplet number concentrations observed at the cloud base can be predicted well, as shown by detailed in-situ aircraft measurements (Fountoukis et al., 2007).

Although homogeneous and heterogeneous freezing of aerosol particles can be described theoretically by using classical nucleation theory (Pruppacher and Klett, 1997), many parameters are uncertain or unknown. Parameterizations based on lab or field measurement studies are used to describe these processes with empirical relationships in atmospheric models (e.g. Phillips et al., 2008; Koop et al., 2000; Lohmann and Diehl, 2006; Hoose et al., 2008; Storelvmo et al., 2008) and few are based on nucleation theory (e.g. Hoose et al., 2010b). The most important IN in the atmosphere are mineral dust

Tab. 1.1.: State-of-the-art online-coupled mesoscale model systems, including the treatment of chemistry-aerosol-cloud interactions. Mechanistic parameterizations are based on a solution of the saturation equation during activation and ice nucleation.

	COSMO-ART	WRF/CHEM	COSMO-M7
particulate phase			
aerosol module	$MADE_{soot}^{extended}$	MOSAIC	M7
size distribution	MODAL	BIN	MODAL
sulfate	•	•	•
ammonium	•	•	
nitrate	•	•	
organics	•	•	
soot	•	•	•
sea salt	•		•
mineral dust	•		•
number of modes/bins	11	8	7
gas phase			
gas phase	RADMKA	CBM-Z	sulfur cycle
prognostic species	60	52	3
representation of aerosol-cloud interaction			
cloud droplets	two-moment	two-moment	two-moment
activation	mechanistic	mechanistic	empirical
ice crystals	two-moment	one-moment	two-moment
ice nucleation	mechanistic	(not coupled)	empirical
aerosol ↔ liquid clouds	•	•	•
aerosol ↔ ice clouds	•		•
drop size ↔ radiation	•	•	•
crystal size ↔ radiation	•		•
reference	This study	Zhang et al. (2010)	Zubler et al. (2011b)

particles, because of their efficient ice-nucleating ability and high number concentrations (Field et al., 2006; Möhler et al., 2006; Hoose et al., 2008). Other IN in the atmosphere are biological particles, which are very efficient, but occur in low number concentrations compared to other IN (Hoose et al., 2010a), and soot particles, which are less efficient, but may reach high number concentrations in the atmosphere (DeMott, 1990; Möhler et al., 2005). Due to the different freezing mechanisms, the variety of aerosol properties, and the potential effect of soluble coatings, quantitative description of homogeneous and heterogeneous freezing in the atmosphere still is uncertain and subject to current research.

Observations of the aerosol-cloud interaction are limited to well-defined cloud systems, especially stratiform clouds in the pacific. They show that there is a significant correlation of aerosol concentration and droplet concentration at the cloud base (Twohy et al., 2005). An in-situ measurement of the aerosol impact on cloud optical properties is challenging because of the complex feedback processes with cloud microphysics, cloud dynamics, and the environment, see Twohy et al. (e.g. 2005); Roberts et al. (e.g. 2008). As discussed by Koren et al. (2010), quantifying the aerosol-cloud interaction with satellites is challenging, because clouds and aerosol properties cannot be measured at the same point and numerous artefacts affect the retrieval of their properties. Additionally, the distributions of clouds and aerosol particles are not independent, since they both are influenced by atmospheric dynamics, humidity, and temperature (Engstrom and Ekman, 2010). Understanding the correlation of the cloud and aerosol distribution is crucial to the interpretation of satellite-derived measurements of the aerosol-cloud interaction.

The current estimate of the contribution of aerosol-cloud interaction to global radiative forcing derived with GCM simulations is $-0.7 \pm 0.4\,\mathrm{W\,m^{-2}}$ (Quaas et al., 2009). Recent mesoscale simulations highlighted the strong variability of the response of cloud optical depth to CCN variations (Zhang et al., 2010; Chapman et al., 2009). The impact of increased IN concentrations on cloud properties and the radiation budget is uncertain. An increase in IN concentration is assumed to decrease the lifetime of mixed-phase clouds due to more intense precipitation triggered by the effective glaciation of the clouds (e,g, Lohmann and Hoose, 2009), whereas measurements in regions with abundant mineral dust particles showed that mineral dust significantly increases the ice crystal number concentration, the consequence being a decreasing precipitation rate (Min et al., 2009). Long-term lidar measurements showed that in the presence of high mineral

dust concentrations, the amount of ice-containing clouds is 30 % higher at temperatures between −10 °C and −20 °C (Seifert et al., 2010). The impact of aerosol particles on ice clouds forming at temperatures lower than −35 °C depends on the competition of heterogeneous freezing involving IN with homogeneous freezing of liquid aerosol particles. Depending on the updraft velocities, an increase in IN may therefore also decrease the ice crystal number by inhibiting homogeneous freezing (Barahona et al., 2010a).

Understanding and quantifying the impact of aerosol variations on precipitation still are challenging tasks of current research. Depending on cloud type and atmospheric conditions, an increase in CCN may increase or decrease the precipitation amount in single clouds, as shown in numerous CRM studies (e.g. Khain et al., 2008; Khain, 2009). Ice-free clouds tend to produce less precipitation, if the aerosol concentration is increased, whereas the precipitation amount produced by convective mixed-phase clouds tends to increase due to an invigoration of the cloud dynamics (e.g. Rosenfeld et al., 2008; Seifert and Beheng, 2006a). The development of mixed-phase clouds is susceptible to the IN number concentration. An increase in efficient IN can cause an effective glaciation of the mixed-phase clouds and potentially increase precipitation (Lohmann and Hoose, 2009). On the contrary, further increase in IN will result in smaller ice crystals that fall more slowly. Consequently, the formation of precipitation is less effective (Lebo and Seinfeld, 2011).

In summary, the aerosol-cloud-precipitation-radiation interaction still is far from being understood because of the numerous feedback processes involved (IPCC, 2007; Stevens and Feingold, 2009).

With COSMO-ART, the properties and spatial and temporal distributions of atmospheric aerosol particles can be simulated on the basis of secondary formation as well as anthropogenic and natural emissions without needing given distributions of gaseous precursors or particles. As a consequence, feedback processes related to the chemistry-aerosol-cloud-radiation interactions can be simulated on the regional scale, which allows to improve our understanding of the aerosol-cloud interaction. Based on our current knowledge of the aerosol-cloud interaction, different questions are addressed.
Understanding the correlation of the aerosol and cloud distribution is indispensable for quantifying the aerosol-cloud interaction with measurements.

- Are there systematic patterns in the distributions of aerosol number and mass concentration as well as cloud droplet number concentration? Are there close links between them?

- Is there a relation among the aerosol, topography, and cloud droplet number concentrations?

The impact of aerosol on cloud microphysics can affect precipitation amounts very differently, especially in the case of mixed-phase clouds as shown by numerous studies.

- How are precipitation patterns altered when the interaction of aerosol particles and cloud processes is taken into account on the regional scale? Are there any systematic effects?

Global and regional climate studies as well as satellite observations showed that aerosol particles have an effect on the global statistics of cloud properties with consequences for the global energy budget of the atmosphere-earth system.

- Is there any significant aerosol impact on cloud properties and the radiation budget on short time scales, especially during extraordinary aerosol events like dust storms?

- How strong is the impact of Saharan dust events on the 2-meter temperature and the state of the atmosphere over Europe? Are there consequences for operational weather forecast?

In the following sections the basic physical concepts of the aerosol-cloud interaction will be discussed and implementation of these processes in the model framework COSMO-ART will be presented. Finally, the scientific questions will be discussed based on two case studies.

2. Theory of the Aerosol-Cloud Interaction

The interaction of aerosol particles and clouds involve processes on multiple scales. They range from the nucleation of liquid and solid particles on the scale of just a few nanometer to the growth of droplets on the scale of several micrometers up to the dynamics of cloud systems and the hydrological cycle on the scale of several kilometers.

In the following, the basic theoretical concepts describing the interaction of aerosol particles and clouds are introduced.

2.1. Formation of Hydrometeors in the Atmosphere

To understand why aerosol particles are most important for the formation of clouds in the atmosphere, one has to understand the formation of hydrometeors in the atmosphere in general. The nucleation and growth of a liquid or solid particle in the atmosphere can be described by thermodynamic theory.

The thermodynamic state of a system can be defined by one of its thermodynamic potentials. In the following we will use the Gibbs free energy G, which is commonly used to describe the thermodynamics of phase changes. For a mixture of n components G is given by

$$G = \sum_{l=1}^{n} \mu_l n_l, \qquad [2.1]$$

where μ_l is the chemical potential and n_l is the number of moles of component l.

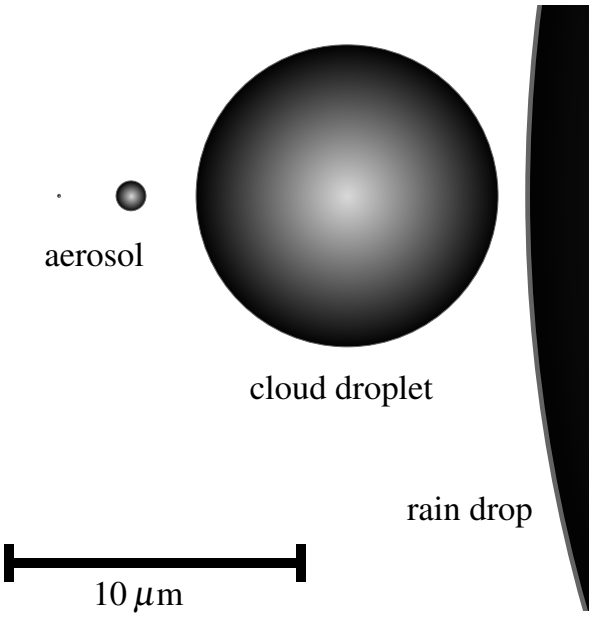

Fig. 2.1.: Growth from aerosol to rain drop

2.1.1. Gibbs Free Energy Change of Droplet Formation

The formation of a pure water droplet, index $_d$, from water vapor, index $_v$ is accompanied by a change in G:

$$\begin{aligned} \Delta G &= G_d - G_v \\ &= \mu_w n_w + \mu_v (n_t - n_w) + \pi D^2 \sigma_{v,w} - \mu_v n_t \\ &= (\mu_w - \mu_v) n_w + \pi D^2 \sigma_{v,w}, \end{aligned} \qquad [2.2]$$

where n_t is the total number of moles in the system and D is the diameter of the droplet. We introduced the term $\pi D^2 \sigma_{v,w}$, which is the free energy associated with the interface between the droplet and the water vapor, where $\sigma_{v,w}$ is the surface tension of the water-water vapor interface, index $_{v,w}$, and represents the amount of energy needed to increase the surface by one unit area. Assuming that water vapor is an ideal gas, μ_v can be expressed as a function of the water vapor pressure e (Seinfeld and Pandis, 2006, p. 442)

$$\mu_v = \mu_v^{\diamond} + RT \ln \frac{e}{e^{\diamond}}, \qquad [2.3]$$

where R is the universal Gas constant, T is the temperature and $\mu_v^\diamond$ is the standard chemical potential defined at $e^\diamond = 1013.25\,\text{hPa}$. The difference in the chemical potential between the liquid water and the water vapor can be derived by (Fletcher et al., 1962)

$$\mu_w - \mu_v = \mu_v(e^\circ) - \mu_v(e) = -RT \ln \frac{e}{e^\circ}, \qquad [2.4]$$

where e° is the water vapor pressure in chemical equilibrium with the water surface. The ratio e/e° defines the saturation ratio S

$$S = \frac{e}{e^\circ}. \qquad [2.5]$$

For $S = 1$ the water vapor is in chemical equilibrium ($\mu_v = \mu_w$) with the water surface.

We can write n_w in Eq. 2.2 as a function of D

$$n_w = \frac{\rho_w \pi D^3}{6 M_w}, \qquad [2.6]$$

where ρ_w is the density of water and M_w is the molar mass of water. Substituting Eq. 2.4 and Eq. 2.6 in Eq. 2.2 we obtain the following expression of the Gibbs free energy change

$$\Delta G = -\frac{1}{6}\pi D^3 \frac{\rho_w RT}{M_w} \ln S + \pi D^2 \sigma_{v,w} \qquad [2.7]$$

Figure 4.2 shows the behavior of ΔG as a function of D for different values of S. For $S < 1$, ΔG is always positive, but for $S > 1$ a maximum ΔG exists. The diameter D^*corresponding to the maximum can be calculated by $d\Delta G/dD = 0$ and we get

$$D^* = \frac{4\sigma_{v,w} M_w}{RT\rho_w \ln S}. \qquad [2.8]$$

The second law of thermodynamics states that a system at constant pressure and temperature tends to decrease G by irreversible processes until a minimum G is reached. At the minimum G the system is in a stable thermodynamical equilibrium. A particle in thermodynamic equilibrium with its surrounding mother phase will not grow or shrink, as the net fluxes of matter and energy at the particle surface are zero. In case of ΔG accompanied with the formation of a droplet with diameter D we have a maximum in G ($G = G_0 + \Delta G$, where G_0 is the Gibbs free energy before the droplet formation) for $S > 1$ at $D = D^*$. At this point the droplet is in a metastable thermodynamical equilibrium ($dG/dD = 0$). Small changes in D will either cause the droplet to grow in case of a small increase in D (e.g. because of a collision with a molecule) or shrink in case of

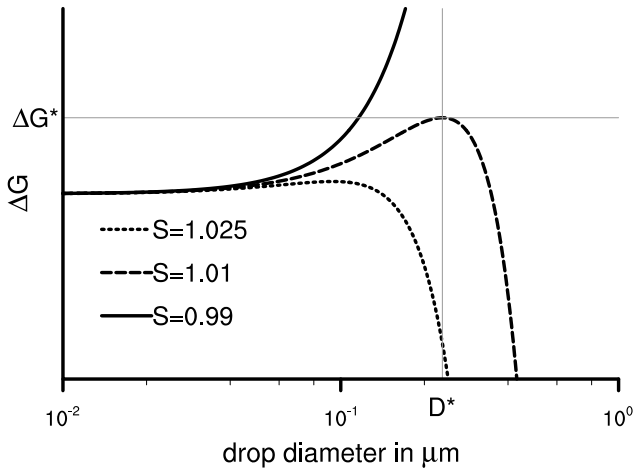

Fig. 2.2.: Change in Gibbs free energy for the formation of droplets as a function of drop diameter for three different saturation ratios calculated with Eq. 2.7.

a small decrease in D. For $S < 1$ the droplet will always shrink, decrease G, until it is completely evaporated.

Rearranging Eq. 2.8, the equilibrium saturation ratio S_{eq} of a pure water droplet can be expressed as a function of its diameter D:

$$S_{\mathrm{eq}} = \frac{e_{\mathrm{eq}}}{e^{\circ}} = e^{\frac{4\sigma_{v,w}M_w}{RT\rho_w D}}, \qquad [2.9]$$

which is known as the Kelvin equation. In equilibrium the water vapor pressure e_{eq} over a curved interface always exceeds the vapor pressure over a flat surface e°.

2.1.2. Classical Nucleation Theory

Even though the nucleation of droplets and particles depends on the collision and cluster formation of a few molecules, one can use thermodynamic (macrophysical) arguments to describe the conditions for the formation of stable nuclei. The initial cluster size has to exceed the critical diameter D^* to grow further, otherwise the cluster will shrink again. To form a cluster of size D^* the energy $\Delta G(D^*) = \Delta G^*$ is needed. The height of this energy barrier can be calculated by substituting Eq. 2.8 in Eq. 2.7:

$$\begin{aligned} \Delta G^*_{w,v} &= \tfrac{16}{3}\pi \frac{\sigma^3_{v,w}M^2_w}{(RT\rho_w \ln S)^2}, \\ &= \tfrac{1}{3}\pi D^{*2}\sigma_{v,w} \end{aligned} \qquad [2.10]$$

We see that for increasing S the energy barrier and the critical diameter decreases. To derive the nucleation rate, we need to know the number concentration of molecule clus-

ters $N^e_{w/v}$, which are in a metastable equilibrium ($\Delta G_{w/v}$ equals $\Delta G^*_{w/v}$). If we assume a constrained equilibrium of the clusters within the vapor, their distribution obeys the Boltzmann distribution (Fletcher et al., 1962) and we get

$$N^e_{w/v} = \dot{N} \exp\left(-\frac{\Delta G^*_{w/v}}{kT}\right), \qquad [2.11]$$

where $\dot{N}$ is the total number concentration of molecules in the system and k is the Boltzmann constant. The nucleation rate per unit time and per unit volume J_w is determined by the rate by which molecules collide with the surface of the critical clusters (Pruppacher and Klett, 1997, p. 199ff)

$$\begin{aligned} J_w &= \beta_{w/v} Z_{w/v} \pi D^{*2} N^e_{w/v}, \\ &= \beta_{w/v} Z_{w/v} \pi D^{*2} \dot{N} \exp\left(-\tfrac{\Delta G^*_{w/v}}{kT}\right), \end{aligned} \qquad [2.12]$$

where $\beta_{w/v}$ is the rate at which a critical cluster gains a molecule by collision with the vapor molecules and $Z_{w/v}$ is the Zeldovich factor, which accounts for deviations from the assumed equilibrium cluster concentration and the loss of molecules from the clusters. For an ideal gas $\beta_{w/v}$ is given by (Pruppacher and Klett, 1997, p. 163)

$$\beta_{w/v} = \frac{e}{(2\pi \dot{m} kT)^{1/2}}. \qquad [2.13]$$

where mi_w is the mass of a single water molecule. This derivation of the nucleation rate is commonly referred to as classical nucleation theory, CNT. One should note that even though the derivation is shown for the homogeneous nucleation of a water droplet , the derivation holds for the nucleation of ice in water vapor by replacing the properties of water with the corresponding properties of ice in Eq. 2.2 to Eq. 2.13 and assuming a spherical shape of the nucleated crystals.

Nucleation rates for a pure water droplet and ice crystal calculated with CNT are given in Table 2.1. Even if S is unrealistic high compared to conditions in the atmosphere the nucleation rates of pure ice and water are negligible. Therefore, the formation of hydrometeors in the atmosphere requires the nucleation and growth of aerosol particles, which contain other substances that nucleate more efficiently under atmospheric conditions. The main contributor to particle nucleation in the atmosphere is sulfuric acid vapor (Seinfeld and Pandis, 2006, p. 520). Even for small amounts of sulfuric acid vapor and $S < 1$, nucleation of sulfuric acid droplets is induced in the atmosphere.

Tab. 2.1.: Nucleation rates of ice and water at a temperature of -12° C and $S = 2$ (Pruppacher and Klett, 1997, p. 203)

J_w	$1.9e^{-112}\,\mathrm{cm}^{-3}\,\mathrm{s}^{-1}$
J_i	$9.2e^{-394}\,\mathrm{cm}^{-3}\,\mathrm{s}^{-1}$

2.2. Diffusional Growth of Aerosol Particles

The diffusional growth of an aerosol droplet depends if the droplet is in thermodynamic equilibrium with the surrounding humid air or not and can be calculated by (Pruppacher and Klett, 1997, p. 511):

$$\frac{dD}{dt} = \frac{\Lambda}{D}(S - S_{\mathrm{eq}}), \qquad [2.14]$$

$$\text{where} \qquad \Lambda = 4\left(\frac{\rho_w RT}{e^{\circ} D'_v M_w} + \frac{l_{w,v}\rho_w}{k_a T}\left(\frac{l_{w,v} M_w}{TR} - 1\right)\right)^{-1}, \qquad [2.15]$$

k_a is the thermal conductivity of air and $l_{w,v}$ is the latent heat of evaporation. The diffusivity of water vapor in air onto the droplet D'_v depends on the size of the droplet and can be calculated by (Fukuta and Walter, 1970)

$$D'_v = \frac{D_v}{1 + \frac{2D_v}{\alpha_c D}\sqrt{\frac{2\pi M_w}{RT}}}, \qquad [2.16]$$

where D_v is the diffusivity of water vapor in air neglecting non-continuum effects and α_c is the accommodation coefficient that expresses the probability of a water vapor molecule remaining in the liquid phase upon collision (Seinfeld and Pandis, 2006, p. 546). If $S > S_{\mathrm{eq}}$ the droplet will grow by condensation of water vapor and if $S < S_{\mathrm{eq}}$ the droplet will shrink by evaporation until $S = S_{\mathrm{eq}}$. To calculate the growth of a specific aerosol particle both S and S_{eq} have to be know.

2.2.1. Equilibrium Saturation Ratio of a Solution Droplet

For conditions of thermodynamic equilibrium the water vapor pressure surrounding a pure liquid water droplet is given by the Kelvin equation Eq. 2.9. For a solution droplet we can replace e° with its equivalent over the solution e_s° to derive the equilibrium water vapor pressure of a solution droplet

$$e_{\mathrm{eq}} = e_s^{\circ} \exp\left(\frac{4\sigma_{v,w} M_w}{RT\rho_w D}\right). \qquad [2.17]$$

Applying Raoult's law we can determine the water vapor pressure over a flat solution surface e_s° as a function of e°

$$e_s^\circ = e^\circ x_w, \tag{2.18}$$

where x_w is the mole fraction of water in the solution:

$$x_w = \frac{n_w}{n_w + n_s}. \tag{2.19}$$

Here, n_w is the number of moles of water and n_s the number of moles of the solute. If Equation 2.18 is valid, the solution is termed ideal. In a non-ideal solution an effective mole fraction of water has to be used, which is called the water activity α_w of the solution

$$e_s^\circ = e^\circ \alpha_w. \tag{2.20}$$

Now we can combine the equations 2.17 and 2.18 and get

$$S_{\mathrm{eq}} = \frac{e_{\mathrm{eq}}}{e^\circ} = \alpha_w \exp\left(\frac{4\sigma_{v,w} M_w}{RT\rho_w D}\right). \tag{2.21}$$

To calculate S_{eq} one has to determine α_w. For an ideal solution α_w equals x_w. Combining the volume of the solution droplet

$$\frac{1}{6}\pi D^3 = n_w \upsilon_w + n_s \upsilon_s, \tag{2.22}$$

where υ_w and υ_s are the mole volumes of water and of the solute, and the definition of x_w (Eq. 2.19) we get

$$\frac{1}{x_w} = 1 + \frac{n_s \upsilon_w}{1/6\pi D^3 - n_s \upsilon_s}. \tag{2.23}$$

Assuming that the solution is dilute $1/6\pi D^3 \gg n_s \upsilon_s$ and using $\upsilon_w = M_w/\rho_w$, we get

$$\ln S_{\mathrm{eq}} = \frac{4\sigma_{v,w} M_w}{RT\rho_w D} - \frac{6 n_s M_w}{\rho_w \pi D^3}, \tag{2.24}$$

where we made use of $\ln(1+y) \approx y$ for $y \to 0$. Equation 2.24 is known as the Köhler equation. We can express n_s by the properties of the dissolved dry aerosol particle in the solution droplet by

$$n_s = \frac{\nu_s \pi D_p^3 \rho_s}{6 M_s}, \tag{2.25}$$

where ν_s is the dissociation factor of the solute, D_p is the dry diameter of the dissolved particle, and ρ_s is the density of the solute. Because inside a cloud the ambient saturation

ratio is very close to 1, we can replace $\ln S_{\mathrm{eq}}$ with the supersaturation s_{eq} which is defined as

$$s_{\mathrm{eq}} = S_{\mathrm{eq}} - 1 = \frac{e_{\mathrm{eq}}}{e^{\circ}} - 1 \approx \ln S_{\mathrm{eq}} \qquad [2.26]$$

and formulate the most common version of the Köhler equation:

$$s_{\mathrm{eq}} = \frac{A}{D} - \frac{B}{D^3}, \qquad [2.27]$$

$$\text{where} \qquad A = \frac{4\sigma_{v,w} M_w}{RT\rho_w} \qquad \text{and} \qquad B = \frac{\nu_s D_p^3 \rho_s M_w}{\rho_w M_s}. \qquad [2.28]$$

2.2.2. Equilibrium Saturation Ratio of a Solid Aerosol Particle

The equilibrium saturation ratio of an aerosol particle is given by Eq. 2.21. In case of a soluble aerosol particles α_w in Eq. 2.21 can be expressed by the mole fraction of water in the solution droplet, which results in the Köhler equations (Eq. 2.24 and Eq. 2.27). For insoluble particles, e.g. dust, this classical theory can not be applied, because S_{eq} is now affected by another physical process namely the process of physisorption of water vapor on the particle surface (Kumar et al., 2009). In this case α_w can be determined by FHH (Frenkel, Halsey, and Hill) adsorption theory (e.g. Lowell et al., 2004)

$$\alpha_w = \exp\left(-A_{\mathrm{FHH}} \Theta^{-B_{\mathrm{FHH}}}\right), \qquad [2.29]$$

where A_{FHH} and B_{FHH} are empirical constants, and Θ is the surface coverage (defined as the number of adsorbed layers of water molecules). A_{FHH} characterizes interactions of adsorbed molecules with the aerosol surface and adjacent adsorbate molecules (i.e., those in the first monolayer). B_{FHH} characterizes the attraction between the aerosol surface and the adsorbate in subsequent layers; the smaller the value of B_{FHH}, the greater the distance at which the attractive forces act (Sorjamaa and Laaksonen, 2007). A_{FHH} and B_{FHH} are compound-specific and determined experimentally. We can calculate Θ by

$$\Theta = \frac{D - D_p}{\hat{D}_w}, \qquad [2.30]$$

where $\hat{D}_w$ is the diameter of a water molecule adsorbed at the particle surface (Kumar et al., 2009). Substituting Eq. 2.30 and Eq. 2.29 in the equation for S_{eq} (Eq. 2.21), gives

$$s_{\mathrm{eq}} = \frac{4\sigma_{v,w} M_w}{RT\rho_w D} - A_{\mathrm{FHH}} \left(\frac{D - D_p}{\hat{D}_w}\right)^{-B_{\mathrm{FHH}}}, \qquad [2.31]$$

where we made us of $s_{\mathrm{eq}} \approx \ln S_{\mathrm{eq}}$.

Solid particles can potentially get hygroscopic coatings due to the condensation of gaseous compounds (e.g. sulfuric acid vapor), chemical reactions at their surface, or collision and coalescence with a droplet containing solutes (e.g. in a cloud). This so-called aging of solid particles in the atmosphere decreases the supersaturation needed for their activation. For thin coating the effect of adsorption on s_{eq} has to be considered together with the effect of the solute. Kumar et al. (2011) presented a unified approach combining Köhler with FHH theory in the calculation of the water activity:

$$\alpha_w = x_w \exp\left(-A_{\mathrm{FHH}}\left(\frac{D-\varepsilon_i^{1/3}D_p}{\hat{D}_w}\right)^{-B_{\mathrm{FHH}}}\right), \qquad [2.32]$$

where $\varepsilon_i = V_i/V_p$ is the insoluble volume fraction of the particle with V_p being the total particle volume and with V_i being the volume of the insoluble part. Substituting Eq. 2.32 in Eq. 2.21 using the definition of x_w (Eq. 2.19) we get an equation for s_{eq} combining Köhler and FHH theory:

$$s_{\mathrm{eq}} = \frac{4\sigma_{v,w}M_w}{RT\rho_w D} - \frac{\nu_s\varepsilon_s D_p^3\rho_s M_w}{\rho_w M_s(D^3-\varepsilon_i D_p^3)} - A_{\mathrm{FHH}}\left(\frac{D-\varepsilon_i^{1/3}D_p}{\hat{D}_w}\right)^{-B_{\mathrm{FHH}}}, \qquad [2.33]$$

where $\varepsilon_s = 1-\varepsilon_i$ is the soluble volume fraction of the particle. Note that, in contrast to the derivation of Eq. 2.27, the volume of the particle that is incorporated into the droplet was not neglected.

2.2.3. The Concept of Activation

For a given supersaturation s of the ambient air, the diffusional growth of soluble or solid aerosol particles can be calculated by Eq. 2.14 using Eq. 2.27, Eq. 2.31, and Eq. 2.33 to determine s_{eq} of the different particles. In Figure 2.2.3 the evolution of s_{eq} with droplet diameter is shown for different initial dry aerosol particles sizes. The maximum of s_{eq} is called the critical supersaturation s_{crit} of the aerosol particle. If s is lower than s_{crit} the droplet can grow only until $s = s_{\mathrm{eq}}$ (Eq. 2.14) is reached. If s is greater than s_{crit} the droplet will grow and s_{eq} can reach s_{crit}. During the further growth s_{eq} will decrease (Eq. 2.27, Eq. 2.31, and Eq. 2.33) and as a result cause a continuous and accelerating growth of the droplet (Eq. 2.14). Because the aerosol droplet will grow fast to the size of a cloud drop when s_{eq} reaches s_{crit}, the aerosol droplet is called activated.

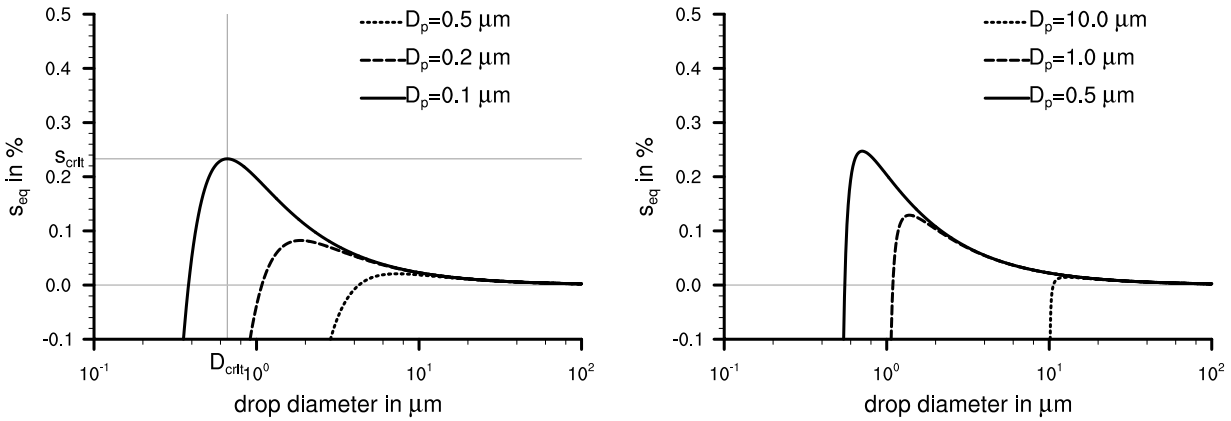

Fig. 2.3.: Equilibrium supersaturation for droplets containing dissolved sulfur particles (left) and solid mineral dust particles (right) with different dry diameters calculated with Eq. 2.27 and Eq. 2.31 respectively

The corresponding processes is referred to as the 'activation' of the aerosol particle. The value of s_{crit} is a function of the properties of the initial dry aerosol particle and can be determined for a soluble particle by the maximum ($ds_{\text{eq}}/dD = 0$) of the Köhler equation (Eq. 2.27):

$$s_{\text{crit}} = \left(\frac{4A^3}{27B}\right)^{1/2} = \left(\frac{4A^3\rho_w M_s}{27\nu_s\rho_s M_w D_p^3}\right)^{1/2}. \qquad [2.34]$$

We see that s_{crit} is independent of the wet droplet diameter D and a function of the chemical properties and the size of the dissolved dry aerosol particle. For increasing D_p, s_{crit} decreases. The corresponding droplet diameter at s_{crit} is given by substituting Eq. 2.34 in Eq. 2.27:

$$D_{\text{crit}} = \frac{2A}{3s_{\text{crit}}}, \qquad [2.35]$$

where $D_{\text{crit}} = D(s_{\text{crit}})$ is the critical droplet diameter for activation. The aerosol droplet has to grow to the size of D_{crit} to get activated. One should note that usually aerosol activation is treated as an instantaneous process, assuming that the aerosol particles have sufficient time to grow to D_{crit}, when s is larger than s_{crit}. In case of very large aerosol particles this assumption can cause errors in the calculation of activation, since the particle growth is proportional to D^{-1} (Eq. 2.14), which means they grow too slowly to reach D_{crit} during the typical time when s exceeds s_{crit}. Such mass transfer limitations on the growth rate, which cause deviations from the assumption of instantaneous activation, are referred to as kinetic limitations (Nenes et al., 2001).

For insoluble solid particles a similar relationship of s_{crit} and D_p can be derived based on Eq. 2.31 of the FHH activation theory or Eq. 2.33 in case of solid particles with a soluble coating. In contrast to soluble particles, the maxima of Eq. 2.31 and Eq. 2.33 have to be calculated numerically to derive s_{crit}. Kumar et al. (2009) suggested that s_{crit} for solid particles can be written analogous to Eq. 2.34 in the form

$$s_{\text{crit}} = CD_p^c, \qquad [2.36]$$

where c and C are constants depending on A_{FHH} and B_{FHH} (see Eq. 4.5 and Eq. 4.6).

If the chemical composition of a given aerosol number density size distribution $n_N(D_p)$ does not vary with size, a corresponding number density distribution $n_N^*(s_{\text{crit}})$ in supersaturation space can be derived, because D_p is proportional to s_{crit}:

$$n_N^*(s_{\text{crit}}) = \frac{dN}{ds_{\text{crit}}} = \frac{dN}{dD_p}\frac{dD_p}{ds_{\text{crit}}} = n_N(D_p)\left(\frac{1}{c}\right)\frac{D_p}{s_{\text{crit}}}, \qquad [2.37]$$

where c is the exponent in Eq. 2.36 and equals $-3/2$ for hygroscopic particles (Eq. 2.34). For a given s, all particles with $s_{\text{crit}} \leq s$ will get activated (neglecting kinetic limitations). Thus, the total number of activated particles as a function of s is given by

$$\text{CCN}(s) = \int_0^s n_N^*(s')\,ds', \qquad [2.38]$$

which is commonly referred to as the CCN spectrum of an aerosol population. The number concentration of cloud droplets formed during cloud formation is therefore determined by $\text{CCN}(s_{\text{max}})$, where s_{max} is the maximum supersaturation that occurs.

2.2.4. Calculation of Supersaturation in an Ascending Air Parcel

During the formation of a cloud s is mainly determined by the adiabatic cooling rate, which causes an increase in s, and the condensation of water, which causes a decrease in s. These two processes counteract each other and determine the variation of s in time. Neglecting mixing processes with the environment and diabetic cooling, the variation of s in time is given by (Seinfeld and Pandis, 2006, p. 789)

$$\frac{ds}{dt} = \alpha w - \frac{\gamma}{\rho_a}\frac{dm_c}{dt} \qquad [2.39]$$

for an ascending air parcel, where αw is the contribution with respect to the adiabatic cooling of the ascending air parcel and $\frac{\gamma}{\rho_a}\frac{dm_c}{dt}$ is the contribution with respect to the

condensation rate of water in the parcel. m_c is the mass concentration of cloud water, and w is the vertical velocity of the parcel. The factors α and γ depend on pressure, temperature, and physical constants only and are given by (Seinfeld and Pandis, 2006, p. 789)

$$\alpha = \frac{l_{wv} M_w g}{c_p R T^2} - \frac{g M_a}{R T} \qquad [2.40]$$

and

$$\gamma = \frac{p M_a}{e^\circ M_w} + \frac{l_{wv}^2 M_w}{c_p R T^2}, \qquad [2.41]$$

where g is the gravitational acceleration, M_a is the molar mass of air, and c_p the specific heat capacity of air at constant pressure. One should note, that for the derivation of Eq. 2.39 it was assumed that $S = 1 + s \approx 1$. This can be justified by the fact, that s is usually lower than 10^{-2} during cloud formation. The condensation rate is determined by the condensational growth of the aerosol particles. Because the growth of particles before their activation is small in comparison to their subsequent growth, only the particles with $s_{\text{crit}} \leq s$ given by Eq. 2.38 are considered in the calculation of the condensational growth rate. Defining m_c as the mass concentration of all activated droplets

$$m_c = \frac{\pi}{6} \rho_w \int_0^s D^3 n_N^*(s')\, ds' \qquad [2.42]$$

and calculating the time derivative results in a formulation of the condensational growth rate

$$\frac{dm_c}{dt} = \frac{\pi}{2} \rho_w \int_0^s D^2 \frac{dD}{dt} n_N^*(s')\, ds'. \qquad [2.43]$$

Substituting Eq. 2.43 in Eq. 2.39 the maximum supersaturation $s_{\max}$ that occurs during the formation of a cloud can be determined by solving

$$\alpha w - \gamma \frac{\pi}{2} \frac{\rho_w}{\rho_a} \int_0^{s_{\max}} D^2 \frac{dD}{dt} n_N^*(s')\, ds' = 0. \qquad [2.44]$$

for $s_{\max}$.

To determine the number of activated aerosol particles during cloud formation, one has to solve the equation system given by Eq. 2.38 and Eq. 2.44. Because a direct analytical solution is not possible, further assumptions have to be made or a numerical solution has to be performed.

2.2.5. Solution of the Supersaturation Balance Equation

Following Twomey (1959), we assume that beyond the point of activation s_{eq} decreases rapidly to zero. Hence, the growth rate of the activated solution droplet (Eq. 2.14) can be approximated by

$$\frac{dD}{dt} = \frac{\Lambda}{D} s \qquad [2.45]$$

and is not influenced by curvature or solute effects anymore. We can integrate equation 2.45 from time τ, when s equals s_{crit}, to the time $t_{\max}$, when $s_{\max}$ is reached, and get the droplet diameter at $t_{\max}$:

$$D^2 = D^2(\tau) + 2\int_{\tau}^{t_{\max}} \Lambda s\, dt. \qquad [2.46]$$

Substituting equations 2.46 and 2.45 into equation 2.44, we obtain:

$$\begin{aligned} \frac{2\alpha w \rho_a}{\pi\gamma\rho_w} - \Lambda s_{\max} \int_0^{s_{\max}} \left(D^2(\tau) + 2\Lambda \int_{\tau}^{t_{\max}} s dt\right)^{1/2} n_N^*(s')\, ds' &= 0 \\ \frac{2\alpha w \rho_a}{\pi\gamma\rho_w} - \Lambda s_{\max} I(0, s_{\max}) &= 0 \end{aligned} \qquad [2.47]$$

To determine the maximum supersaturation we have to calculate the condensation integral $I(0, s_{\max})$, where the parameters in the parentheses indicate the limits of integration:

$$I(0, s_{\max}) = \int_0^{s_{\max}} \left(D^2(\tau) + 2\Lambda \int_{\tau}^{t_{\max}} s\, dt\right)^{1/2} n_N^*(s')\, ds'. \qquad [2.48]$$

An analytic calculation of $I(0, s_{\max})$ is not possible. For this reason, Twomey (1959) derived two asymptotic limits. In case the droplet experiences significant growth after the activation

$$D^2(\tau) \ll 2\Lambda \int_{\tau}^{t_{\max}} s\, dt, \qquad [2.49]$$

and one can neglect $D^2(\tau)$ in Eq. 2.48. For the supersaturation integral Twomey (1959) suggested a lower bound based on geometrical reasons (Fig. 2.4):

$$\int_{\tau}^{t_{\max}} s\, dt \approx \frac{1}{2\alpha w} \left(s_{\max}^2 - s(\tau)^2\right). \qquad [2.50]$$

Applying Eq. 2.49 and substituting Eq. 2.50 in Eq. 2.48, we get the condensation integral for droplets that experience significant growth after their activation:

$$I_1(0, s_{\max}) = \int_0^{s_{\max}} \left(\frac{\Lambda}{\alpha w}\right)^{1/2} \left(s_{\max}^2 - s(\tau)^2\right)^{1/2} n_N^*(s)\, ds. \qquad [2.51]$$

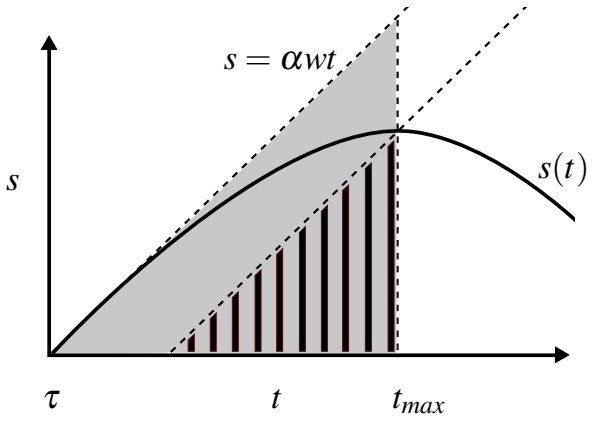

Fig. 2.4.: Evolution of supersaturation (solid line) with time applying the assumptions of Twomey (1959). The area below $s(t)$ given by the integral $\int_{\tau}^{t_{\max}} s\,dt$ is approximated by the the striped area ($\int_{\tau}^{t_{\max}} s\,dt \approx \frac{1}{2\alpha w}\left(s_{\max}^2 - s(\tau)^2\right)$; lower bound for the supersaturation integral) or the grey area (upper bound for the supersaturation integral).

For droplets that do not experience significant growth after the activation, we get

$$D^2(\tau) \gg 2\Lambda \int_{\tau}^{t_{\max}} s\,dt. \qquad [2.52]$$

Assuming that the droplet is in equilibrium with the parcel supersaturation until activation, we can substitute $D(\tau)$ at the time of activation with the diameter D_{crit} given by Eq. 2.35:

$$D(\tau) = D_{\text{crit}} = \frac{2A}{3s_{\text{crit}}}. \qquad [2.53]$$

Applying Eq. 2.52 and substituting Eq. 2.53 in Eq. 2.48, we obtain the condensation integral for the case that the droplets experience no significant growth after their activation:

$$I_2(0, s_{\max}) = \int_0^{s_{\max}} \frac{2A}{3s} n_N^*(s)\,ds. \qquad [2.54]$$

Following Twomey (1959), we derived a lower (Eq. 2.51) and upper (Eq. 2.54) bound for the condensation integral, which can be used in Eq. 2.47 to estimate the upper and lower bound of $s_{\max}$.

Twomey (1959) performed the integration of Eq. 2.51 with a supersaturation distribution of $n_N^*(s_{\text{crit}}) = abs_{\text{crit}}^{a-1}$ to predict the upper bound of $s_{\max}$ and consequently the upper bound for $\text{CCN}(s_{\max}) = bs_{\max}^a$, where b and a are constants depending on the assumed aerosol population (e.g. $b = 125$ and $a = 1/3$ for a so-called maritime aerosol population

and $b = 2000$ and $a = 2/5$ for a so-called continental aerosol population). This form of $\mathrm{CCN}(s_{\max})$ was widely used in numerical atmospheric models that lack the explicit simulation of aerosol particles. For studies with detailed information of the properties of the aerosol population more sophisticated parameterizations have to be used. To determine the supersaturation with respect to ice s_i and the maximum supersaturation with respect to ice $s_{i,\max}$ in an ascending air parcel with nucleating ice crystals (e.g. during the formation of cirrus clouds) Eq. 2.39 to Eq. 2.44 can be formulated with respect to ice. One should note that the assumption $S_i = 1 + s_i \approx 1$, which was made in the derivation of Eq. 2.39 for water saturation, is not valid since s_i can reach values in the order of 0.5 in the atmosphere and therefore Eq. 2.39 becomes more complex if formulated with respect to ice.

2.3. Nucleation of Ice Crystals

Ice crystals can nucleate in the atmosphere in different ways, depending on temperature, saturation with respect to ice, and available aerosol particles. As shown in Table 2.1 the direct nucleation of ice crystals from the gas phase is negligible in the atmosphere. Therefore, the formation of ice crystals requires the freezing of water droplets or solid particles on which ice crystals can nucleate. Freezing of water drops without the presence of solid aerosol particles is refereed to as homogeneous freezing and does not occur at temperatures above -33° C in the atmosphere (Fletcher et al., 1962). If solid particles are present, ice crystals can form at higher temperatures, which is referred to as heterogeneous freezing. At temperatures lower than ≈ -20° C ice crystal are found to nucleate on the surface of insoluble aerosol particles. This process is referred to as deposition freezing. If the air is saturated with respect to water ice crystals can be formed with the help of insoluble particles at temperatures up to ≈ -10° C. Ice crystals can form simultaneously with the condensation of water on a solid particle (Condensation freezing), or in the liquid phase that already surrounds a solid particle (Immersion freezing) or by collision of a supercooled drop with a solid particle (contact freezing). Figure 2.5 shows a sketch of the different freezing mechanisms.

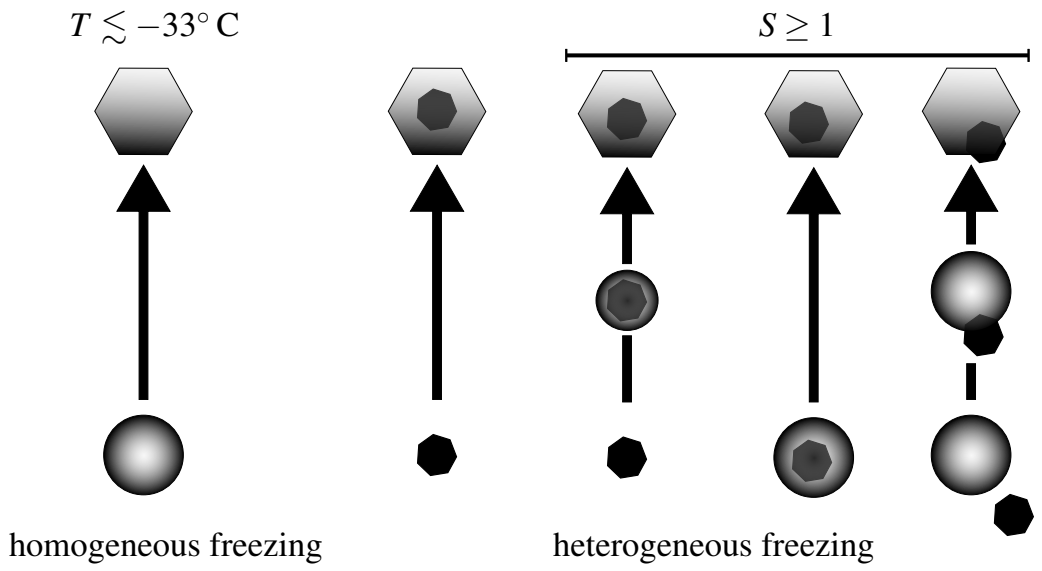

Fig. 2.5.: Freezing mechanisms in the atmosphere.

Homogeneous Freezing

The homogeneous freezing of a water droplet can be described by the classical nucleation theory (Sect. 2.1.2). The nucleation rate is then given by

$$J_{i,hom} = \beta_{i/w} Z_{i/w} \pi D_d^{*2} N_{i/w}^e, \qquad [2.55]$$

where $\beta_{i/w}$ is the collision rate of water molecules with an ice cluster and $N_{i/w}^e$ the distribution of critical ice clusters in the water. The nucleation of an ice crystal inside a water droplet is accompanied with a reorientation of the water molecules, breaking the water-water bounds and formation of water-ice bounds. Hence, an additional energy barrier, which can be expressed by the Gibbs-free energy $\Delta G^{\ddagger}$ has to be passed to form a new ice phase in equilibrium with the surrounding water. In this case the collision rate of water molecules with the ice clusters is given by (Dufour and Defay, 1963)

$$\beta_{i/w} = \dot{N}^{\ddagger} \frac{kT}{h} \exp\left(-\frac{\Delta G^{\ddagger}}{kT}\right), \qquad [2.56]$$

where $\dot{N}^{\ddagger}$ is the number of water molecules in contact with unit area of the ice surface and h is the Planck's constant.Using this definition in the equation for the nucleation rate (Eq. 2.55) we get

$$J_{i,hom} = Z \pi D^{*2} \frac{\dot{N} \dot{N}^{\ddagger} kT}{h} \exp\left(-\frac{\Delta G^{\ddagger} + \Delta G_{i/w}^{*}}{kT}\right), \qquad [2.57]$$

where $\Delta G^*_{i/w}$ is defined accordingly to Eq. 2.10 with respect to ice and water instead of water and water vapor. We see that for the initiation of homogeneous freezing of the droplet two energy barriers (ΔG^* and $\Delta G^{\ddagger}$) have to be passed. For temperatures above -33° C the nucleation rate of freezing droplets is negligible. For lower temperatures $J_{i,hom}$ increases rapidly and ice germs can nucleate in the liquid, initiating the homogeneous freezing of the droplet.

Given a population of droplets, the decrease in number concentration N due to freezing of droplets is given by

$$\frac{dN}{dt} = -N\frac{\pi}{6}D^3 J_{i,hom}, \qquad [2.58]$$

where we assumed that the droplets freeze by one nucleation event per drop. After integration from N_0 at $t = 0$ to N_1 at t we get

$$N_1 = N_0 e^{-\frac{\pi}{6}D^3 J_{i,hom} t} \qquad [2.59]$$

The number concentration of frozen droplets N_i^* after time t is then

$$N_i^*(t) = N_0 - N_1 = N_0\left(1 - e^{-\frac{\pi}{6}D^3 J_{i,hom} t}\right). \qquad [2.60]$$

Thus, the number of frozen droplets increases with time, which is due to the stochastic nature of freezing.

Heterogeneous Freezing

Ice crystals are found to nucleate in the atmosphere at temperatures up to -5° C when solid aerosol particles are present. In case a solid particle is immersed in a water droplet the energy needed for ice germ formation $\Delta G^*_{i/w,het}$ is decreased on the particle surface in comparison to $\Delta G^*_{i/w}$ of homogeneous freezing. This reduction can be describe by (Fletcher et al., 1962)

$$\Delta G^*_{i/w,het} = \Delta G^*_{i/w} f_i \qquad [2.61]$$

where f_i is a geometric factor depending on the contact angle between the cap of the ice molecules and the particle surface, the critical cluster size (Eq. 2.8), and on the particle size. For a particle with a perfect ice nucleating ability $f_i = 0$, which means their is no energy barrier at all. If the particle does not interact with the nucleating droplet $f_i = 1$, which equals the energy barrier for homogeneous freezing. The nucleation rate of ice

crystals $J_{i,het,imm}$ per unit area of the immersed solid particle in the droplet can be derived analogous to Eq. 2.57.

$$J_{i,het,imm} = Z_{i/w}\pi D^{*2}\frac{\dot{N}_s\dot{N}^{\ddagger}kT}{h}\exp\left(-\frac{\Delta G^{\ddagger}+\Delta G^{*}_{i/w}}{kT}\right), \qquad [2.62]$$

where $\dot{N}_s$ is the number of water molecules in contact with unit area of the solid aerosol particle.

In case solid aerosol particles are not immersed, ice crystals can directly nucleate on the surface of the particle. In this case the energy needed for ice germ formation can be derived by

$$\Delta G^{*}_{w/v,het} = \Delta G^{*}_{w/v} f_w, \qquad [2.63]$$

where $\Delta G^{*}_{w/v}$ is given by Eq. 2.10. The nucleation rate of $J_{i,het,dep}$ per unit surface and unit time can then be calculated analogous to Eq. 2.55

$$J_{i,het,dep} = \beta_{w/v}Z_{w/v}\pi D^{*2}\dot{N}_s\exp\left(-\frac{\Delta G^{*}_{w/v,het}}{kT}\right), \qquad [2.64]$$

where in this case $\dot{N}_s$ is the number of adsorbed water molecules per unit area of the particle surface, which can be calculated assuming a steady state of adsorption and desorption fluxes (Pruppacher and Klett, 1997, p. 299f). The nucleation rate decreases rapidly for particles with a radius less than 0.1 μm (Fletcher et al., 1962).

The number of nucleated ice crystals for a population of solid aerosol particles with diameter D_p can be calculated analogous to the approach for homogeneous freezing by assuming that the heterogeneous freezing is a stochastic process

$$N^{*}_{i}(t) = N_{d,0}\left(1-e^{-\pi D_p^2 J_{i,het}t}\right), \qquad [2.65]$$

where D_p is the diameter of the insoluble aerosol particle. Note that $N^{*}_{i}(t)$ scales with the surface area of the solid aerosol particles and that $N^{*}_{i}(t)$ depends on time. In contrast to this so-called "stochastic hypothesis" (Fletcher et al., 1962) one can formulate the number of nucleated ice crystals by the so-called "singular hypothesis" (Levine, 1950), where N^{*}_{i} is independent of t and a function of the properties of the solid particles and temperature only, or by theories combining both approaches (Niedermeier et al., 2011). In laboratory studies one finds that ice nucleation is very localized and that it proceeds at

distinct sites on the particles that are capable of adsorbing water molecules. By introducing the density of active sites per particle surface area, this can be accounted for in Eq. 2.65. The active nucleation sites are not equally distributed among the particles. This causes additional difficulties in the theoretical description of the heterogeneous freezing processes.

The presented classical theory can be used to describe qualitatively the basic physical processes governing the heterogeneous nucleation of ice in the atmosphere. Numerous efforts have been made to improve the quantitative accuracy of the theory, nonetheless most atmospheric applications use empirical functions to describe the heterogeneous freezing of droplets. The formulation of $N_i^*(s_i, T)$ as a function of the aerosol properties based on field measurements or nucleation theory is a challenging task of current research (e.g. Meyers et al., 1992; Phillips et al., 2008; Hoose et al., 2010b)

We can define some basic requirements for an aerosol particle to be an efficient IN. At first, aerosol particles must provide a solid surface. Hence a particle serving as an IN has to be highly water-insoluble. Larger particles are more efficient IN than smaller particles, because $J_{i,het}$ scales with the surface area and larger particles have a higher probability of having an active nucleation site. Additionally f_i and f_w are functions of the particle diameter. Observations suggest that efficient IN have sizes larger than approximately 0.1 μm (Pruppacher and Klett, 1997, p. 327). The particle must be able to efficiently adsorb water molecules on its surface. Therefore the chemical composition of the particle is important. Last but not least, the crystallographic lattice of the particle has to fit to the ice lattice, to avoid strains in the ice germ, which would increase the bulk free energy of the ice germ and reduce the IN ability of the particle.

The most important IN in the atmosphere, which fulfill these requirements, are mineral dust particle (Hoffer, 1961), soot particles (DeMott, 1990), and biological particles (Möhler et al., 2007).

2.4. Aerosol Impact on Cloud Properties

In Section 2.2 and 2.3 we saw that the initial number concentration of clouds droplets and ice crystals is determined by the activation of aerosol particles and the homogeneous and heterogeneous freezing involving aerosol particles. Because of that, the optical

properties of clouds and the efficiency of the microphysical processes in clouds depend on the aerosol population present during the cloud formation.

2.4.1. Impact on Microphysical Processes

The formation of rain in ice free-clouds cannot be explained by the diffusional growth (Eq. 2.15) of cloud droplets ($D_c \approx 5\,\mu$m) to the size of rain drops ($D_r \approx 1\,mm$), because it would need several hours with a sufficient high supersaturation to reach sizes of more than $50\,\mu$m but rain drops are found in cumulus clouds already about 15 min after a cloud forms. Hence, the growth of cloud droplets to the size of rain drops is dominated by another processes, namely the collision and coalescence of the droplets.

The increase in mass of a single cloud drop $\acute{m}_c$ with diameter D_c, falling through a population of smaller drops with diameter D_c' and mass $\acute{m}_c'$, can be calculated by the volume the drop is falling through times the number concentration of smaller drops N_c'

$$\frac{d\acute{m}_c}{dt} = \frac{1}{4}\pi(D_c + D_c')^2(|w^{sed} - w^{sed\prime}|)\acute{m}_c' N_c' = K_c(D_c, D_c')\acute{m}_c' N_c', \qquad [2.66]$$

where w^{sed} and $w^{sed\prime}$ are the fall velocities of the drops and $K_c(D_c, D_c')$ is the collection kernel. Small drops will follow the flow field around the larger drop. Therefore, the collection cross section will decrease. Consequently, the growth of the larger drop by collision will be less effective. This effect is considered by the definition of a collection efficiency

$$E(D_c, D_c') = \frac{\Omega_c^2}{(D_c + D_c')^2}, \qquad [2.67]$$

where Ω_c is the diameter of the collision cross section formed by the grazing tracks of the drops. In Figure 2.6 values of $E(D_c, D_c')$ are shown for different drop diameters. The collection efficiency decreases significantly with the droplet diameters. The collection kernel of two drops falling with different fall velocities is then

$$K(D_c, D_c') = \frac{1}{4}\pi(D_c + D_c')^2 E(D_c, D_c')|w^{sed} - w^{sed'}|, \qquad [2.68]$$

Smaller cloud droplets will grow slower in comparison to larger particles and for droplets smaller than $10\,\mu$m the collision efficiency is negligible. Therefore aerosol particles can strongly modify the growth of cloud droplets to rain drops. An decrease in D_c, as a consequence of a high number of activated aerosol particles, will decrease the efficiency of the growth of cloud droplets to precipitating rain drops and can suppress the rain

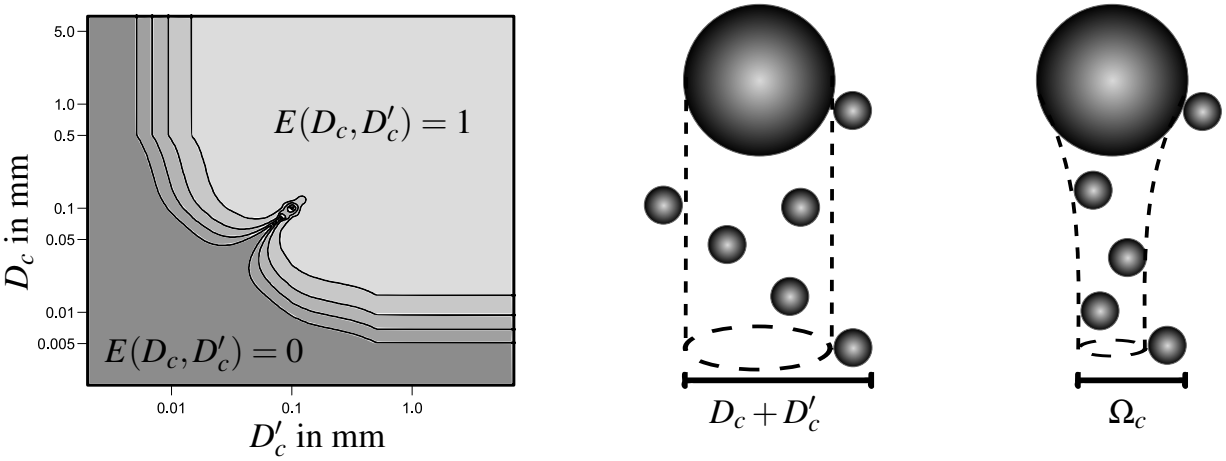

Fig. 2.6.: Collection efficiency calculated from a solution of the Navier-Stokes equation after Pinsky et al. (2001) (left) and sketch of geometric (middle) and hydrodynamic collision cross section (right)

formation if D_c of the cloud droplets does not exceed $10\,\mu$m. One should note, that in order to grow by collision, the droplets have to coalesce, which was not taken into account so far.

Although Eq. 2.66 describes the growth of a cloud droplet by coagulation, the growth of a droplet distribution is more complicated. Some droplets will by chance experience a greater than average frequency of collection events and therefore grow faster in comparison to other drops of the same size. This probabilistic aspect of the collection growth of droplets is accounted for in the quasi stochastic collection equation for a droplet number mass distribution $n_{N,c}(\acute{m}_c)$ (Pruppacher and Klett, 1997, p. 622ff)

$$\begin{aligned}\frac{\partial n_{N,c}(\acute{m}_c)}{\partial t} = \; & \tfrac{1}{2}\int_0^{\acute{m}_c} n_{N,c}(\acute{m}_c - \acute{m}_c')\, n_{N,c}(\acute{m}_c')\, K(\acute{m}_c - \acute{m}_c', \acute{m}_c')\, d\acute{m}_c' \\ & - n_{N,c}(\acute{m}_c) \int_0^{\infty} n_{N,c}(\acute{m}_c')\, K(\acute{m}_c, \acute{m}_c')\, d\acute{m}_c'.\end{aligned} \qquad [2.69]$$

Note that K_c is given as a function of $\acute{m}_c$ rather than D_c. The first term on the r.h.s of Eq. 2.69 increases the number concentration of drops with mass $\acute{m}_c$ by the collision of smaller droplets, whereas the second term decreases the number concentration of drops with mass $\acute{m}_c$ by their collision with other droplets. In this context, K_c can be interpreted as the probability that a droplet with mass $\acute{m}_c$ collects a droplet with mass $\acute{m}_c'$ per unit time.

The quasi stochastic collection equation can be used to describe the growth and formation of different hydrometeors by collision if appropriate formulations for K_c are used (e.g. Beheng, 1982).

2.4.2. Impact on Cloud Optical Properties

Apart from microphysical processes, the optical properties of clouds are modified by aerosol particles. In this section the simple case of sunlight crossing a single cloud layer is discussed to highlight the physical principles of the interaction of aerosol particles with the optical properties of a cloud (e.g. Petty, 2004, p. 189ff). Following Beer's law, the transmittance of a cloud layer is given by

$$t_c = e^{-\tau_c/\mu}, \qquad [2.70]$$

where τ_c is the optical depth of the cloud and μ is the cosine of the solar zenith angle. The optical depth is defined as

$$\tau_c = \int_{z_{cb}}^{z_{ct}} \beta_{e,c}(z)\, dz, \qquad [2.71]$$

where $\beta_{e,c}$ is the extinction coefficient, z is the vertical coordinate in m, z_{cb} the height of the cloud base, and z_{ct} the height of the cloud top. The extinction coefficient of a monodisperse cloud can be calculated by

$$\beta_{e,c} = N_c Q_e \pi r^2 = k_e m_c = k_e N_c \frac{4}{3} \pi r_c^3 \rho_w, \qquad [2.72]$$

where Q_e is the ratio of extinction cross section and geometrical cross section know as the extinction efficiency, N_c the number concentration of cloud droplets, m_c is the mass concentration of cloud water, r_c the radius of the cloud droplets, and k_e the mass specific extinction coefficient given as

$$k_e = \frac{\beta_{e,c}}{m_c} = \frac{3 Q_e}{4 \rho_w r_c}. \qquad [2.73]$$

Substituting Eq. 2.73 and Eq. 2.72 in Eq. 2.71 and using that $Q_e = 2$ in good approximation for cloud droplets and visible light one gets

$$\tau_c = \frac{3}{2 \rho_w r_c} LWP, \qquad [2.74]$$

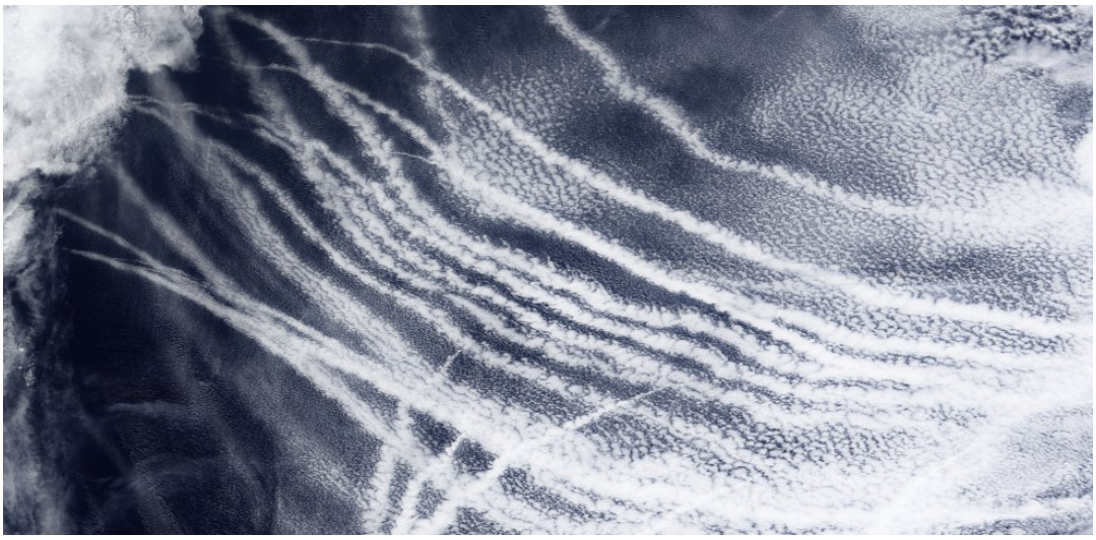

Fig. 2.7.: Satellite image by MODIS showing an increased optical thickness of clouds along shipping routes on March 4, 2009 over the northeast Pacific Ocean. NASA images by Robert Simmon and Jesse Allen, based on an image by Jeff Schmaltz, MODIS Rapid Response Team.

where $LWP = \int_{z_{cb}}^{z_{ct}} m_c \, dz$ is the liquid water path of the cloud layer in g m^{-2}. We see that $\tau \propto 1/r_c$ and $\tau \propto LWP$. We can substitute r_c in Eq. 2.74 and get

$$\tau_c \approx \left(\frac{9 LWP^2 \pi (z_{ct} - z_{cb})}{2\rho_w^2} N_c \right)^{1/3}. \qquad [2.75]$$

For a cloud with a fixed cloud depth and a fixed LWP, τ_c is proportional to $N_c^{1/3}$. Since N_c is determined by the number concentration of activated aerosol particles, τ_c depends on the aerosol particles that are present during cloud formation.

The impact of aerosol on the optical properties of clouds can be seen best during the formation of so-called ship tracks, where stripes of optical thick clouds are found in vicinity of traveling ships in an environment of stratified optical thin clouds (Fig. 2.7)

In reality, the distribution of cloud droplets is not monodisperse but consists of droplets of different sizes. Therefore we need to find a formulation of τ_c as a function of the properties of the cloud droplet size distribution. We can calculate $\beta_{e,c}$ and m_c of the cloud layer by an integration over the cloud droplet size distribution $n_{N,c}$ (Petty, 2004)

$$\beta_{e,c} = \int_0^\infty n_{N,c}(r_c) Q_e \pi r_c^2 \, dr_c \qquad [2.76]$$

and

$$m_c = \int_0^\infty n_{N,c}(r_c) \rho_w \frac{4\pi}{3} r_c^3 \, dr_c. \qquad [2.77]$$

Consequently, we can calculate the optical thickness of a polydisperse cloud layer by

$$\tau_c = \frac{\beta_{e,c}}{m_c} LWP = \frac{\int_0^\infty n_{N,c}(r_c) Q_e \pi r_c^2 \, dr_c}{\int_0^\infty n_{N,c}(r_c) \rho_w \frac{4\pi}{3} r_c^3 \, dr_c} LWP \approx \frac{3}{2\rho_w} \frac{LWP}{r_{c,\text{eff}}}, \qquad [2.78]$$

where we made use of $Q_e \approx 2$ and introduced the effective radius $r_{c,\text{eff}}$ of the cloud droplet distribution

$$r_{c,\text{eff}} = \frac{\int_0^\infty n_{N,c}(r_c) r_c^3 \, dr_c}{\int_0^\infty n_{N,c}(r_c) r_c^2 \, dr_c} = \frac{M_3^c}{M_2^c}, \qquad [2.79]$$

where M_2^c and M_3^c are the second and third moment of $n_{N,c}(r_c)$.

For the numeric simulation of radiation transfer in the atmosphere $\beta_{e,c}$ is used usually. Rearranging Eq. 2.78 we get an expression for the extinction of solar radiation of a single cloud layer

$$\beta_{e,c} \approx \frac{3 m_c}{2\rho_w r_{c,\text{eff}}}. \qquad [2.80]$$

Radiation transfer in the atmosphere is not a one dimensional problem. Especially in overcast situation most of the solar radiation is scattered multiple times before it reaches the surface. To account for these affects additional information about the scattering angles and the contribution of absorption to the extinction has to be known. In three dimensional atmospheric numerical model frameworks direct solar radiation and diffusive scattered radiation is distinguished. To simplify the problem of three dimensional scattering, a two-stream approximation is usually used for the diffusive part of the atmospheric radiation. Thereby, the upwelling and downwelling part of the diffusive radiation in an atmospheric column are assumed to be isotropic in each hemisphere. The radiation transfer in an atmospheric column can then be treated as a one dimensional problem and can be described by the extinction coefficient, the single scattering albedo, which is defined as the scattering fraction of the extinction coefficient, and the asymmetry parameter, which can be interpreted as the average of the cosine of the scattering angle for a high number of scattering events (Petty, 2004). All parameters are a function of wavelength and in case of clouds, they depend on the size distribution of hydrometeors in the cloud.

2.5. Feedback Processes between Aerosol, Clouds, and the State of the Atmosphere

In the previous sections the theoretical concepts of nucleation and growth of aerosol droplets to the size of cloud droplets and rain drops were discussed. Although the physics governing the individual processes are well known, the interaction of aerosol and clouds is poorly understood, because of the complex coupling of the individual processes and the variety of atmospheric conditions. As a result, the potential impact on the hydrological cycle and the radiation budget of the atmosphere is still not quantified.

It is evident, that changes in the atmospheric aerosol load have an immediate impact on the formation of cloud droplets and ice crystals in the atmosphere (Sect. 2.2 – 2.3); but the magnitude of this impact on cloud droplet number, for example for a change in number concentration of a specific aerosol particle, is still poorly quantified. A main reason is the competition of the individual particles for water vapor during the cloud formation and the resulting feedback on supersaturation. An increase in the number concentration of hygroscopic aerosol particles decreases the maximum supersaturation reached during cloud formation. This can inhibit the activation of smaller aerosol particles and attenuate or inhibit the increase in cloud droplet number. As long as not all particles that are present during cloud formation as well as their physiochemical properties are known, a reliable quantitative assessment of the susceptibility of cloud droplet number to aerosol changes is impossible.

Additionally to the aerosol properties, the atmospheric conditions have to be known. Especially updrafts and the accompanying adiabatic cooling (Eq. 2.39) are the main source of supersaturation in the atmosphere and therefore crucial for the aerosol activation. The susceptibility of cloud droplet number to changes in the aerosol is very variable, depending on the number of aerosol particles and the updraft velocity. Reutter et al. (2009) distinguished three different regimes of the susceptibility of N_c to varying aerosol number concentrations, based on simulations with a parcel model. In the first regime, the fraction of activated particles is high and N_c is limited by the available particle number and practically independent of the updraft velocity. In the second regime, N_c is dominated by the updraft velocity, since the fraction of activated particles and the supersaturation are low ($s < 0.2\%$). In the third intermediate regime, N_c is sensitive to both, aerosol and updraft velocity. In reality, the susceptibility of N_c on the aerosol is

even more complex, because beside the aerosol number also the shape of CCN(s) can vary significantly (Bangert, 2008).

During the formation of ice clouds similar feedbacks involving the ice supersaturation can be identified, especially if homogeneous freezing and heterogeneous freezing occur together. An increase in efficient atmospheric IN and therefore a more efficient heterogeneous freezing at lower ice saturations can decrease the peak ice supersaturation and weaken or completely inhibit the homogeneous freezing of droplets, which strongly depends on ice supersaturation. Because the number concentration of homogeneously frozen ice crystals typically exceeds the number of heterogeneously frozen crystals by one order of magnitude the ice crystal number concentration is expected to decrease with increasing IN at temperatures below the homogeneous freezing threshold (DeMott et al., 1997).

In summary, the response of cloud droplet and ice crystals number concentration to changes in the number concentration and properties of the aerosol particles is non-linear and, as a result, can be contradictory to the expected common result ”more aerosol causes more cloud droplets/ ice crystals“.

Aerosol induced changes of cloud droplet and ice crystal number concentration have an impact on the optical properties of the cloud as well as on the efficiency of microphysical processes, such as the rain formation by collisional growth of drops and crystals (Sect. 2.4). The net impact of these processes on the radiation budget and on the hydrological cycle is still poorly understood (IPCC, 2007). Reasons are the various feedback processes involving atmospheric stability, cloud dynamics, and the water budget. They strongly depend on atmospheric conditions and cloud type and therefore are hard to generalize. For this reason, estimates of the net impact of aerosol-cloud interactions on the radiation budget and the hydrological cycle are restricted to specific atmospheric conditions and cloud types. In the following the basic concepts of different possible scenarios are discussed.

In case of an ice-free shallow stratocumulus layer an increase in aerosol number concentration, and consequently in the cloud droplet number concentration, decreases the average cloud droplet size, assuming that the cloud water amount is not affected. As discussed in Sect. 2.4 this will increase the solar optical thickness of the cloud. As a consequence, less solar radiation reaches the surface, which results in lower surface temperatures and more solar radiation is scattered back into space. This net increase in

the planetary albedo is referred to as the Twomey effect (Twomey, 1974) or first indirect aerosol effect (Lohmann and Feichter, 2005). Additionally, the onset of precipitation is delayed or even suppressed (Sect. 2.4). As a result, the cloud water amount is maintained for a longer time and thus the lifetime of the cloud is increased potentially. Hence, less solar radiation reaches the surface and the planetary albedo is increased, which is referred to as the Albrecht effect (Albrecht, 1989) or second indirect aerosol effect.

Modifications of the atmospheric radiation budget always result in a modification of atmospheric stability. When less radiation reaches the surface, as a consequence of the discussed aerosol-cloud interactions, the resulting lower surface temperature causes a more stable lower troposphere. As a result, the subsequent formation of clouds can be affected, which in turn modifies the radiation budget and precipitation formation. As a consequence, the net impact of aerosol changes on clouds, precipitation and the radiation budget depends on the susceptibility of the cloud development on modifications of the atmospheric conditions. Beside the modification of the radiation budget, also aerosol induced changes in cloud entrainment and droplet evaporation, due to changes in precipitation, cloud water amount and droplet size, can modify the atmospheric lapse rate (Wood, 2007; Small et al., 2009; Koren and Feingold, 2011) and therefore the further development and formation of clouds. Additionally, aerosol particles modify the radiation budget by scattering and adsorption, which is referred to as the direct aerosol effect. The accompanying impact on atmospheric stability and cloud development as well as the potential evaporation of cloud droplets due to the temperature increase caused by absorbing aerosol particles are referred to as semi-direct aerosol effect (Koch and Del Genio, 2010).

In short, even in case of ice free clouds numerous feedback mechanisms exist, which make the quantification of the net impact of aerosol changes on clouds, precipitation and radiation difficult.

For mixed phase clouds the number of feedback processes increases, and as a consequence the response of the cloud system to aerosol changes is more complex. The most challenging and most discussed problem is the impact of aerosol changes on precipitation (Khain, 2009; Stevens and Feingold, 2009; Small et al., 2009; Levin and Cotton, 2009; Rosenfeld et al., 2008). Depending on the cloud type the influence of aerosol changes on cloud microphysics can affect precipitation amounts very differently.

As discussed, an increase in aerosol concentration can decrease the cloud droplet size. Hence, the formation of precipitation by drop collision is less effective and more cloud droplets reach the freezing level. Finally, the additional release of latent heat accompanying their freezing, can strengthen the updrafts inside the cloud. The increase in cloud ice and the more intense cloud dynamics can facilitate an effective production of precipitation. As a result, an increase in aerosol concentration can result in an increase rather than an decrease in precipitation (e.g. Seifert and Beheng, 2006a; Khain, 2009). On the other hand, if no IN are present, the cloud droplets can reach the homogeneous freezing level in deep convective clouds and freeze to small crystals that are unable to produce precipitation efficiently (Rosenfeld et al., 2008). Thus, the development of mixed phase clouds is susceptible to the IN number concentration and depends on the height of the homogeneous and heterogeneous freezing level. An increase in efficient IN can cause an effective glaciation of the mixed phase clouds and potentially increase precipitation. On the contrary, a further increase in IN will result in smaller ice crystals that fall more slowly and consequently the formation of precipitation is less effective (Lebo and Seinfeld, 2011). Furthermore, the impact of changes in CCN and IN concentration on the development of mixed phase clouds depends on the development stage of the clouds (van den Heever et al., 2006).

The development of clouds, modified by changes in the aerosol population, can not be investigated independent of their surroundings. The development of convective clouds systems strongly depends on the formation of precipitation and the accompanying production of pools of cold air (Houze, 2004). Aerosol induced changes in precipitation of a cloud can potentially trigger or inhibit the formation and development of clouds and precipitation in the surroundings. Koren and Feingold (2011) used a simple mathematical model to point out that for shallow boundary layer cloud systems the coupling of clouds, precipitation and dynamics results in oscillating cycles, which are mediated by the aerosol concentration.

Finally, the atmospheric water budget must be fulfilled. Strongly enhanced precipitation will limit the water vapor available for subsequent cloud and rain formation, whereas a suppression of precipitation can potentially enhance the precipitation formation in the later cloud development. On the global scale, the amount of precipitation must balance the amount of evaporation. A potential reduction in precipitation from shallow

clouds caused by an increase in the aerosol concentration has to be compensated, for example by an increase in precipitation from convective clouds (Rosenfeld et al., 2008).

In summary, various feedback mechanisms between aerosol, clouds, radiation, precipitation, and atmospheric conditions exist, which inhibit a simple classification and general quantification of the aerosol-cloud interactions.

3. Numerical Model Framework

Investigating the interaction of aerosol particles and the atmosphere with a numerical model at a specific scale requires the treatment of the relevant physical, chemical, and aerosol dynamical processes at a comparable level of complexity. To fulfill these requirements the model system COSMO-ART (Vogel et al., 2009) was developed for the regional to continental scale.

3.1. COSMO-ART

COSMO-ART is based on the non-hydrostatic weather forecast model COSMO (*C*onsortium for *S*mall-scale *MO*delling, Baldauf et al., 2011) of the Deutscher Wetterdienst (DWD), which was coupled with comprehensive modules for gas phase chemistry and aerosol dynamics. ART stands for *A*erosols and *R*eactive *T*race gases. The coupling of gas phase and aerosol processes with the state of the atmosphere is realized in a consistent way using the same grid for all scalars, e.g. temperature, humidity, aerosol and gas phase concentrations. For processes affecting all scalars, as for example advection, the same numerical schemes and integration time steps are applied. As a result, COSMO-ART enables the simulation of feedback processes between gas phase and aerosol processes, and the state of the atmosphere.

The chemical reactions of gas phase species are accounted for by the RADMKA mechanism (*R*egional *A*cid *D*eposition *M*odel Version *KA*rlsruhe, Vogel et al., 2009). RADMKA is based on an extended version of the gas phase mechanism RADM2 (*R*egional *A*cid *D*eposition *M*odel, Stockwell et al., 1990) for inorganic species and the SORGAM mechanism (*S*econdary *ORG*anic *A*erosol *M*odel, Schell et al., 2001), which calculate the photochemical formation of gaseous precursors for the secondary formation of aerosol particles. The photolytic dissociation rates are derived with an efficient parameterization (Vogel et al., 2009; Bangert, 2006), which is consistent with the simulated atmospheric radiation fields. Therefore, the impact of clouds on photochemistry

Tab. 3.1.: Overview of the individual aerosol modes, their chemical composition (first block), aerosol dynamical processes (second block), and their initial diameter and standard deviation (third block).

	if	ic	jf	jc	so	sa	sb	sc	da	db	dc
sulfate	•	•	•	•							
nitrate	•	•	•	•							
ammonium	•	•	•	•							
organics	•	•	•	•							
soot		•		•	•						
sodium chloride						•	•	•			
mineral dust									•	•	•
coagulation	•	•	•	•	•						
condensation	•	•	•	•	•						
initial median diameter of the log-normal number size distribution in μm											
	0.01	0.08	0.07	0.08	0.08	0.2	1	12	1.5	6.7	14.2
standard deviation of the log-normal number size distribution											
	1.7	2	1.7	2	1.4	1.9	2	1.7	1.7	1.6	1.5

and consequently on the formation and growth of secondary aerosol particles is represented in the model framework.

The nucleation of secondary aerosol particles is based on the binary homogeneous nucleation of sulfuric acid and water and calculated with the parameterization of Kerminen and Wexler (1994).

The aerosol module $\text{MADE}_{\text{soot}}^{\text{extended}}$ (extended *M*odal *A*erosol *D*ynamics model for *E*urope including *soot*; Vogel et al., 2009) is used to describe the aerosol population by eleven overlapping log-normal size distribution functions, so-called modes, and represent the aerosol dynamic processes like the Brownian coagulation of small particles. Five modes represent sub-micron particles consisting of sulphate, ammonium, nitrate, organic compounds, water, and soot in a range of mixing states and sizes, and are allowed to interact with anthropogenic emissions of particles and gases. These modes enable the explicit simulation of soot aging in the atmosphere (Riemer et al., 2004, 2003). Sea salt and mineral dust particles are represented by three modes for differ-

ent size ranges in each case. An overview of the different modes is given in Table 3.1. The emissions of sea salt and mineral dust particles are calculated online in the model as a function of atmospheric state, e.g. 10 m-windspeed, and friction velocity, and surface properties, such as sea surface temperature, soil type, and soil moisture (Lundgren, 2010; Stanelle et al., 2010).

3.2. Numerical Description of Aerosol Particles

The atmospheric aerosol is a suspension of polydisperse particles with varying chemical composition suspended in the air and can be described by a continuous size distribution as a function of the particle diameter

$$n_N(D_p) = \frac{dN}{dD_p}. \qquad [3.1]$$

To describe chemical and physical processes related with the atmospheric aerosol in numerical model systems efficiently, the size distribution of the aerosol particles is separated in individual overlapping modes, depending on the size and chemical composition of the particles (Whitby and McMurry, 1997). Each mode is approximated by a log-normal size distribution function (Whitby, 1978) with constant chemical composition:

$$n_{N,l}(D_p) = \frac{1}{D_p} \frac{N_l}{\sqrt{2\pi} \ln \sigma_l} \exp\left(-\frac{\ln^2(D_p/\overline{D_{p,l}})}{2\ln^2 \sigma_l} \right). \qquad [3.2]$$

where N_l is the number concentration of particles in mode l, σ_l is the geometrical standard deviation of mode l, and $\overline{D_{p,l}}$ the median diameter of the particles in mode l. The size distribution function and the total number concentration of aerosol particles can be calculated by

$$n_N(D_p) = \sum_l n_{N,l}(D_p), \qquad [3.3]$$

$$N = \sum_l N_l = \sum_l \int_0^\infty n_{N,l}(D_p)\, dD_p. \qquad [3.4]$$

To simulate the temporal evolution of $n_{l,N}(D_p)$ in the atmosphere, one has to simulate the temporal evolution of N_l, σ_l, and $\overline{D_{p,l}}$. For processes like advection and diffusion the differential equations for σ_l and $\overline{D_{p,l}}$ can not be solved directly (Whitby and McMurry,

1997). Therefore, the equations in the model are formulated for integral moments of $n_{l,N}(D_p)$. The k-th moment M_k^x of the size distribution of mode l is defined as

$$M_k^l = \int_0^\infty D^k n_{N,l}(D_p)\, dD_p. \qquad [3.5]$$

The moments are directly related to integral quantities of the aerosol population by

$$N_l = \int_0^\infty n_l(D_p)\, dD_p = M_0^l, \qquad [3.6]$$

$$O_l = \pi \int_0^\infty D_p^2 n_l(D_p)\, dD_p = \pi M_2^l, \qquad [3.7]$$

$$V_l = \frac{\pi}{6} \int_0^\infty D_p^3 n_l(D_p)\, dD_p = \frac{\pi}{6} M_3^l, \qquad [3.8]$$

$$m_l = \frac{\pi}{6} \rho_p \int_0^\infty D_p^3 n_l(D_p)\, dD_p = \frac{\pi}{6} \rho_p M_3^l, \qquad [3.9]$$

where O_l is the surface concentration, V_l the volume concentration, and m_l the mass concentration of mode l. To fully determine $n_{l,N}(D_p)$, three moments of the log-normal size distribution function are needed, because of the three parameters N_l , σ_l, and $\overline{D_{p,l}}$. To derive a numerically feasible solution of the resulting equation system, σ_l is held constant for each mode. Thus, two moments have to be calculated to determine $n_{l,N}(D_p)$. In COSMO-ART balance equations for N_l and m_l are solved, which are proportional to M_0^l and M_3^l (Eq. 3.6 and Eq. 3.9). Given N_l, m_l, and σ_l, we can calculate $\overline{D_{p,l}}$ by

$$\overline{D_{p,l}} = \left(\frac{6 m_l}{\pi \rho_p \exp\left(9/2 \ln^2 \sigma_l\right) N_l} \right)^{\frac{1}{3}}, \qquad [3.10]$$

and finally calculate $n_{l,N}(D_p)$ as given in Eq. 3.2.

The temporal evolution of $n_{l,N}(D_p)$ is calculated by solving the Reynolds-averaged balance equations of N_l and m_l, which are given by (Doms, 2011; Jacobson, 2005)

$$\frac{\partial}{\partial t} y_l = \underbrace{-\nabla \cdot (\mathbf{v} y_l)}_{\substack{\text{advection} \\ \text{(flux form)}}} + \underbrace{\nabla \cdot \mathbf{F}_{y_l}}_{\text{turbulence}} + \underbrace{\frac{\partial}{\partial z}\left(\overline{w_l^{\text{sed}}} y_l\right)}_{\substack{\text{gravitational} \\ \text{sedimentation}}} + \underbrace{S_{y_l}}_{\substack{\text{microphysical} \\ \text{processes}}} \qquad [3.11]$$

for $y = \{N, m\}$, where $\mathbf{F_{y_l}} = -\overline{\mathbf{v}' y_l'}$ is the turbulent flux and $\mathbf{v}'$ and y_l' are the sub-grid-scale components of y_l and $\mathbf{v}$. One should note that Eq. 3.11 is only applicable in case of the conservative flux-form advection scheme of COSMO (Runge-Kutta time integration with a Bott-advection scheme), which is recommended for studies of

aerosol-cloud interaction because of its mass conserving formulation. For the other available advection schemes in COSMO (e.g. a semi-Lagrangian advection scheme and a three timelevel leapfrog time integration scheme with explicit advection) the balance equations have to be formulated in advection form for mass specific quantities ($d\Psi/dt = -\mathbf{v}\cdot\nabla\Psi + 1/\rho[\ldots]$), such as mass mixing ratios. The turbulent fluxes are parameterized according to the cloud hydrometeors in COSMO (Doms et al., 2011). One should note that y_l and $\mathbf{v}$ are mass weighted, time and volume averages for each grid cell and time step. The contribution of molecular diffusion is small and is neglected. $S_{N,l}$ and $S_{m,l}$ describe the contributions of the parameterized processes. For mode if, ic, jf, jc and c coagulation and condensation is considered:

$$\begin{aligned} S_{N_l} &= S^{\text{nuc}}_{N_{(l=if)}} + S^{\text{wash}}_{N_l} + S^{\text{coag}}_{N_l} + S^{\text{coag}^\circ}_{N_l} + S^{\text{conv}}_{N_l}, \\ S_{m_l} &= S^{\text{nuc}}_{m_{(l=if)}} + S^{\text{wash}}_{m_l} + S^{\text{coag}}_{m_l} + S^{\text{cond}}_{m_l} + S^{\text{conv}}_{m_l}, \end{aligned} \qquad \text{for } l = if, ic, jf, jc, c \quad [3.12]$$

The modes sa, sb, sc, da, db and dc do not interact with other modes and the gas phase; therefore we get

$$\begin{aligned} S_{N_l} &= S^{\text{wash}}_{N_l} + S^{\text{conv}}_{N_l}, \\ S_{m_l} &= S^{\text{wash}}_{m_l} + S^{\text{conv}}_{m_l}. \end{aligned} \qquad \text{for } l = sa, sb, sc, da, db, dc \quad [3.13]$$

The individual microphysical processes are:

$S^{\text{nuc}}_{N_l}$ and $S^{\text{nuc}}_{m_l}$	are the source rates due to nucleation from the gas phase,
$S^{\text{wash}}_{N_l}$ and $S^{\text{wash}}_{m_l}$	decribe the scavenging of particles by precipitation,
$S^{\text{coag}}_{N_l}$ and $S^{\text{coag}}_{m_l}$	are the tendencies due to intermodal coagulation,
$S^{\text{coag}^\circ}_{N_l}$	is the tendency due to intramodal coagulation,
$S^{\text{cond}}_{m_l}$	is the condensation rate,
$S^{\text{conv}}_{N_l}$ and $S^{\text{conv}}_{m_l}$	describes the sub-grid-scale convective transport (optional),

The emission of particles and the deposition at the surface are boundary conditions for the solution of Eq. 3.11. A detailed description of the individual processes is given in Vogel et al. (2009) and Riemer et al. (2003).

3.3. Radiation Scheme

The atmospheric radiation fluxes are calculated with the GRAALS (Ritter and Geleyn, 1992) radiation scheme for eight spectral bands. GRAALS is based on the two-stream

Tab. 3.2.: Overview of the spectral bands used in GRAALS.

	wavelength intervals in μm				
solar	1.53–4.64	0.7–1.53	0.25–0.7		
thermal	20.0–104.5	12.5–20.0	8.33–9.01 and 10.31–12.5	9.01–10.31	4.64–8.33

approximation of the radiative transfer equations. GRAALS provides a spatially variable climatology of aerosol optical properties. To consider the impact of the simulated aerosol particles and cloud hydrometeors on the radiation fields in the atmosphere their extinction coefficient, single scattering albedo, and asymmetry factor (Sect. 2.4.2) have to be calculated.

The optical properties of the aerosol particles are parameterized as a function of aerosol size distribution and chemical composition with the use of detailed Mie calculation performed a priori. The optical properties of clouds droplets and ice crystals are parameterized in GRAALS as a function of the corresponding mass concentration, since the standard cloud scheme of COSMO provides no information of hydrometeor number concentration and size. In this study more sophisticated cloud schemes are included in COSMO-ART, which provide information of the size distribution of the cloud hydrometeors. To consider the effect of varying hydrometeor size distributions, new parameterizations of the cloud optical properties were introduced, which is described in Sect. 4.6.

3.4. Cloud Microphysics

In COSMO clouds are represented by a bulk microphysics scheme, which describes different categories of cloud hydrometeors by size distribution functions. The selection of categories follows the traditional grouping (Houze, 1994) by phase, size and terminal fall speed respectively into cloud droplets, rain drops, cloud ice, and snow. Microphysical processes are represented by modifications of the size distributions and transfer of hydrometeors from one category to another. The scheme is designed for operational weather forecast and therefore has to be computationally efficient. Consequently, only one moment of each size distribution function, the mass mixing ratio of the hydrometeors, is simulated. Number concentration and standard deviation of the size distribution

functions are held constant. A detailed description of the conversion processes between the hydrometeor categories and their parameterization in the operational model version of COSMO is given in Doms et al. (2011) and Seifert (2008).

To investigate the impact of aerosol particles on cloud microphysical processes, one has to simulate at least two moments of the size distribution functions of the cloud hydrometeors. In a first step, Bangert (2008) enabled the simulation of the aerosol impact on the ice-free cloud phase extending the operational cloud scheme with a prognostic treatment of the cloud droplet number concentration. The introduced budget equation for the number concentration of cloud droplets (N_c) is:

$$\frac{\partial}{\partial t}N_c = \underbrace{-\nabla\cdot(\mathbf{v}N_c)}_{\substack{\text{advection}\\ \text{(flux form)}}} + \underbrace{\nabla\cdot\mathbf{F}_{N_c}}_{\text{turbulence}} + \underbrace{S^{act}_{N_c}}_{\substack{\text{activation of}\\ \text{aerosol particles}}} + \underbrace{S_{N_c}}_{\substack{\text{microphysical}\\ \text{processes}}}, \qquad [3.14]$$

where the microphysical processes are

$$S_{N_c} = -S^{\text{au}}_{\substack{N_c\\ c\to r}} - S^{\text{sc}}_{\substack{N_c\\ c\to c}} - S^{\text{acc}}_{\substack{N_c\\ r+c\to r}} + S^{\text{melt}}_{\substack{N_c\\ i\to c}} - S^{\text{freez}}_{\substack{N_c\\ c\to i}} - \frac{1}{\overline{m_c}}\left(S^{\text{rim}}_{\substack{m_c\\ s+c\to s}} + S^{shed}_{\substack{m_c\\ s+c\to r}}\right). \qquad [3.15]$$

The individual conversion rates describe:

$S^{\text{au}}_{\substack{m_c\\ c\to r}}$ the formation of rain drops by collision and coalescence

$S^{\text{sc}}_{\substack{N_c\\ c\to c}}$ the self-collection of cloud droplets,

$S^{\text{acc}}_{\substack{m_c\\ r+c\to r}}$ the accretion of cloud droplets by raindrops,

$S^{\text{melt}}_{\substack{N_c\\ i\to c}}$ the melting of ice crystals,

$S^{\text{freez}}_{\substack{N_c\\ c\to i}}$ freezing of cloud droplets,

$S^{\text{rim}}_{\substack{m_c\\ s+c\to s}}$ the collection of cloud water by snow (riming),

$S^{\text{shed}}_{\substack{m_c\\ s+c\to r}}$ the collection of cloud water by wet snow to form rain (shedding).

The autoconversion, accretion, and selfcollection of cloud droplets are calculated with the parameterization of Seifert and Beheng (2001) as a function of the varying cloud droplet size distribution. The autoconversion rate is inversely proportional to the square of the number concentration of cloud droplets (N_c). For the cloud droplets a Gamma size distribution function is assumed. The autoconversion parameterization relies on a solution of the stochastic collection equation (Eq. 2.69) and is well validated against simulations using spectral bin microphysics (Seifert and Beheng, 2006a). Cloud ice crystals

are assumed to melt instantaneously when the ambient temperature rises above 273.15 K and the melting ice crystal number concentration is assumed to be the maximum of either $100\,\mathrm{m}^{-3}$ or $\rho_a x_i / \overline{m}_i^{\max}$, where x_i is the ice mass mixing ratio and $\overline{m}_i^{\max} = 10^{-9}\,\mathrm{kg}$ is the maximum mean ice crystal mass in the model (Doms et al., 2011). The homogeneous freezing of cloud droplets occurs at a temperature of 236.15 K, where all cloud water is assumed to freeze instantaneously. The conversion rates of cloud water due to riming and shedding on snow are calculated with the original one moment bulk approach of COSMO (Doms et al., 2011). The condensation and evaporation of water vapor is calculated with a simple saturation adjustment approach. Each timestep the temperature, water vapor and cloud water is iteratively adjusted to a saturated state, taking the latent heating into account. The resulting decrease or increase in cloud water represents the condensation or evaporation during this time step (Doms et al., 2011). The use of such a simple scheme is justified because S is always close to saturation inside clouds. Furthermore, supersaturated layers, e.g. at the cloud base, can not be resolved by the vertical resolution used in typical applications of the model system ($\Delta z \approx 100\,\mathrm{m}$ at cloud base).

The heterogeneous nucleation of cloud ice is possible for temperatures below $T = 267.15\,\mathrm{K}$ and the inital ice crystal number concentration N_i is based on an updated version of the classical Fletcher-formula (Fletcher et al., 1962)

$$N_i(T) = N_0^i e^{0.2(T_0 - T)}, \qquad [3.16]$$

where $N_0^i = 100\,\mathrm{m}^{-3}$ and T_0 is the temperature at the freezing point (273.15 K). Heterogeneous nucleation of cloud ice requires water saturation for $T > 248.15\,\mathrm{K}$ and ice saturation for lower temperatures. To calculate the initial ice mass mixing ratio an initial mean ice crystal mass of $10^{-12}\,\mathrm{kg}$ is assumed (Doms et al., 2011).

4. Realization of the Aerosol-Cloud Interaction

To study the interaction of aerosol particles with clouds additional processes have to be included in COSMO-ART. These are in detail the activation of aerosol particles, the homogeneous freezing of liquid aerosol particles, and the heterogeneous freezing on solid aerosol particles, which couple the simulated aerosol particles with the cloud hydrometeors. Furthermore, comprehensive descriptions of the cloud microphysical processes and the cloud optical properties must be introduced, which consider the variability of the hydrometeor size distributions. In Bangert (2008) the treatment of the processes involved in the interaction of aerosol particles with the formation of precipitation in warm clouds was presented.

In this thesis, new comprehensive processes were included in COSMO-ART, which enable the investigation of aerosol particles on cloud droplet and ice crystal number concentration as well as the subsequent impact on cloud microphysical processes and cloud optical properties. Figure 4.1 gives a brief overview of the processes described in this chapter.

4.1. Aerosol Activation

In Section 2.2.3 the basics concepts of the aerosol activation were explained, which describe the growth of a specific aerosol particle to the size of a cloud droplet for a given saturation ratio with respect to water,

To realize the process of aerosol activation in an atmospheric numerical model system the CCN-spectra of the simulated aerosol particles has to be calculated with respect to the chemical composition and size distribution of the aerosol modes. In three dimensional atmospheric models with vertical resolutions of several hundred meter, the evolution of the supersaturation during the formation of the cloud can not be resolved explicitly. As a consequence, parameterizations have to be used to derive the maximum

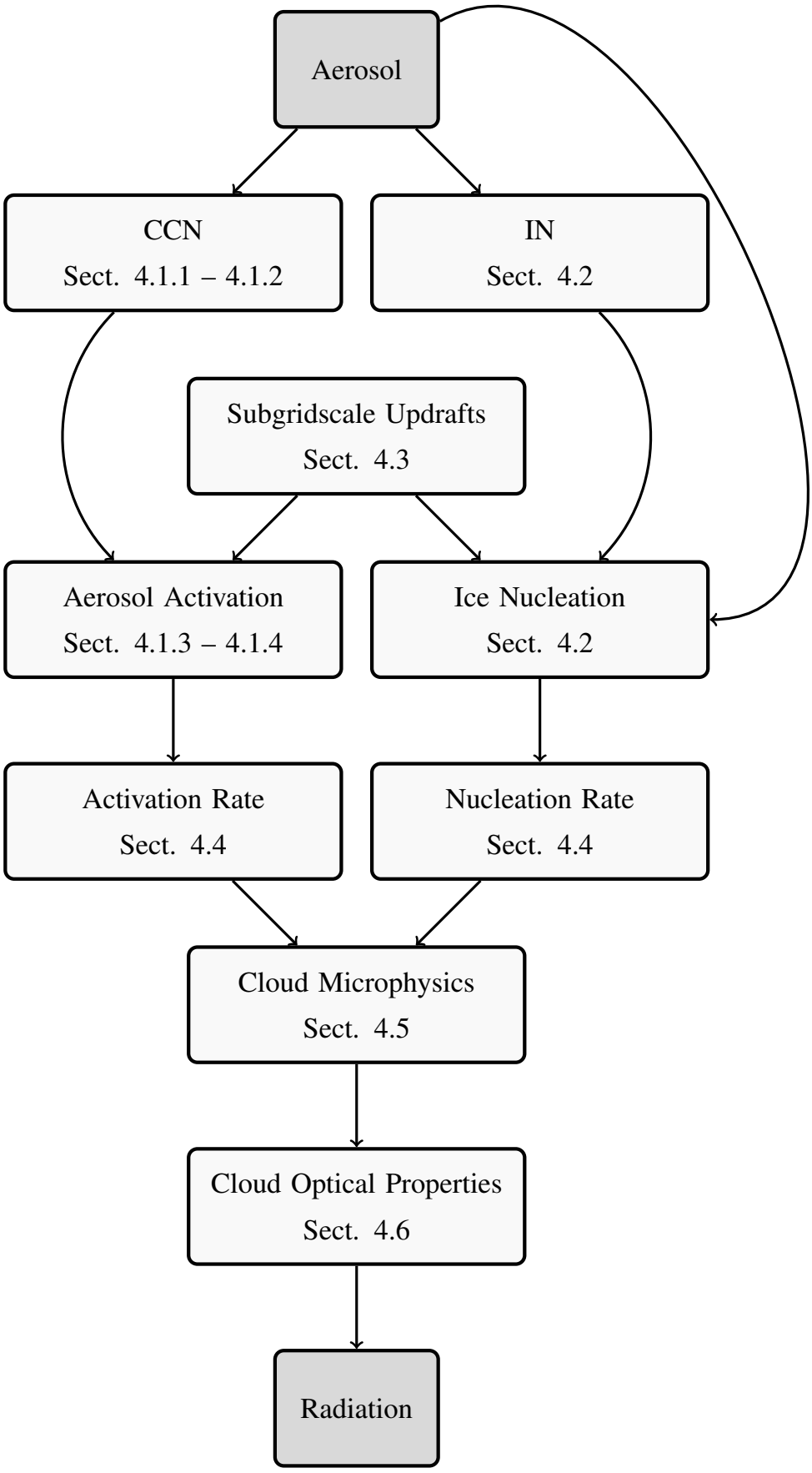

Fig. 4.1.: Overview of the new aerosol-cloud-radiation coupling in COSMO-ART and the corresponding references. Dark gray boxes are already implemented in the standard COSMO-ART version.

supersaturation that occurs during cloud formation (Ghan et al., 2011). In these parameterizations the competition of the aerosol particles for water vapor has to be considered.

4.1.1. Critical Supersaturation of an Internally Mixed Soluble Aerosol Particle

The critical supersaturation s_{crit} at which an aerosol particle gets activated can be related to the dry particle diameter by Eq. 2.34. For internally mixed particles s_{crit} can be calculated in terms of average chemical properties

$$s_{\text{crit}} = \left(\frac{4A^3 \rho_w \overline{M_s}}{27 \overline{\nu_s \rho_s} \varepsilon_s M_w D_p^3} \right)^{1/2}, \qquad [4.1]$$

where ρ_s is the density of the soluble particle fraction and $\varepsilon_s = V_s/V_p$ with V_p the total volume of the particle including insoluble components.

Following Hänel (1976) the average properties of the soluble fraction are given by

$$\overline{\nu_s} = \frac{1}{n_s} \sum_i \nu_{s,i} n_{s,i} = \frac{1}{\sum_i n_{s,i}} \sum_i \nu_{s,i} n_{s,i} = \frac{1}{\sum_i m_{s,i}/M_i} \sum_i \nu_{s,i} \frac{m_{s,i}}{M_i}, \qquad [4.2]$$

$$\overline{M_s} = \frac{m_s}{n_s} = \frac{\sum_i m_{s,i}}{\sum_i m_{s,i}/M_i}, \qquad [4.3]$$

$$\overline{\rho_s} = \frac{m_s}{V_s} = \frac{\sum_i m_i}{\sum_i m_i/\rho_i}, \qquad [4.4]$$

where n_s is the total number of moles of solute, m_s is the total mass of solute, $m_{s,i}$ is the mass of solute component i, $n_{s,i}$ is the number of moles of solute component i, M_i is the molar mass of component i, and ρ_i is the density of component i. In COSMO-ART m_i of Sulfate, Nitrate, Ammonium, Sodium Chloride, organic compounds, soot and mineral dust are calculated. Sulfate, Nitrate, Ammonium and the organic compounds are treated as fully water soluble, and soot and mineral dust as insoluble.

For the calculation of $\sigma_{v,w}$ in A (Eq. 2.28) the surface tension of pure water is used, which is a function of temperature (e.g. Seinfeld and Pandis, 2006; Pruppacher and Klett, 1997). One should note, that effects of solute and of organic films on $\sigma_{v,w}$ are neglected.

Equation 4.1 was derived with the assumption that the volume of water in the droplet at the point of activation is much larger than the volume of the particle including the insoluble core. This is the case for particles with only a small insoluble fraction, where D_{crit} is much larger than D_p.

For insoluble particles, for example mineral dust, s_{crit} can be derived by Eq. 2.36 ($s_{\text{crit}} = CD_p^c$) as a function of D_p. Kumar et al. (2009) specified c and C in Eq. 2.36 by a multivariate regression of the results of numerical solutions of the equations in Sect. 2.2.2 for a set of possible input parameters:

$$C = 10^{-8} A_{\text{FHH}}^{Q_1} \left(\frac{-21}{A_{\text{FHH}}^{Q_2}} + \frac{1.3}{B_{\text{FHH}}^{Q_3}} + \frac{Q_4}{B_{\text{FHH}}^{Q_5}} \right), \quad [4.5]$$

$$c = A_{\text{FHH}}^{P_1} \left(\frac{P_2}{B_{\text{FHH}}^{P_3}} - \frac{P_4}{B_{\text{FHH}}^{P_5}} \right), \quad [4.6]$$

where Q_1,Q_2,Q_3,Q_4, and Q_5 as well as P_1, P_2, P_3, P_4, and P_5 are fitting constants and are given in Kumar et al. (2009).

In case of large insoluble particles with a hygroscopic coating, the volume of the solid particle can not be neglected (D_p is in the order of D_{crit}). Additionally, the influence of adsorption on s_{crit} has to be considered. Consequently, s_{crit} is derived by a numerical solution of Eq. 2.33 using the bisection method (Kumar et al., 2009, 2011).

4.1.2. CCN-spectrum of a Multi Modal Aerosol Size Distribution

The CCN-sepctrum CCN(s) (Eq. 2.38) of a multi modal aerosol size distribution can be calculated by

$$\text{CCN}(s) = \int_0^s n_N^*(s')ds' = \int_0^s \sum_l n_{N,l}^*(s')ds'. \quad [4.7]$$

where $n_{N,l}^*$ has to be derived for a log-normal number size distribution (Eq. 3.2) of the mode l. In Section 2.2.3 the relation of s_{crit} with the dry particle diameter D_p was discussed. For the ratio $D_p/\overline{D_{p,l}}$ of the log-normal number size distribution, we get with Eq. 2.36

$$\frac{D_p}{\overline{D_{p,l}}} = \left(\frac{s_{\text{crit}}}{\overline{s_{crit,l}}} \right)^{\frac{1}{c}}, \quad [4.8]$$

where $\overline{s_{crit,l}}$ is the critical supersaturation for activation of the median diameter of $n_{N,l}(D_p)$, and c is an exponent that depends on the used activation theory. For soluble particles the Köhler theory is used and c equals $-3/2$. For solid particles the FHH theory is used and c varies between -0.8 and -1.2 (Kumar et al., 2009) and is calculated by Eq. 4.6. For large solid particles with a soluble coating a fixed $c = -1.33$ is used, which is consistent with values of c derived from field measurements (Kumar et al., 2009).

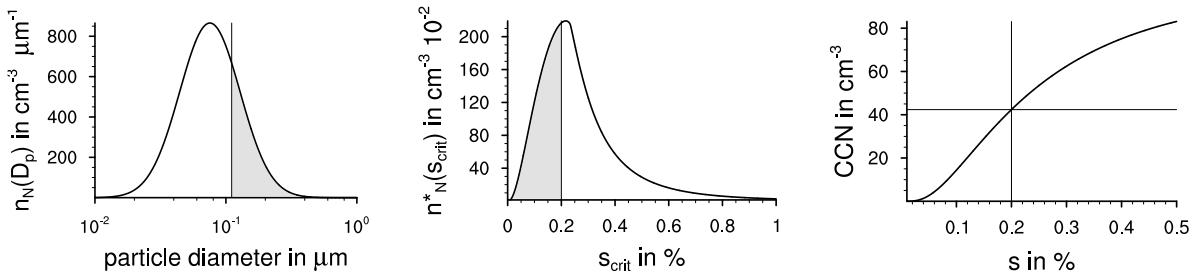

Fig. 4.2.: Number density size distribution of a log-normal aerosol mode containing pure sulfate particles (left, Eq. 3.2) with $N_l = 100\,\mathrm{cm}^{-3}$, $\overline{D_{p,l}} = 0.1\,\mu\mathrm{m}$, and $\sigma_l = 1.7$ together with the corresponding $n^*_{N,l}(s_{\mathrm{crit}})$ (middle, Eq. 4.9) and the resulting CCN spectrum (right, Eq. 4.10). The gray areas highlight the fraction of particles that activate at 0.2 % supersaturation. Note that the gray area in the left figure is not directly proportional to the number of activated particles because of the log-scaling of the x-axis.

Substituting Eq. 4.8 in the definition of n^*_N (Eq. 2.37), we get for a log-normal size distribution (Eq. 3.2)

$$n^*_{N,l}(s_{\mathrm{crit}}) = -\frac{1}{s_{\mathrm{crit}}}\frac{N_l}{c\sqrt{2\pi}\ln\sigma_l}\exp\left(-\frac{\ln^2\left(\frac{s_{\mathrm{crit}}}{\overline{s_{crit,l}}}\right)^{\frac{1}{c}}}{2\ln^2\sigma_l}\right). \qquad [4.9]$$

Substituting $n^*_{N,l}(s_{\mathrm{crit}})$ in Eq. 4.7 and performing the integration, we get the CCN-sepctrum of a multi modal log-normal aerosol size distribution

$$\mathrm{CCN}(s) = \sum_l \frac{N_l}{2}\mathrm{erfc}\left(\frac{\ln\left(\frac{s}{\overline{s_{crit,l}}}\right)}{c\sqrt{2}\ln\sigma_l}\right), \qquad [4.10]$$

where erfc is the complementary error function:

$$\mathrm{erfc}(y) = 1 - \frac{2}{\sqrt{\pi}}\int_0^y e^{-y'^2}dy' \qquad [4.11]$$

4.1.3. Parametrization of Maximum Supersaturation

To calculate the number of activated aerosol particles with Eq. 4.10, the maximum supersaturation s_{max} during cloud formation has to be calculated. In Section 2.2.4 it was shown, that s_{max} can be derived by solving the saturation balance equation Eq. 2.44 of an ascending air parcel. In the following, the mechanistic parameterizations used to solve Eq. 2.44 and to determine s_{max} are introduced.

Parameterization of Abdul-Razzak and Ghan (2000)

Abdul-Razzak and Ghan (2000) developed a parameterization for $s_{\max}$ based on the work of Twomey (1959) (Sect 2.2.5) that considers multiple log-normal aerosol size distributions. They use adjustment parameters derived by a detailed numerical parcel simulation to combine the lower and upper bound estimates for the condensation integral (Eq. 2.51 and Eq. 2.54) in a single equation, which can be directly applied to estimate $s_{\max}$:

$$s_{\max} = \left\{ \sum_l \frac{1}{\overline{s_{crit,l}}^2} \left[P_{3,l} \left(\frac{P_1}{P_{2,l}} \right)^{\frac{3}{2}} + P_{4,l} \left(\frac{\overline{s_{crit,l}}^2}{P_{2,l} + 3P_1} \right)^{\frac{3}{4}} \right] \right\}^{-\frac{1}{2}}, \qquad [4.12]$$

where four dimensionless parameters are introduced:

$$P_1 = \frac{2A}{3} \left(\frac{\alpha w}{\Lambda} \right)^{\frac{1}{2}},$$
$$P_{2,l} = \frac{\rho_a (\alpha w/\Lambda)^{\frac{3}{2}}}{2\pi \rho_w \gamma N_l},$$
$$P_{3,l} = 0.5 e^{(2.5 \ln^2 \sigma_l)},$$
$$P_{4,l} = 1 + 0.25 \ln \sigma_l.$$

Since Eq. 4.12 was derived by a combination of the lower and upper bound regimes with parameters ($P_{3,l}$ and $P_{4,l}$) averaged over a set of conditions, the accuracy of the parameterization decreases for conditions that significantly deviate from the average, for example for very large aerosol particles.

Parameterization of Nenes and Seinfeld (2003); Fountoukis and Nenes (2005)

Nenes and Seinfeld (2003) and Fountoukis and Nenes (2005) introduced the concept of "population splitting" in which the growing aerosol droplets are treated as two separate populations. As a consequence, $s_{\max}$ can be determined almost without empirical information or correlations. In the first population the droplets experience significant growth between their activation and $t_{\max}$ and in the second they do not. Hence, the upper and lower bound conditions of Twomey (1959) can be directly used to approximate the condensation integral Eq. 2.48 by the condensational growth of the two populations:

$$I(0, s_{\max}) = I_1(0, s_{\text{part}}) + I_2(s_{\text{part}}, s_{\max}), \qquad [4.13]$$

where s_{part} is the "partitioning critical supersaturation", which separates the two aerosol populations. $I_1(0, s_{\text{part}})$ represents the contribution of aerosol droplets that grow significantly after activation and is equal to the integral in Eq. 2.51, and $I_2(s_{\text{part}}, s_{\max})$ represents the contribution of droplets that do not experience significant growth after activation and is equal to the integral in Eq. 2.54 of Twomey (1959).

Nenes and Seinfeld (2003) defined s_{part} as the critical supersaturation of a particle s_{crit}, for which the diameter at their activation equals the subsequent growth of the particle:

$$D^2(\tau) = 2\Lambda \int_{\tau}^{t_{\max}} s dt. \qquad [4.14]$$

Substituting the r.h.s with Eq. 2.50 and the l.h.s with Eq. 2.53 we get

$$\frac{4A^2}{9s_{\text{part}}^2} = \frac{\Lambda}{\alpha w}\left(s_{\max}^2 - s_{\text{part}}^2\right). \qquad [4.15]$$

A solution for s_{part} can be found using the discriminant Δ of Eq. 4.15, which is

$$\Delta = \left(s_{\max}^4 - \frac{16A^2\alpha w}{9\Lambda}\right), \qquad [4.16]$$

where Δ expresses the extent of kinetic limitations throughout the droplet population. The activation of a population of aerosol droplets is not an instantaneous process. The aerosol droplets need time to grow to D_{crit}, before they get activated. Small aerosol droplets with high s_{crit} may not have enough time available for which $s > s_{\text{crit}}$ to grow to D_{crit}, though $s_{\max}$ is larger than s_{crit}. Additionally, large aerosol droplets have low values for s_{crit} but their growth is inertial due to their large size. Hence, they have not much time for growth after reaching D_{crit} or even do not get explicitly activated. These effects limit the growth of the droplets and are referred to as "kinetic" effects or "kinetic limitation" (Nenes et al., 2001). Nenes and Seinfeld (2003) point out, that $\Delta = 0$ marks a boundary between two droplet growth regimes, one where most CCN are free from kinetic limitations ($\Delta > 0$) and one in which kinetic limitations are dominant ($\Delta < 0$). For $\Delta > 0$ we can solve Eq. 4.15 and get

$$s_{\text{part}} = s_{\max}\left\{\frac{1}{2}\left[1 + \left(1 - \frac{16A^2\alpha w}{9\Lambda s_{\max}^4}\right)^{1/2}\right]\right\}^{1/2}. \qquad [4.17]$$

For $\Delta < 0$ Eq. 4.15 has no real solution. Nenes and Seinfeld (2003) derived an empirical correlation based on comprehensive parcel simulations with a microphysical model:

$$s_{\text{part}} = s_{\max} \min\left\{\frac{2\cdot 10^7 A}{3} s_{\max}^{-0.3824}, 1.0\right\}. \qquad [4.18]$$

Finally, we can use s_{part} to calculate the condensation integral (Eq. 4.13) taking into account the kinetic limitations of droplet growth.

To determine $s_{\max}$ an iterative procedure is used. At first Δ, s_{part}, and $I(0, s_{\max})$ are calculated for $s_{\max} = 0.5$ and $s_{\max} = 10^{-5}$ and used in the saturation balance equation:

$$\frac{2\alpha w \rho_a}{\pi \gamma \rho_w} - \Lambda s_{\max} I(0, s_{\max}) \stackrel{!}{=} 0. \qquad [4.19]$$

If the balance equation is not fulfilled, a better guess for $s_{\max}$ is made using the bisection method. The value of $s_{\max}$ is iterated until the balance equation is fulfilled, in detail until $s_{\max}$ is determined with a accuracy of approximately $10^{-4}\,\%$.

Extensions of the Parameterization of Nenes and Seinfeld (2003); Fountoukis and Nenes (2005)

In the derivation of the supersaturation balance equation (Eq. 4.19) it was assumed that the diffusivity of water vapor onto the droplets is independent of the droplet size. This causes an overestimation of the growth rate and hence an underestimation of $s_{\max}$, because D'_v decreases for droplets smaller than approximately $10\,\mu$m (Eq. 2.16). Therefore, a size-averaged diffusivity $\overline{D'_v}$ for the growth of the droplet population was included by Fountoukis and Nenes (2005) in the solution of Eq. 4.19:

$$\overline{D'_v} = \frac{D_v}{D_{\text{big}} - D_{\text{low}}} \left[D_{\text{big}} - D_{\text{low}} - \frac{2D_v}{\alpha_c} \sqrt{\frac{2\pi M_w}{RT}} \ln \left(\frac{D_{\text{big}} + \frac{2D_v}{\alpha_c}\sqrt{\frac{2\pi M_w}{RT}}}{D_{\text{low}} + \frac{2D_v}{\alpha_c}\sqrt{\frac{2\pi M_w}{RT}}} \right) \right], \qquad [4.20]$$

where $D_{\text{big}} = 5\,\mu$m is the upper size bound and $D_{\text{low}} = \min\left\{0.207683\alpha_c^{-0.33048}, 5.0\right\}$ is the lower size bound for the average given in μm. For the calculation of $\overline{D'_v}$ and D_{low}, $\alpha_c = 0.06$ is used.

The contribution of large solid particles activated by adsorption to the condensation integral (Eq. 4.13) of Nenes and Seinfeld (2003) was introduced by Kumar et al. (2009). In contrast to solution droplets, where $D_{\text{crit}} \gg D_p$, D_{crit} of large solid particles (e.g. mineral dust) is in the order of their dry diameter D_p. Therefore, the water amount required for activation is much smaller. Thus, we can use the lower bound of Twomey (1959) (Eq. 2.49) and calculate the contribution of activated large solid particles by Eq. 2.51

$$I_{\text{FHH}}(0, s_{\max}) = \int_0^{s_{\max}} \left(\frac{\Lambda}{\alpha w}\right)^{1/2} \left(s_{\max}^2 - s(\tau)^2\right)^{1/2} n_N^*(s) ds. \qquad [4.21]$$

For the growth of solution droplets and solid particles Eq. 4.13 becomes

$$I(0, s_{\max}) = I(0, s_{\text{part}}) + I(s_{\text{part}}, s_{\max}) + I_{\text{FHH}}(0, s_{\max}). \quad [4.22]$$

Very large aerosol particles ($D_p > 0.5\,\mu$m, e.g. sea salt particles), frequently referred to as "giant CCN", have low s_{crit}, but grow slowly in comparison to small particles. As a consequence they do not grow substantially during cloud formation and are not able to attain D_{crit}. Even tough the parameterization of Nenes and Seinfeld (2003) considers the inertial-limitations of droplet growth with their concept of population splitting, the size of the particles at cloud base (at saturation) is neglected in comparison to the subsequent growth of the particles. This assumption causes increasingly-large errors as the dry particle size increases. As a consequence, $s_{\max}$ is overestimated in presence of very large aerosol particles.

Barahona et al. (2010b) present an extension of the parameterization by Nenes and Seinfeld (2003) that includes an additional contribution of large inertially-limited aerosol particles to the condensation rate. The condensation integral (Eq. 4.13) becomes

$$I(0, s_{\max}) = I(0, s_{\text{part}}) + I(s_{\text{part}}, s_{\max}) + N_{\text{sat}}\overline{D_{\text{sat}}}, \quad [4.23]$$

where $\overline{D_{\text{sat}}}$ is the mean droplet diameter of the aerosol distribution at saturation and N_{sat} the corresponding number concentration of droplets, both derived for particles with $s_{\text{crit}} < s_{\text{part}}$, i.e. particles that experience kinetic limitations (Nenes and Seinfeld, 2003). The droplet diameter at saturation D_{sat} is calculated with the Köhler theory (Eq. 2.27 for $s = 0$) as a function of the dry particle diameter or alternatively of s_{crit}

$$D_{\text{sat}} = \left(\frac{B}{A}\right)^{1/2} = \frac{2A}{3\sqrt{3}s_{\text{crit}}} = \left(\frac{\nu_s \rho_s M_w}{A \rho_w M_s}\right)^{1/2} D_p^{3/2}. \quad [4.24]$$

N_{sat} is calculated by

$$N_{\text{sat}} = \int_{D_{sat,min}}^{\infty} n(D_{\text{sat}}) dD_{\text{sat}}, \quad [4.25]$$

where $D_{sat,min} = 2A/3\sqrt{3}s_{\text{part}}$ is the equilibrium diameter at saturation of the smallest particle that activates at s_{part}, and $n(D_{\text{sat}})$ is the number size distribution of droplets at saturation. $n(D_{\text{sat}})$ is calculated from the dry aerosol size distribution with Eq. 4.24 (Barahona et al., 2010b). $\overline{D_{\text{sat}}}$ is given by

$$\overline{D_{\text{sat}}} = \frac{1}{N_{\text{sat}}} \int_{D_{sat,min}}^{\infty} D_{\text{sat}} n(D_{\text{sat}}) dD_{\text{sat}} \quad [4.26]$$

The approach of Barahona et al. (2010b) is used to account for water vapor depletion on pre-existing cloud droplets in case of in-cloud activation in a pragmatic way. At this, the cloud droplets are treated as giant sulfate particles ($D_p = 2\,\mu$m) in the activation parameterization. As a consequence, they are treated as inertially-limited particles with a diameter of approximately $34\,\mu$m at water saturation. Thus, their growth contributes to the condensation integral (Eq. 4.23). This enables a more accurate parameterization of $s_{\max}$ inside clouds depending on the aerosol population and the pre-existing cloud droplet number concentration.

4.1.4. Number Concentration of Activated Particles

Following Sect. 4.1.1 to 4.1.3, the number concentration of activated particles is calculated by

$$N_c^* = \mathrm{CCN}(s_{\max}) = \mathrm{CCN}(w, N_l, \overline{D}_{d,l}, \overline{\nu_{s,l}}, \overline{M_{s,l}}, \overline{\rho_{p,l}}) \qquad [4.27]$$

as a function of the varying chemical ($\overline{\nu_{s,l}}, \overline{M_{s,l}}, \overline{\rho_{p,l}}$) and physical ($N_l$, $\overline{D}_{d,l}$) aerosol properties and the updraft velocity (w).

4.2. Ice Nucleation

The nucleated number concentration of ice crystals N_i^* is calculated using the parameterization of Barahona and Nenes (2008, 2009a,b), which is based on the framework of an ascending Lagrangian air parcel (see Sect. 2.2.4). Competition between homogeneous and heterogeneous freezing is explicitly considered in the calculation of the ice supersaturation s_i. In doing so the dependency of N_i^* on the conditions of cloud formation (i.e., T, p), updraft velocity, deposition coefficient, and soluble and insoluble aerosol concentrations is explicitly resolved. N_i^* is given by

$$N_i^* = \begin{cases} N_{\mathrm{hom}} + N_{\mathrm{het}}(s_{\mathrm{hom}}) & ; N_{\mathrm{het}}(s_{\mathrm{hom}}) < N_{\mathrm{lim}} \\ N_{\mathrm{het}}(s_{i,\max}) & ; N_{\mathrm{het}}(s_{\mathrm{hom}}) \geq N_{\mathrm{lim}} \end{cases}, \qquad [4.28]$$

where $s_{i,\max}$ is the maximum supersaturation that develops during the nucleation pulse, and N_{hom} and N_{het} are the number of ice crystals forming from homogeneous and heterogeneous freezing, respectively. s_{hom} is the homogeneous freezing threshold, which is defined by Barahona and Nenes (2008) as the average maximum s_i that occurs during a

homogeneous freezing pulse with a nucleation rate of $J(s_{\text{hom}}) = 10^{16}\,s^{-1}\,m^{-3}$ and is calculated with the parameterization of Koop et al. (2000). N_{lim} is the IN concentration that completely inhibits homogeneous nucleation ($s_{i,\max} < s_{\text{hom}}$) and sets the limit between combined heterogeneous-homogeneous freezing and pure heterogeneous freezing only.

The heterogeneous freezing spectrum of Phillips et al. (2008) is used for $N_{\text{het}}(s_i)$. It provides the contribution of individual aerosol species (dust, black carbon, and organics) and freezing mechanisms (e.g. immersion and deposition) to $N_{\text{het}}(s_i)$. A base freezing spectrum $N'_{\text{het}}(s_i,T)$, which is derived from several field campaign data sets, is used and the contribution of the dust and soot particles with a diameter larger than $0.1\,\mu$m to $N_{\text{het}}(s_i)$ are scaled to their surface area:

$$\begin{aligned} N_{\text{het}}(s_i) = \; & \sum_{dx=da,db,dc} \left(\int_{0.1\,\mu m}^{\infty} n_{N,dx} \left[1 - e^{-H_{dx}\xi\frac{2}{3}\frac{N'_{\text{het}}(s_i,T)}{\Omega^*_d}\pi\overline{D}^2_{dx}} \right] dD_{dx} \right) \\ & + \int_{0.1\,\mu m}^{\infty} n_{N,so} \left[1 - e^{-H_{so}\xi\frac{1}{3}\frac{N'_{\text{het}}(s_i,T)}{\Omega^*_{so}}\pi\overline{D}^2_{so}} \right] dD_{so} \end{aligned} \qquad [4.29]$$

where $H_{dx}(s_i,T)$ and $H_{so}(s_i,T)$ are empirical fractions representing the efficiency of heterogeneous freezing of dust and soot as a function of saturation with respect to water. Approaching water saturation, condensation and immersion freezing are enhanced, which is represented by a strong increase in $H_{dx}(s_i,T)$ and $H_{so}(s_i,T)$ up to 1 at water saturation. ξ equals 1 for temperatures below -5 °C and zero for temperatures above -2 °C with interpolated values in between (Phillips et al., 2008). Ω_d and Ω_{so} are the baseline surface area mixing ratios given in (Phillips et al., 2008) and $\overline{D}_{dx}$ and $\overline{D}^2_{so}$ are the median diameters of the dust modes and the soot mode. A detailed definition of the parameters is given in appendix B.

For pure heterogeneous freezing ($N_{\text{het}} \geq N_{\text{lim}}$ or $T > 235$ K; Eq. 4.28) homogeneous freezing is not possible and N_i^* equals $N_{\text{het}}(s_{i,\max})$. A simplified s_i balance equation (Barahona and Nenes, 2009b) is solved numerically to determine $s_{i,\max}$:

$$\frac{N_{\text{het}}(s_{i,\max})}{N^{\diamond}} = \frac{1}{\sqrt{\Delta s^*_{\text{char}}\big|_{s_{i,\max}}}} \frac{(1+s_{i,\max})}{s_{i,\max}} e^{\frac{2}{\lambda s_{i,\max}}}. \qquad [4.30]$$

where $\Delta s^*_{\text{char}}|_{s_i}$ is a function of the slope of the heterogeneous freezing spectrum at s_i. $N^{\diamond}$ and λ depend on cloud characteristic like updraft velocity and temperature, for instance. The individual parameters are defined in appendix B.

Homogeneous freezing is inhibited if the resulting $s_{i,\max}$ derived from Eq. 4.30 equals s_{hom}. Hence, N_{lim} is given by

$$N_{\text{lim}} = \frac{N^{\diamond}}{\sqrt{\Delta s^{*}_{\text{char}}}\big|_{s_{\text{hom}}}} \frac{(1+s_{\text{hom}})}{s_{\text{hom}}} e^{\frac{2}{\lambda s_{\text{hom}}}}, \qquad [4.31]$$

The homogeneous contribution to N_i^* for combined homogeneous and heterogeneous freezing ($N_{\text{het}} < N_{\text{lim}}$ and $T \leq 235$ K; Eq. 4.28) is given by (Barahona et al., 2010b)

$$N_{\text{hom}} = \begin{cases} N_0 e^{-f_c}\left(1-e^{-f_c}\right) & f_c < 0.6 \\ N_0\left[1+e^{\left(\frac{9-2f_c}{7}\right)}\right]^{-1} & f_c \geq 0.6 \end{cases}, \qquad [4.32]$$

where N_0 is the number concentration of the supercooled liquid droplet population and f_c is the droplet freezing fraction. N_0 equals the sum of the number concentration of the soluble aerosol modes (Table 3.1) which are assumed to deliquesce during ice cloud formation. The fraction of droplets freezing homogeneously in presence of IN is calculated by (Barahona et al., 2010b)

$$f_c = f_{c,\text{hom}}\left[1-\left(\frac{N_{\text{het}}(s_{\text{hom}})}{N_{\text{lim}}}\right)^{3/2}\right]^{3/2}, \qquad [4.33]$$

where $f_{c,\text{hom}}$ is the freezing fraction in absence of IN (Barahona and Nenes, 2008)

$$f_{c,\text{hom}} = \frac{\rho_a}{\rho_i}\frac{k_{\text{hom}}^{1/2}}{\gamma_i N_0}\left(\frac{2\alpha w(s_{\text{hom}}+1)}{\pi\overline{\Lambda}_i s_{\text{hom}}}\right)^{3/2}. \qquad [4.34]$$

The parameters k_{hom} and $\overline{\Lambda}_i$ are specified in appendix B.

4.3. Subgridscale Updrafts

Even though regional scale models are able to simulate individual cloud systems, they cannot explicitly resolve the updraft velocities which control nucleation of ice and droplets (Tonttila et al., 2011). Therefore, parameterizations of the subgrid-scale vertical velocity must be applied to address this issue.

Two different methods are introduced in COSMO-ART. In the first, an effective updraft is calculated based on the turbulent kinetic energy TKE and the grid scale updraft w to account for the contribution of sub-grid scale updrafts following Lohmann et al. (1999b):

$$\overline{w_e} = w + a \cdot \sqrt{TKE}, \qquad [4.35]$$

where a is a factor that has to be chosen. Following Lohmann et al. (1999a) $a = 0.7$ is used. One should note that averaging the positive part of a normally distributed probability density function of sub-grid scale vertical velocities w' that has a standard deviation equal to $\sqrt{TKE}$ and is centered close to 0, one gets $\overline{w'} = \sqrt{2/\pi}\sqrt{TKE} = 0.79\sqrt{TKE}$ for the mean updraft velocity. The activation parameterization is then applied using $\overline{w_e}$ as an input parameter.

$$\overline{N_c^*} \approx N_c^*(\overline{w_e}, [\ldots]) \quad [4.36]$$

$$\overline{N_i^*} \approx N_i^*(\overline{w_e}, [\ldots]). \quad [4.37]$$

Because the number of nucleated droplets and crystals is a non linear function of the updraft velocity using an average updraft in the parameterizations of activation and ice nucleation will result in inaccurate numbers of activated particles and nucleated ice crystals. Consequently, a second approach was introduced, which calculates activation and ice nucleation for a Gaussian probability distribution function $P_w(w')$ of sub-grid scale vertical velocities following Morales and Nenes (2010):

$$P_w(w') = \frac{1}{\sqrt{2\pi}\sigma_w} e^{-\frac{(w'-w)^2}{2\sigma^2}}. \quad [4.38]$$

The mean of $P_w(w')$ is set equal to the grid scale updraft w and the standard deviation σ_w is calculated as the square root of the turbulent kinetic energy. The parameterizations are then calculated explicitly for w'. Subsequently, a weighted mean of the activated particles and nucleated ice crystals is calculated by numerically calculating the integrals

$$\overline{N_c^*} = \frac{\int_0^\infty N_c^*(w', [\ldots]) P_w(w') dw'}{\int_0^\infty P_w(w') dw'}, \quad [4.39]$$

$$\overline{N_i^*} = \frac{\int_0^\infty N_i^*(w', [\ldots]) P_w(w') dw'}{\int_0^\infty P_w(w') dw'}. \quad [4.40]$$

4.4. Activation and Nucleation Rates

The activation and ice nucleation parameterizations, which were included in the model framework (Sect. 4.1 to Sect. 4.3), enable the calculation of number concentrations of activated aerosol particles and nucleated ice crystals as a function of atmospheric state and aerosol properties with a set of diagnostic equations (Eq. 4.39, Eq. 4.40, Eq. 4.27 and Eq. 4.28). Hence, they cannot be a used directly in the budget equations of cloud

water droplets and ice crystals. To derive a nucleation rate of cloud droplets $S_{N_c}^{\text{act}}$ and ice crystals $S_{N_i}^{\text{nuc}}$ several assumptions were made.

For the nucleation of clouds droplets three different cases were defined for which the nucleation of cloud droplets can occur. In case of an already existing cloud the nucleation rate of droplets at the cloud base (lowest layer with $s_g > 0$) is calculated on the basis of advection and turbulent diffusion of particles into the cloud base

$$S_{N_c}^{\text{act}} = -\frac{\partial}{\partial z}\overline{N_c^*}(s_{\max})w + \frac{\partial}{\partial z}K\frac{\partial}{\partial z}\overline{N_c^*}(s_{\max}), \qquad \text{(cloud base case)} \qquad [4.41]$$

where K is the turbulent diffusion coefficient. If the cloud is newly formed or N_c is lower than $10\,\text{cm}^{-3}$ as well as for in-cloud activation of aerosol particles above the cloud base the nucleation rate of cloud droplets is given by

$$S_{N_c}^{\text{act}} = \max([\overline{N_c^*} - N_c]/\Delta t, 0), \qquad \text{(new cloud and in-cloud case)} \qquad [4.42]$$

where Δt is the time step used and N_c is the cloud droplet number concentration before droplet nucleation. In-cloud activation is calculated only if the parameterization of (Nenes et al., 2001; Fountoukis and Nenes, 2005) is used. In this case the growth of the existing cloud droplets can be considered in the parameterization of $s_{\max}$ using the extension of Barahona et al. (2010b) (Eq. 4.23) for the growth of large inertially-limited aerosol particles. One should note that aerosol particles that have been activated at the cloud base are considered in the calculation of the in-cloud activation. This can potentially cause an overestimation of the number of activated droplets inside the cloud, especially for low aerosol number concentrations. Nevertheless, in-cloud activation is accounted for to avoid unrealistic low N_c in case of convective cloud systems with strong updrafts inside the clouds. For all cases the maximum number concentration of cloud droplets after nucleation is restricted by the total number concentration of aerosol particles.

The parameterization of the nucleation rate of ice crystals by the freezing of aerosol particles follows Reisner and Bruintjes (1998); Seifert and Beheng (2006b) and others by adjusting N_i with the parameterized number concentration of nucleating ice crystals $\overline{N_i^*}$

$$S_{N_i}^{nuc} \approx \max\left(\frac{\overline{N_i^*} - N_i}{\Delta t}, 0\right). \qquad [4.43]$$

In doing so, one avoids unrealistic high values of N_i formed by the successive calculation of the ice nucleation parameterization.

4.5. Cloud Microphysics

A comprehensive two-moment bulk microphysical scheme (Seifert and Beheng, 2006b; Seifert et al., 2006; Noppel et al., 2006; Blahak, 2008) was included in COSMO-ART to further improve the representation of cloud microphysics and to enable the simulation of aerosol impacts on ice clouds. This scheme distinguishes six hydrometeor categories (cloud drops, cloud ice, rain, snow, graupel, and hail) and represents each particle type by its respective number and mass concentration, the zeroth and first moment of the number size distribution with respect to the droplet mass respectively . A (generalized) gamma size distribution is used for each hydrometeor class, where the so-called shape parameters are held constant during the simulation.

For the warm clouds, the scheme considers autoconversion of cloud droplets to rain, accretion of cloud droplets by rain drops, self-collection of cloud and rain droplets, break-up of rain drops, and evaporation of rain drops. Condensational growth of cloud droplets is calculated with a saturation adjustment technique.

For the cold clouds, homogeneous and heterogeneous ice nucleation, diffusional growth of ice crystals, freezing of cloud and rain droplets, aggregation, self-collection, riming, conversion to graupel, melting, sublimation, shedding, and Hallett-Mossop ice multiplication are considered. The freezing of cloud and rain drops is calculated with a classical statistical approach based on an empirical relation for the freezing probability as a function of temperature (Seifert and Beheng, 2006b). Note that the freezing of cloud and rain droplets is independent of the simulated IN concentrations. This may introduce an underestimation of the glaciation of mixed phase clouds for high IN concentrations, but can be justified by a small fraction of cloud droplets originating from activated insoluble particles in the presented simulations (Sect. 6).

A detailed description of the cloud microphysical processes is given in Seifert and Beheng (2006b) and Blahak (2008), and a statistical analysis of the aerosol-cloud interaction for three summer seasons using the microphysics scheme is presented in Seifert et al. (2011).

Cloud microphysical processes and aerosol particles are coupled via the formation of cloud droplets and ice crystals by activation, and homogeneous and heterogeneous freezing of aerosol particles. The derivation of the activation rate $S_{N_c}^{act}$ and ice nucleation rate

$S_{N_i}^{nuc}$ is given in Sect. 4.4. The budget equations for cloud droplet number concentration and ice crystal number concentration are

$$\frac{\partial}{\partial t}N_c = -\nabla\cdot(\mathbf{v}N_c) + \nabla\cdot\mathbf{F}_{N_c} + \frac{\partial}{\partial z}\left(\overline{w_c^{\mathrm{sed}}}N_c\right) + S_{N_c}^{\mathrm{act}} + S_{N_c}, \qquad [4.44]$$

and

$$\frac{\partial}{\partial t}N_i = -\nabla\cdot(\mathbf{v}N_i) + \nabla\cdot\mathbf{F}_{N_i} + \frac{\partial}{\partial z}\left(\overline{w_i^{\mathrm{sed}}}N_i\right) + S_{N_i}^{\mathrm{nuc}} + S_{N_i}, \qquad [4.45]$$

where S_{N_c} stands for the microphysical sources and sinks of cloud droplets and S_{N_i} for the microphysical sources and sinks of ice crystals. $S_{N_c}^{\mathrm{act}}$ and $S_{N_i}^{\mathrm{nuc}}$ are calculated only if the grid-scale updraft w and the grid-scale supersaturation with respect to water and ice respectively are positive. For in-cloud activation, the vertical gradient of supersaturation in addition must be positive.

Note that in contrast to the standard cloud scheme of COSMO and its extension by Bangert (2008) the sedimentation of cloud droplets and ice crystals is considered.

4.6. Cloud Optical Properties

The cloud optical thickness τ_{cloud} depends on the size of cloud droplets and the water content of the cloud (Sect. 2.4.2). To simulate the impact of aerosol particles on the optical properties of clouds the varying droplet and ice crystal sizes have to be accounted for in the radiation scheme. For the calculation of the radiation transfer with GRAALS the extinction coefficient β_e, single-scattering albedo ω, and asymmetry factor g of the clouds are needed (Sect. 3.3).

With the restriction to the visible range of light, β_e for a liquid cloud is given by Eq. 2.80 as a function of the mass concentration of cloud water m_c and the effective radii $r_{c,\mathrm{eff}}$ of the cloud droplet distribution. The calculation of β_e for general conditions along with ω, and g needs the explicit solution of the Maxwell equations (e.g. with the so-called Mie solution for a spherical particle) because the particle size is in the same order as the wavelength of light. For an application in a three dimensional atmospheric model the Mie solution is computational too time consuming. As a consequence, parameterizations have to be used. In this study the parameterization of Hu and Stamnes (1993) is used to formulate the optical properties of liquid clouds as a function of $r_{c,\mathrm{eff}}$

$$\beta_{e,c}(\lambda) = m_c(a_1 r_{c,\text{eff}}^{b_1} + c_1), \quad [4.46]$$

$$\omega_c(\lambda) = 1 - (a_2 r_{c,\text{eff}}^{b_2} + c_2), \quad [4.47]$$

$$g_c(\lambda) = a_3 r_{c,\text{eff}}^{b_3} + c_3, \quad [4.48]$$

where a_y, b_y, and c_y for $y = 1,2,3$ are fitting constants derived by a Mie solution for different wavelengths and are given in Hu and Stamnes (1993). Note that in Hu and Stamnes (1993) Eq. 4.46 to Eq. 4.48 are given for specific input units of $r_{c,\text{eff}}$ and m_c.

For ice clouds the calculation of the optical properties is more complex in comparison to liquid clouds, due to the complex shape of the ice crystals. In this study the parameterization of Edwards et al. (2007) is used. Here β_e, ω, and g for ice clouds are parameterized as a function of an effective dimension $D_{i,\text{eff}}$ of the ice crystal population. Here, $D_{i,\text{eff}}$ represents the complex shape of the ice crystals. The definition of $D_{i,\text{eff}}$ is chosen to be consistent to the definition of the effective radii of cloud droplets and is given by $D_{i,\text{eff}} = 2r_{i,\text{eff}}$ assuming a spherical shape of the ice particles. For consistency with the formulation for liquid clouds, only $r_{i,\text{eff}}$ is used in the following. Based on the definition of $r_{c,\text{eff}}$ (Eq. 2.80), $r_{i,\text{eff}}$ is defined as

$$r_{i,\text{eff}} = \frac{M_{3,i}}{M_{2,i}} = \frac{1}{2} D_{i,\text{eff}}, \quad [4.49]$$

where $M_{3,i}$ and $M_{2,i}$ are the third and second moment of the ice crystal size distribution $n_{N,i}(r_i)$.

The optical properties of ice clouds are parameterized by

$$\beta_{e,i}(\lambda) = m_c(\acute{a}_0 + \acute{a}_1 (2r_{i,\text{eff}})^{-1} + \acute{a}_2 (2r_{i,\text{eff}})^{-2}), \quad [4.50]$$

$$\omega_i(\lambda) = 1 - (\acute{b}_0 + \acute{b}_1 (2r_{i,\text{eff}})^{1} + \acute{b}_2 (2r_{i,\text{eff}})^{2} + \acute{b}_3 (2r_{i,\text{eff}})^{3}), \quad [4.51]$$

$$g_i(\lambda) = \acute{c}_0 + \acute{c}_1 (2r_{i,\text{eff}})^{1} + \acute{c}_2 (2r_{i,\text{eff}})^{2} + \acute{c}_3 (2r_{i,\text{eff}})^{3}, \quad [4.52]$$

where $\acute{a}_y$, $\acute{b}_y$, and $\acute{c}_y$ for $y = 1,2,3$ are fitting constants derived by a Mie solution for different wavelengths and are given in Edwards et al. (2007).

To use Eq. 4.46 to 4.52 in GRAALS, means of the fitting constants have to be calculated for the eight spectral bands. Here, the mean constants calculated by Zubler et al.

(2011b) are used. Precipitating hydrometeors of snow, graupel, and rain are not considered in the radiation calculations, which may introduce a bias in the calculated radiation fields (Waliser et al., 2011).

5. Regional Scale Effects of the Aerosol-Cloud-Precipitation Interaction

The new extended model version of COSMO-ART enables, for the first time, the investigation of feedback processes between natural and anthropogenic emissions, gas phase chemistry, aerosol dynamics, cloud processes, radiation, and the state of the atmosphere together in a three-dimensional numerical simulation on the regional scale. Two different case studies were carried out to investigate different aspects of the aerosol-cloud interaction.

The first study focuses on the impact of anthropogenic aerosol acting as CCN on clouds and their properties and the impact of clouds on the aerosol distribution. The impact of orographic structures on the aerosol-cloud interaction is highlighted and the susceptibility of precipitation to aerosol variations is investigated for Europe. The content of this chapter is published in Bangert et al. (2011).

With the extended model version of COSMO-ART, the chain from emission of gases, gas phase chemistry, nucleation of particles, activation of the particles, up to clouds and precipitation on the regional scale can be simulated. Due to this online coupling of gases, aerosol and clouds, different feedback mechanisms can be considered in the simulations. Clouds modify the radiation in the atmosphere strongly, which has an impact on photochemistry and dynamics and therefore on the distribution of aerosol particles. This modifies the number of available CCN and therefore has an impact on the size distribution of the cloud droplets. As a result, the autoconversion of droplets to rain can be altered, which can cause a change in precipitation and by release or absorption of latent heat in different layers, the dynamics can be influenced. The change in precipitation consequently alters the aerosol distribution by washout of particles. The change in dynamics can also change the emissions of sea salt, which can cause a strong change in the number of available CCN especially in clean marine air.

This study addresses the following questions:

1. Are there systematic patterns in the distributions of aerosol number and mass concentration as well as cloud droplet number concentration? Are there close links between them?

2. Is there a relation between CCN, terrain slope, and cloud droplet number concentrations?

3. How are precipitation patterns altered when the interaction of aerosol particles and warm cloud processes are taken into account?

5.1. Simulation Setup

This study focuses on the interaction of aerosol acting as CCN with the liquid cloud phase. Table 5.1 shows the model setup for the representation of the aerosol-cloud interaction. The hybrid moment cloud scheme of Bangert (2008) is used to simulate the impact of CCN on cloud microphysics. The activation of the particles is calculated with the parameterization of Abdul-Razzak and Ghan (2000). The ice nucleation is independent of the simulated aerosol particles. As a result, all feedbacks are caused by aerosol acting as CCN.

A horizontal grid size of 0.125° (∼14 km) in both horizontal directions and 40 vertical levels up to a height of 20 km were used. The meteorological initial and boundary conditions are taken from the IFS model analyses of ECMWF. For the gaseous compounds and the aerosol particles, clean air conditions are prescribed. The analyses are used to update the meteorological boundary conditions every six hours. At the lateral boundaries a buffer zone is applied for all variables, according to the standard procedure of the COSMO model.

The simulation domain covers large parts of Europe and the Mediterranean (Fig. 5.2a). The simulation period is 16–20 August 2005. The domain and period are identical to the high cloud cover case in Vogel et al. (2009) in which the direct radiation feedback of the aerosol particles has been investigated and a comprehensive comparison of the simulated aerosol distributions with COSMO-ART to observations has been carried out.

Until 18 August the domain is mainly influenced by a high pressure ridge over Europe. During the following days a high level trough approached Europe and caused a cyclogenesis over the Benelux (Fig. 5.1). This yielded cloudy conditions, precipitation, and

Tab. 5.1.: Model setup used for the representation of the aerosol-cloud interactions.

cloud microphysics	sub-grid updrafts	aerosol activation	ice nucleation	cloud optical properties
hybrid-moment scheme of Bangert (2008) with prognostic N_c	effective updraft based on TKE	parameterization of Abdul-Razzak and Ghan (2000)	standard COSMO, independent of aerosol	standard COSMO, independent of aerosol
Sect. 3.4	Eq. 4.35	Sect. 4.1.3	Sect. 3.4	Sect. 3.3

westerly winds for large parts of Europe. During the last two days of the period a frontal system passed France and Germany. This caused an enhanced development of clouds in the frontal area and a change in air mass from warm continental to cool maritime air.

Two simulations were performed. In simulation A the whole period from 16–20 August 2005 was simulated including the interaction of aerosol particles with liquid cloud microphysics. The direct radiation feedback of the aerosol particles with the radiation was switched off to focus on the aerosol-cloud interaction. The first day was used to spin up the model and build up the aerosol concentration. For the analysis of the distribution of CCN and of the cloud properties the 18–20 August period was used. Simulation B was performed to quantify the impact of changes in aerosol concentration on cloud properties and precipitation. This simulation covers only the last two days of the period, where most of the precipitation occurred. The initial values for simulation B were taken from simulation A at 19 August, 00:00 UTC. In contrast to simulation A, a fixed aerosol concentration was prescribed in simulation B for the whole simulation domain (Table 5.2).

The prescribed aerosol concentration is identical to the conditions at a single grid point in South-West Germany at 19 August, 09:00 UTC, which represents approximately the average aerosol conditions during the simulation period. These values were kept constant and were used at all grid points in simulation B. The corresponding CCN spectrum of the prescribed aerosol concentration is shown in Fig. 5.2b.

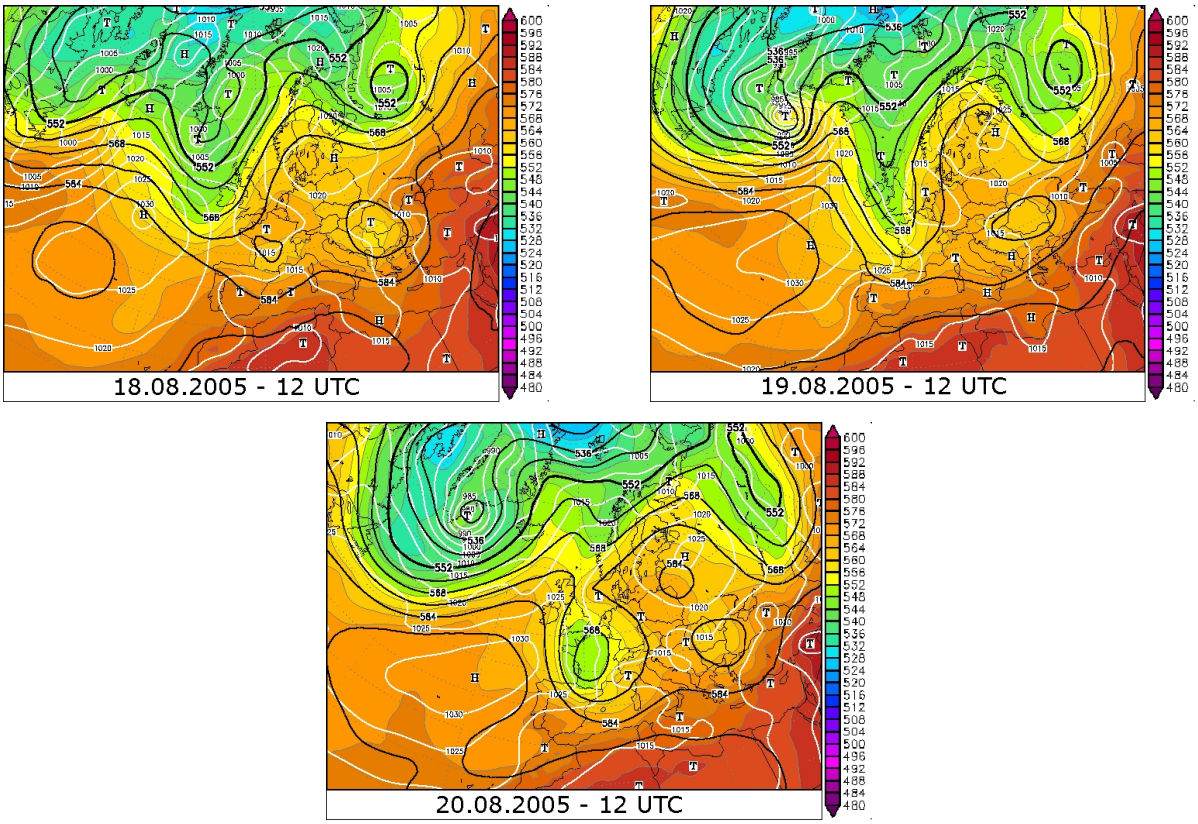

Fig. 5.1.: Synoptic situation represented by 500 hPa geopotential in gpdm (black contours), surface pressure in hPa (white contours), and relative topography in gpdm (colours) during the analysed period from 18. to 20. August 2005. Copyright www.wetter3.de period 18–20 August 2005.

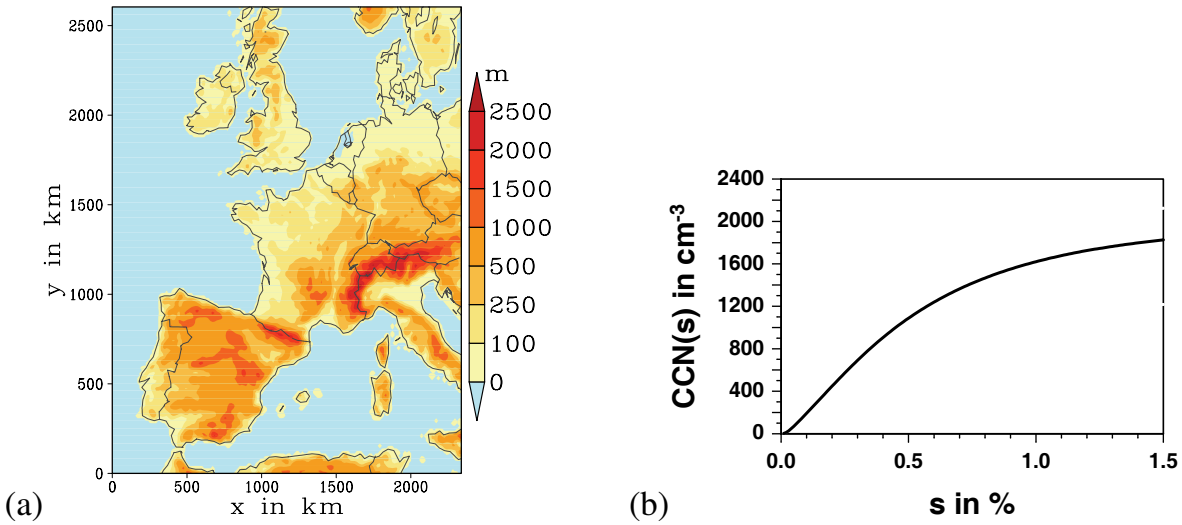

Fig. 5.2.: **(a)** Terrain height within the model domain, **(b)** CCN spectrum of the prescribed aerosol in simulation B.

Tab. 5.2.: Simulation description.

Abbreviation	Period	Aerosol	Initial Data
A	16–20 August 2005	Simulated, 8 Modes	ECMWF
B	19–20 August 2005	Constant, homogenous	Simulation A

5.2. Spatial Distribution of Aerosol and Cloud Droplets

Figure 5.3a shows the total number concentration of the simulated aerosol averaged over the period 18–20 August and over the height interval 0 to 1500 m. The highest number concentrations are found above Spain. Clean air is advected over areas with high emissions, which leads to the formation of new particles with small diameters. High particle number concentrations are also simulated above South-Germany. The corresponding distribution of the simulated CCN (0.1 %) number concentrations for simulation A are given in Fig. 5.3b. Above the Atlantic the CCN number concentrations are below $50\,\mathrm{cm}^{-3}$. It is evident that the spatial patterns of aerosol number concentrations and of CCN (0.1 %) are quite different. High CCN number concentrations on the order of $600\,\mathrm{cm}^{-3}$ are simulated in the southern part of Germany and in the northern part of the Po Valley. Comparing Fig. 5.3a and b shows that there is no obvious correlation between total aerosol number concentration and CCN (0.1 %) number concentration. The distributions of aerosol mass concentration and CCN (0.1 %) number concentration also showed no obvious correlation. For example, over the ocean total aerosol mass concentration can be very high due to large sea salt particles but the CCN (0.1 %) number concentration is very low. Calculations of the CCN concentrations for other supersaturations showed that the pattern of the CCN strongly depends on the supersaturation. This shows that the distribution of CCN strongly depends on the size distributions and the chemical compositions of the aerosol particles, which determine the shapes of the CCN spectra and, therefore, the distribution of CCN at different supersaturations.

Figure 5.3c shows the corresponding simulated cloud droplet concentrations N_c. The average N_c reaches its highest values, on the order of $400\,\mathrm{cm}^{-3}$, above France, Benelux, and Germany. Above the Atlantic N_c is below $50\,\mathrm{cm}^{-3}$. The pattern of N_c shows a very patchy distribution. The highest concentrations are found in the vicinity of mountainous

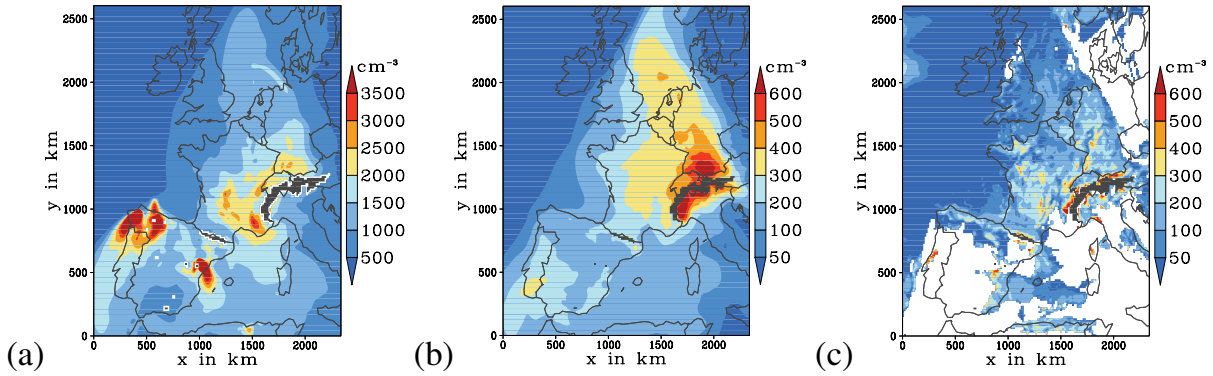

Fig. 5.3.: Simulated spatial distributions (Simulation A) of **(a)** average aerosol number concentration, **(b)** average CCN (0.1 %) number concentration, and **(c)** average N_c for the height interval 0 to 1500 m a.s.l. and the time period 18–20 August 2005.

regions. This indicates a possible correlation between orografic features and the average N_c, which is investigated in more detail.

5.3. Correlation of Terrain Slope and Cloud Droplet Number

The number of droplets inside a cloud depends on a variety of processes. On the one hand, the vertical velocity and the aerosol population determine the number of activated particles and, therefore, the initial value of N_c. On the other hand the microphysical processes inside the cloud change the cloud droplet spectra during the development of the cloud in time. With regional scale simulations it is possible to consider the complex topography which has local and systematic impact on the state of the atmosphere and therefore on, for instance, the vertical wind field. The simulation results indicate that there is a relation between terrain slope, CCN, and N_c. This is checked in the following by quantifying the terrain slope TS at a certain grid point with a very basic approach:

$$TS(i,j) = \frac{1}{4\Delta x}(|h(i,j)-h(i-1,j)|+|h(i,j)-h(i+1,j)| + |h(i,j)-h(i,j-1)|+|h(i,j)-h(i,j+1)|) \quad [5.1]$$

in which $h(i,j)$ is the terrain height at the grid-point (i,j) and Δx is the horizontal grid size.

The dependency of average N_c on CCN (0.1 %) and TS are given in Fig. 5.4a. The figure shows that the highest values of N_c are found in areas where the terrain slope is high.

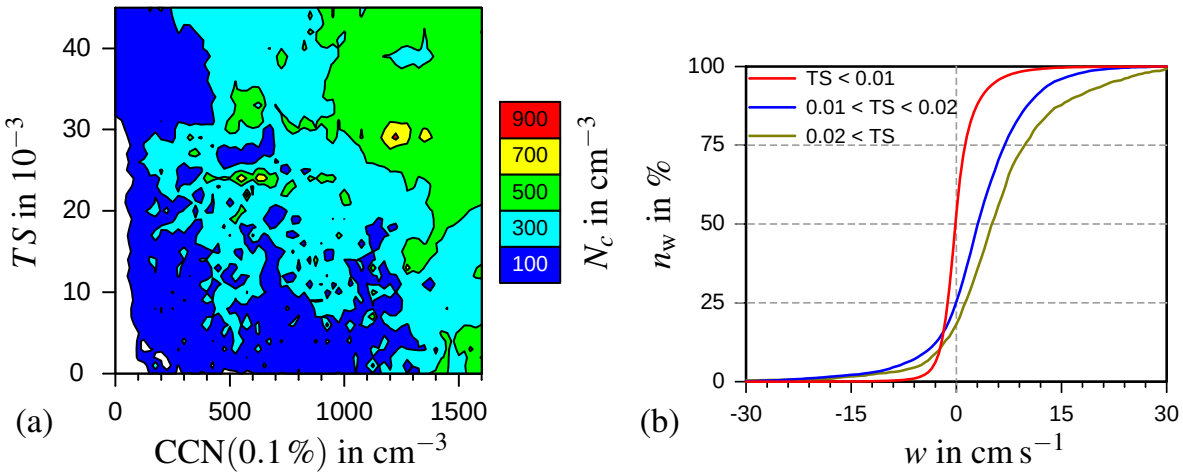

Fig. 5.4.: **(a)** Dependence of N_c on terrain slope parameter TS and CCN (0.1 %) concentration for 18–20 August 2005 and **(b)** cumulative percentage contribution n_w of the grid-scale in-cloud vertical velocity for different values of TS for 18–20 August 2005. N_c and CCN concentrations as well as the in-cloud vertical velocity are vertical averages for 0 to 1500 m a.s.l. (Simulation A).

Complex topography is able to modify the vertical wind field in the atmosphere. With the performed regional scale simulations the mesoscale impact of the terrain slope on the vertical wind velocities is resolved. The distribution functions n_w of the simulated vertically averaged grid-scale vertical velocities inside the clouds are shown in Fig. 5.4b. When TS is increasing, the mean grid-scale vertical velocity within the clouds is increasing.

In flat areas with TS lower than 0.01, the negative and the positive vertical velocities occur with equal frequency. 75 % of the vertical velocities within the clouds are greater than zero, when TS is larger than 0.01. This implies that in mountainous areas clouds are on average mainly in a development stage in which new particles can get activated. This explains the average higher values of N_c in the mountainous areas. Reutter et al. (2009) defined aerosol- and updraft-limited regimes of cloud droplet formation by using a one-dimensional cloud parcel model. They found that for a high ratio of updraft velocity and aerosol number concentration N_c is very sensitive to changes in aerosol number concentration, where for low ratios N_c is relatively insensitive to changes in the aerosol number concentration. According to the three-dimensional simulations results in this study similar regimes can be distinguished in terms of average N_c, CCN, and TS (Fig. 5.4a). In mountainous areas N_c strongly depends on the CCN, whereas in flat areas the average

N_c is less sensitive to changes in CCN. This can be explained by the dependency of aerosol activation on updraft velocity and aerosol number and is in conformance with the findings of Reutter et al. (2009).

To simulate the interaction of aerosol particles with clouds in modern global climate models, the subgrid-scale vertical velocities are crucial for the calculation of aerosol activation. Due to the coarse spatial resolution, the updrafts during cloud development are not resolved. Therefore, parameterizations have to be used. Many climate models integrate the activation parameterization for a given probability density function (PDF) of the vertical velocity to calculate the aerosol activation in one grid box. For this approach, the PDF of the subgrid-scale vertical velocity must be known. A common approach is to use the grid-scale vertical velocity as the center of the PDF and to determine the width corresponding to the turbulence e.g., the vertical eddy diffusivity or the turbulent kinetic energy (e.g. Storelvmo et al., 2006).

The presented results indicate that a parameterization of the PDF of subgrid-scale vertical velocities in climate models also should take the effect of subgrid-scale terrain slope (TS) into account. A first pragmatic approach is to determine the center of the PDF w_{PDF} as a linear function of the grid averaged subgrid-scale TS, $\overline{TS}$,

$$w_{\mathrm{PDF}} = \kappa \cdot \overline{TS}. \qquad [5.2]$$

Calculating the center of $n_{\mathrm{w}}(TS)$ (Fig. 5.4b) we get $\kappa \approx 2.8\,\mathrm{m\,s^{-1}}$. One should note that this is only a rough estimate. An improved formulation of the parameterization, based on a statistical analysis of model results that cover a period of several years with a high spatial resolution, will be presented in a future study. Such a parameterization results in more realistic cloud droplet numbers in mountainous regions. For climate models without the representation of aerosols, a pragmatic parameterization of N_c as a function of TS could be developed.

5.4. Aerosol Number Concentrations in the Vicinity of Clouds

In several measurement studies (Weigelt et al., 2009; Twohy et al., 2002; Keil and Wendisch, 2001; Hegg et al., 1990) high number concentrations of aerosol particles, respectively CCN, were found in the vicinity of clouds. Radke and Hobbs (1991) suggested that the vertical transport of precursor gases, the enhanced photolysis above the

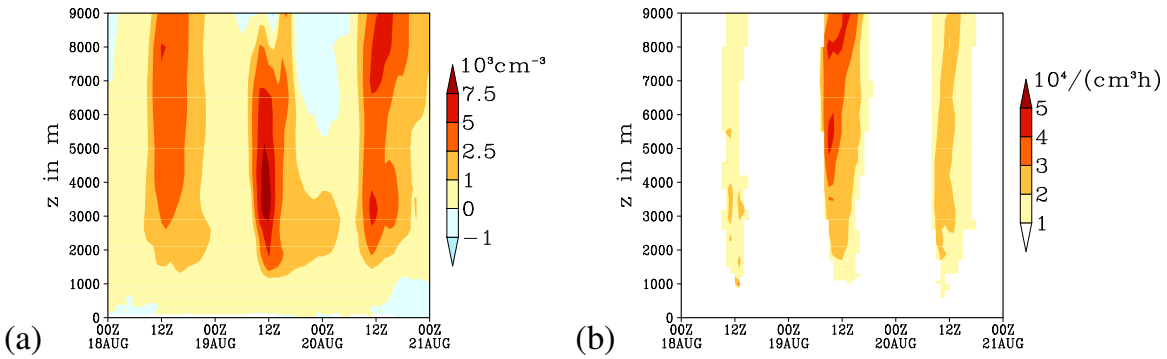

Fig. 5.5.: **(a)** Time evolution of the profile of the difference in the horizontally averaged total aerosol number concentration of cloudy to cloud free grid points, **(b)** time evolution of the profile of the horizontally averaged nucleation rate.

cloud and the high humidity in these regions can cause nucleation events and as a consequence high number concentrations of aerosol particles close to the clouds. With COSMO-ART this hypothesis can be checked, since all involved processes are considered and the potential impact of clouds on the nucleation of particles can be quantified. At first the major nucleation events that occur in the simulation are identified.

Figure 5.5a shows the time evolution of the profile of the horizontally averaged difference in the total aerosol number concentration of cloudy to cloud free grid points. The difference is mainly positive with high values in the free troposphere during midday. In Fig. 5.5b, the time evolution of the profile of horizontally averaged nucleation is shown. The criterion for a nucleation event is a change of more than 10^4 particles h^{-1} cm^{-3} in the smallest aerosol mode. In our simulations the nucleation of particles occurs in the late morning in the free troposphere. The nucleation is strongest at 19 August, with a maximum at an altitude of approximately 5000 m a.s.l. The occurrence of the nucleation events is consistent with the maximum differences in the total aerosol number. The higher aerosol number in the vicinity of clouds can therefore be explained by more effective nucleation close to the clouds. This supports the findings of the aforementioned studies.

Finally, this has an impact on the number of available CCN in areas where clouds develop. Figure 5.6 shows the time evolution of the profile of the ratio of horizontally averaged CCN (0.1 %) at grid cells containing cloud water and of horizontally averaged CCN (0.1 %) at cloud free grid cells. Below 1000 m a.s.l. the ratio is close to 1 and then increases monotonically up to a ratio of 10 in 5000 m a.s.l. This ratio is nearly constant

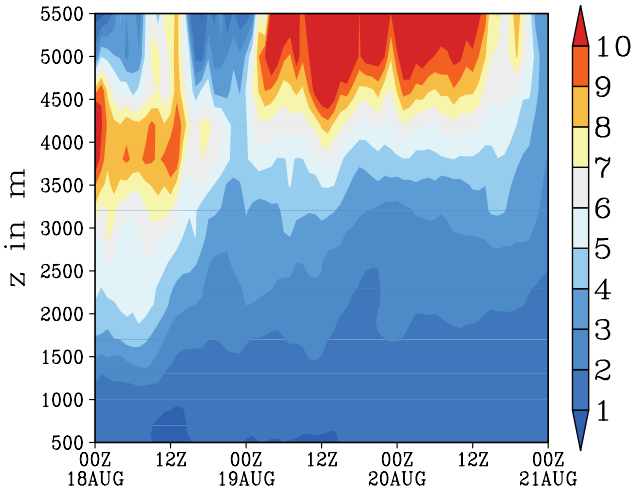

Fig. 5.6.: Time evolution of the profile of the ratio of horizontally averaged CCN (0.1 %) concentrations at grid cells containing cloud water and at cloud free grid cells.

during the passage of the front system from 19–20 August. In the free troposphere, the simulated number concentration of CCN (0.1 %) is much higher in areas where the clouds develop than in the cloud free surroundings.

Despite the fact that the enhanced nucleation plays a crucial role here, vertical transport of particles is also important. Flossmann (1998) showed that in a medium-sized convective cloud up to 70 % of the particulate mass can be transported into the free troposphere and can cause an accumulation of particles above the cloud.

5.5. Aerosols, Clouds, and Precipitation

The net impact of aerosol on clouds and precipitation can hardly be quantified in general because of the regime-dependent complex interactions (Stevens and Feingold, 2009). Besides the direct impact of aerosol on cloud microphysics due to changes in CCN number and therefore changes in droplet size, the dynamics and the atmospheric water cycle play an important role for the development of the clouds and the formation of precipitation (Sandu et al., 2008, 2009; Khain et al., 2008). Stevens and Feingold (2009) pointed out that interactions on different spatial and temporal scales can buffer the impact of aerosol changes to some extent. How efficient these buffering processes are is not yet known.

With the presented simulations of several days for a large model domain the direct microphysical response of the cloud to aerosol changes as well as the resulting macro-

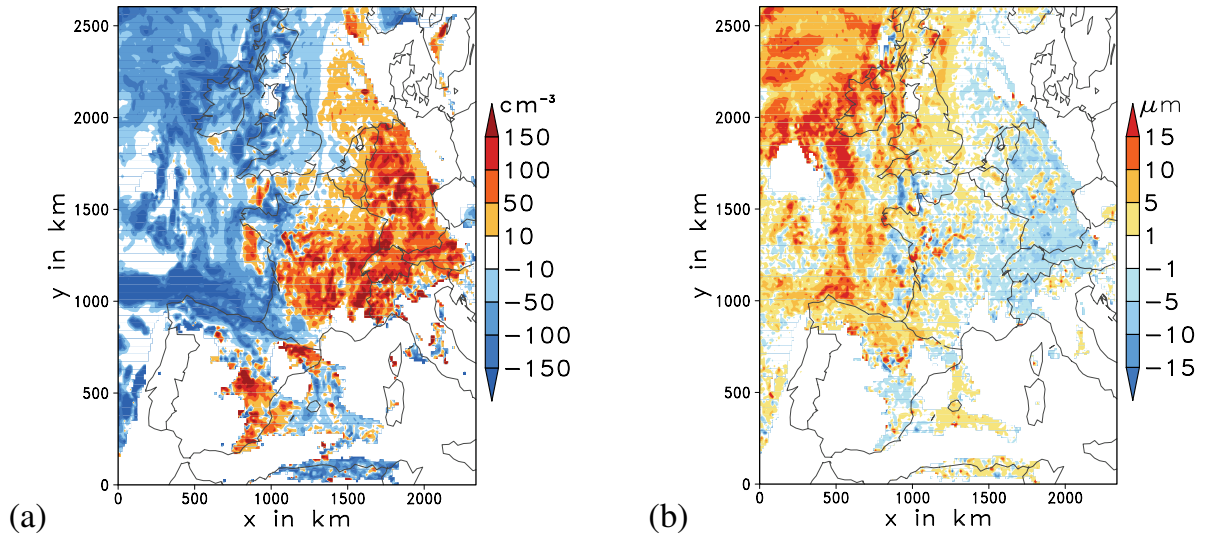

Fig. 5.7.: Difference in the **(a)** average N_c and **(b)** the average mean cloud droplet diameter between simulations A and B for 0 to 1500 m a.s.l. and 19–20 August 2005.

physical feedbacks on dynamics and on the water cycle can be resolved. Therefore, the net response of cloud properties and precipitation can be investigated and quantified.

Introducing a perturbation in regional-scale atmospheric simulations, due to new physical processes or artificially, will in general result in a perturbed precipitation distribution due to e.g., spatial shifts in the location of locally isolated cloud systems after several simulation days. For this reason the following analysis of the aerosol precipitation interaction focuses on a short simulation period of two days from 19–20 August 2005.

In Fig. 5.7a the difference of the mean N_c between simulation A and B are shown for the period of 19–20 August 2005. The simulated aerosol particles in simulation A cause lower N_c over the ocean and higher N_c over the continent and the Northern Sea compared to the prescribed aerosol in simulation B. The changes in mean N_c are directly related to the different availability of CCN in the two simulations.

The difference in N_c is reflected in the difference of the mean droplet size for most parts of the model domain, but there are also local regions, e.g. some parts over Western Germany, where the mean cloud droplet size is bigger despite the higher mean N_c (Fig. 5.7b). Dynamic feedbacks and, therefore, changes in the condensation overcome the initial impact of the aerosol on the microphysics in these areas.

Figure 5.8a shows the total accumulated precipitation of run A for the 19–20 August 2005. Over the Atlantic Ocean weak precipitation was produced by warm stratocumulus clouds. The precipitation amount did not exceed 5 mm in this area during this

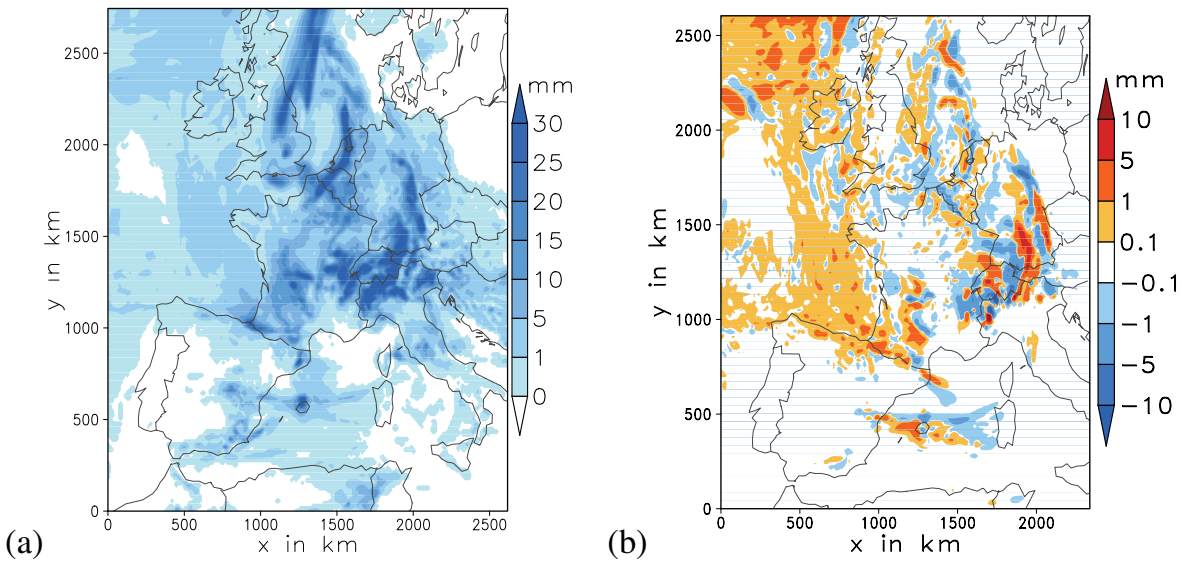

Fig. 5.8.: **(a)** Accumulated precipitation in simulation A for 19–20 August 2005, **(b)** difference of the accumulated precipitation amount between simulations A and B for 19–20 August 2005.

period. The highest precipitation amounts with values up to more than 30 mm occurred in the region of the Alps, the southern part of Germany, in France, and around the depression over the Northern Sea. The precipitation in these areas is produced mainly by mixed phase clouds.

The difference of the total accumulated grid-scale precipitation of A and B are depicted in Fig. 5.8b. Over the ocean the lower CCN number and, consequently, the bigger mean cloud droplet size caused an increase of the precipitation amount in the order of a few millimeter for the whole area. This is directly related to the more efficient formation of warm precipitation in the shallow stratiform clouds due to the lower CCN number concentration.

In case of the mixed phase cloud system, the impact of the aerosol changes on the precipitation is quite different. Whereas the location of the precipitation events is almost identical in both simulations, the total amount of the precipitation shows an alternation of increases and decreases. This is due to temporal and spatial shifts of the precipitation produced by the individual moving cloud systems.

In the areas with mixed phase clouds and higher precipitation amounts, the clouds have, on average, more condensate and higher updrafts inside the clouds in simulation A in which the CCN number is higher. Therefore, the impact on the precipitation can

be related mainly to dynamical effects, which can be initially caused by the changes in the aerosol concentration (Seifert and Beheng, 2006a). But previous and surrounding clouds can also affect the dynamics in several ways. Because of the complex non-linear interactions, the individual processes can hardly be separated.

For the quantification of the impact of the CCN on the precipitation, the precipitation susceptibility β can be used (Sorooshian et al., 2009). β is a measure of the response of the precipitation to changes in N_c or CCN. Here, β is calculated as a function of $\overline{\mathrm{CCN}(0.1\,\%)}$, which is an average between approximately 300 to 2000 m a.s.l., and the rain amount of the following hour $R_{1\,\mathrm{h}}$. Precipitation events with less than 0.01 mm precipitation per hour are neglected.

$$\beta = -\frac{\Delta \log(R_{1\,\mathrm{h}})}{\Delta \log(\overline{\mathrm{CCN}})} \qquad [5.3]$$

β is usually used for warm clouds, where positive values indicate their typical behaviour with more CCN cause less rain and negative values indicate more CCN cause more rain. Negative values of β can only be caused by additional processes and feedbacks besides the direct microphysical impact of the CCN number concentration on droplet number concentration and on the coagulation of cloud droplets, respectively. In this study β is applied for warm and mixed phase clouds. In contrast to other studies, which use one representative time during the development of a specific cloud, β is calculated for each hour and for the whole simulation domain and, therefore, covers different development stages of clouds. The advantage is that not only the first impact of the aerosol on the precipitation but also the ongoing feedbacks during the further cloud development are covered. Aerosol can, at first, change the precipitation in the early development of the cloud by modifying the autoconversion which will result in a positive β. This process can then cause a feedback with the ice phase of the cloud causing a negative β, and then afterwards, due to a change in condensate in the cloud, β can change its sign once again. A distribution of β, termed n_β, was calculated for the whole model domain and the last two days of the simulation period for about 110 000 grid points (Fig. 5.9). The peak of n_β is at a value of zero. The distribution shows that it is hard to estimate a mean value of β, for example for climate purposes, because both positive and negative β occur almost in the same amount. Moreover, what can be seen by this single simulation, which covers different cloud types and their development over several days, is that there is a slight

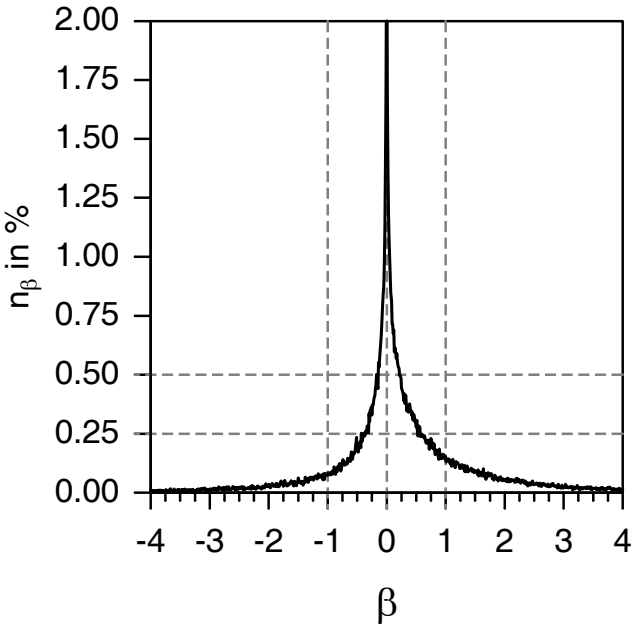

Fig. 5.9.: Simulated relative distribution n_β of β for intervals of $\Delta\beta = 0.01$ for 19–20 August 2005.

skewness of n_β to positive values of β. As a result the mean value for β is 0.23 for this simulation.

Sorooshian et al. (2009, 2010) separated different cloud regimes by correlating β and the cloud liquid water path LWP for cloud parcel and LES simulations and satellite measurements. They found that β increases with LWP till approximately 0.7–1 kg m^{-2} and then decreases again. In Fig. 5.10a, β is shown as a function of cloud water path for our simulation. The mean β increases with increasing cloud water path until 0.5 kg m^{-2} and then stays approximately constant at a value of 0.4.

To find the LWP for which the impact of CCN on the precipitation is most significant in our simulations independent of the sign of β, the absolute value $|\beta|$ of β for all points with an hourly precipitation amount greater than 0.2 mm was calculated. In Fig. 5.10b, $|\beta|$ is depicted as a function of cloud water path. It is increasing up to a value of 1 at $LWP = 0.85$ and then decreasing for larger LWP. This result is in agreement with the results found by Sorooshian et al. (2009, 2010).

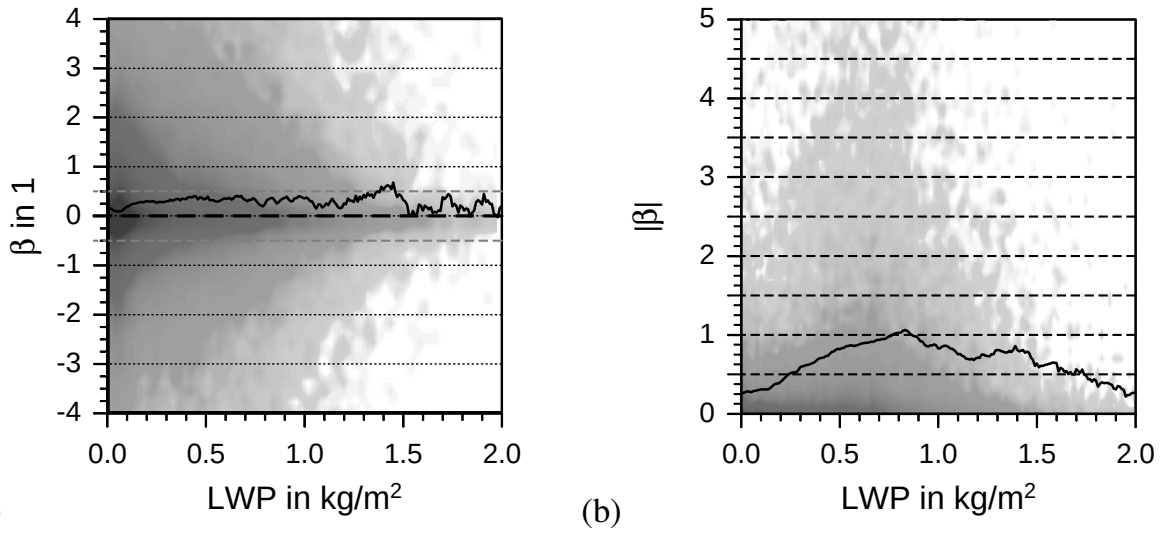

(a) (b)

Fig. 5.10.: **(a)** Simulated precipitation susceptibility β as a function of cloud liquid water path LWP for all grid points for 19–20 August 2005 and **(b)** $|\beta|$ for all grid points with more than 0.2 mm per hour for the same period. Shadings show the joint histogram for the available precipitation data. Dark colors indicate a high density of data points.

5.6. Conclusions

The model system was applied for Europe for a period in August 2005. The simulation of the CCN distribution showed that the treatment of aerosol size distribution and chemical composition is necessary in mesoscale studies with focus on the aerosol-cloud interaction and cannot be replaced by, for instance, correlations of CCN with either aerosol number or mass concentration.

It was shown that the mean N_c is dependent on the structure of the terrain. A terrain slope parameter TS was introduced to classify this dependency. The dependency of N_c on TS could be explained by the different PDF of in-cloud updrafts for different TS. This relationship can be used to parameterize the PDF of subgrid-scale cloud updraft velocity in climate models or directly for mean N_c for climate models in which no aerosol information is available.

The simulations showed big differences in aerosol number concentration at high altitudes during the late morning as well as a strong enhancement of CCN with increasing altitude in cloudy areas in comparison to cloud free areas. It was shown that the nucleation of secondary particles is strongly enhanced above the clouds. This is caused by a more effective photochemistry, humid conditions, and the strong vertical transport of

precursor gases in the cloudy areas. The simulations show that the distribution of CCN and clouds are strongly correlated with each other. Therefore, the treatment of complex photochemistry is crucial in atmospheric models to simulate the distribution of CCN.

The changes of cloud properties and precipitation for a prescribed aerosol distribution were investigated. The changes in the aerosol and the changes of N_c and mean droplet radii showed a clear correlation with more droplets and smaller radii in areas with more available CCN. For precipitation the changes showed different behaviours with a slightly enhanced precipitation in the maritime stratus because of less CCN and spatial and temporal shifts in the precipitation over the continent where mixed phase clouds are dominant. To quantify the impact of the aerosol on the precipitation, the precipitation susceptibility β was calculated for each time step and for the whole model domain. The distribution function of the susceptibility showed that both positive and negative values occur almost with equal frequency, but that the distribution has a slight skewness to positive values and a mean β of 0.23. In our simulations, clouds with a liquid water path of approximately $0.85\,\mathrm{kg\,m^{-2}}$ are most susceptible to aerosol changes with an absolute β of 1. The mean β for clouds with a liquid water path between $0.5\,\mathrm{kg\,m^{-2}}$ and $1\,\mathrm{kg\,m^{-2}}$ is approximately 0.4.

6. Impacts of Saharan Dust on Clouds, Radiation and Temperature over Europe

The second study focuses on a severe Saharan dust event over Europe in May 2008. With the new model framework the impact of dust on atmospheric state can be quantified, as it considers the competition of dust with other aerosol particles during droplet and ice formation and the feedback processes related to cloud microphysics, radiation, and precipitation. The sensitivity of predicted atmospheric state to the dust amount, properties (hygroscopicity), and parameterization is studied thoroughly. The content of this chapter is published in Bangert et al. (2012).

One of the major contributor to the atmospheric aerosol mass is mineral dust. Even though the emission sources of mineral dust are mainly desert regions, dust particles can be transported over long distances. Europe and the Mediterranean can be strongly affected by dust outbreaks originating in the Sahara Desert (Wiacek et al., 2010). This study addresses the following questions:

- Is there any significant effect of the aerosol-cloud interaction on the state of the atmosphere on short time scales, especially during extraordinary aerosol events like dust storms?

- How strong is the impact of Saharan dust events on the surface temperature and the state of the atmosphere over Europe? Are there consequences for operational weather forecast?

Beside their impact on clouds, dust particles modify the atmospheric radiation balance directly (Cavazos et al., 2009), which can cause a cooling or heating of the surface depending on several factors like the surface albedo and the elevation of the dust layer (Stanelle et al., 2010; Cavazos et al., 2009; Yin and Chen, 2007). Previous studies (Perez et al., 2006; Chaboureau et al., 2011) pointed out that including this direct interaction of mineral dust with radiation in model systems used for numerical weather prediction has

the potential to improve the quality of the forecast, especially in regions like Europe and the Mediterranean where the dust concentrations are dominated by sporadic Saharan dust events. As the impact of the aerosol-cloud interaction is assumed to be stronger than the direct impact on radiation (IPCC, 2007), the influence of these dust events can be even stronger.

Mineral dust particles are efficient IN (e.g. Field et al., 2006; Möhler et al., 2006). Since homogeneous freezing of deliquescent aerosol is very unlikely for temperatures higher than $-35\,^{\circ}\mathrm{C}$, the ice nucleation in the troposphere strongly depends on the heterogeneous freezing involving IN (Cantrell and Heymsfield, 2005). In an eleven year lidar-derived cloud data set, Seifert et al. (2010) found a 30 % higher amount of ice containing clouds over Europe with cloud top temperatures from -10 to $-20\,^{\circ}\mathrm{C}$ in air masses that contained Saharan dust. Analyzing satellite measurements from multiple platforms of a Saharan dust outbreak over the Atlantic in 2004, Min and Li (2010) showed that ice clouds tend to form at higher temperatures when dust particles are present. Global modelling studies demonstrated the important contribution of mineral dust to IN number concentration (e.g. Hoose et al., 2008; Lohmann and Diehl, 2006). The impact of mineral dust on the formation of cirrus clouds for temperatures lower than $-35\,^{\circ}\mathrm{C}$ depends on the competition of the heterogeneous freezing of mineral dust with the homogeneous freezing of liquid aerosol particles. For conditions with low updraft velocities, the heterogeneous freezing of dust particles is able to inhibit the homogeneous freezing and cause a decrease in ice crystal number concentration of the affected cirrus clouds (Barahona et al., 2010a).

Based on observations gathered by several satellites including TRMM, Terra and Aqua, and Meteosat-8 Min et al. (2009) showed that mineral dust significantly increases ice crystal number concentration and cloud droplet concentration with the consequence of a decreasing precipitation rate. Similar results were found by Rosenfeld et al. (2001) with a decrease in cloud droplet radius in clouds affected by dust and a suppression of light precipitation. In contrast, Pradelle and Cautenet (2002) found a decrease in cloud albedo in the presence of mineral dust because of an increase in cloud droplet radius. These conflicting results indicate that the impact of mineral dust on cloud droplet number depends on the individual atmospheric conditions, e.g. background aerosol and cloud type. A case study performed for the Eastern Mediterranean by Solomos et al. (2011) showed an increase in droplet number and in cloud top height with an increasing con-

centration of mineral dust particles, but also a strong dependency of the dust impact on precipitation on the prescribed aerosol background conditions.

The impact of dust on the cloud droplet concentration in most studies was hypothesized to be caused by hygroscopic coatings, which make them important CCN due to their large size. With the exception of dust from dry lake beds, freshly emitted dust contains little soluble material (Kumar et al., 2011). Processing of dust particles in clouds (Levin et al., 1996) and the condensation of acids on the particles (Sullivan et al., 2007) are prime mechanisms thought of creating hygroscopic coatings on dust. Kumar et al. (2011) however pointed out that dust particles do not require deliquescent material to act as CCN in the atmosphere, as the adsorption of water on the particle can induce hygroscopicity equivalent to having a considerable soluble fraction. In a global study, Karydis et al. (2011) pointed out that even uncoated mineral dust can contribute significantly to cloud droplet number close to the source regions and that hygroscopic coating of dust particles can decrease the cloud droplet number in regions which are affected by anthropogenic emissions due to a decrease in water supersaturation.

This study focuses on a major dust event that occurred in May 2008. Its origin was in the Sahara and from there mineral dust particles were transported over the Western Mediterranean, covering large areas of Western Europe.

During this episode, high aerosol concentrations were observed throughout Europe; ice nuclei concentrations significantly increased (compared to pre-event levels) at Kleiner Feldberg, Germany (Klein et al., 2010). During the dust event, traditional weather forecast models exhibited poor prediction skill. Here traditional means that operational weather forecast models so far neglect the dynamic behavior of atmospheric aerosol particles.

The German national meteorological service (Deutscher Wetterdienst, DWD) detected a significant bias in their numerical weather forecast of the 2-m temperatures, $T_{2\,\mathrm{m}}$, of $+1.5$ K when the dust outbreaks reached SW-Germany (Damrath, 2010, DWD, personal communication). A comparison of the predicted and observed $T_{2\,\mathrm{m}}$ is shown in Fig. 6.1. The differences are largest during the afternoon. In the early morning the temperatures converge again. The operational weather forecast at DWD is performed with the model system COSMO (Consortium for Small-scale Modeling) (Baldauf et al., 2011). Since the impact of aerosol particles on atmospheric state is accounted for in COSMO by using prescribed profiles for aerosol optical properties and prescribed cloud

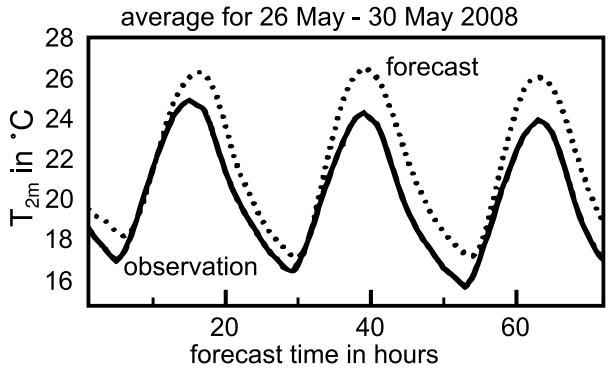

Fig. 6.1.: Predicted $T_{2\,\mathrm{m}}$ as a function of forecast hour compared with measurements for the area of SW-Germany (area Ω in Fig. 6.2). Each day a forecast for three days was simulated; afterwards the results and the corresponding observations were averaged as a function of forecast hour to identify systematic differences between forecast and observation (Damrath, 2010, DWD, personal communication).

droplet and ice crystal numbers, extraordinary aerosol conditions like the dust event in May 2008 are not represented in the simulations. This can potentially cause biases in the weather forecast.

6.1. Simulation Setup

This study focuses on the overall impact of dust particles on liquid as well as ice clouds and their optical properties. For this reason, the most comprehensive representation of the aerosol-cloud interaction in the model-framework is used including the adsorption activation of dust, homogeneous and heterogeneous freezing of aerosol particles, and two-moment cloud microphysics. An overview of the model setup used for the representation of the aerosol-cloud interactions is given in Table 6.1.

A nesting approach is used for the simulations. At first a simulation for a domain D0 covering Northwest Africa and Western Europe was performed. This domain enables the explicit simulation of the dust emissions over Africa and the long-range transport of the dust particles to Europe (Fig. 6.2). All gases and aerosol particles are simulated (Sect. 3.1), but are not allowed to interact with clouds and radiation. Calculations of the cloud microphysical processes are carried out with the one-moment cloud scheme, which includes cloud water, rain, cloud ice, snow, and graupel. The grid size is 0.25°

Tab. 6.1.: Model setup used for the representation of the aerosol-cloud interactions.

cloud microphysics	sub-grid updrafts	aerosol activation	ice nucleation	cloud optical properties
full two-moment scheme of Seifert and Beheng (2006b)	weighted means of N_c^* and N_i^* for a PDF of sub-grid scale updrafts	extended parameterization of Fountoukis and Nenes (2005) including FHH activation	homogeneous and heterogeneous freezing of aerosol particles	long- and shortwave optical properties as a function of $r_{c,\text{eff}}$ and $r_{i,\text{eff}}$
Sect. 4.5	Eq. 4.39	Sect. 4.1.3	Sect. 4.2	Sect. 4.6

(≈ 28 km) in both horizontal directions with 40 non-equidistant levels in the vertical up to an height of 20 km. Initial and boundary conditions for meteorological variables are obtained from the IFS ECMWF analysis; for gas-phase compounds, MOZART-4 results (Emmons et al., 2010) are used. Clean air conditions are assumed for the initial aerosol and for aerosol outside of the domain. The simulation starts at 22 May 2008, 00:00 UTC and ends 30 May 2008, 00:00 UTC.

For the analysis of the aerosol-cloud interaction three simulations were carried out on the nested grid for domain D1 (Fig. 6.2) covering regions affected by the dust event (France, Germany, and the Mediterranean). Cloud microphysical processes were simulated with the two-moment scheme (Sect. 4.5) and full interaction with the aerosol particles by activation, homogeneous freezing and heterogeneous freezing were allowed. The horizontal grid size is 0.0625° (≈ 7 km) in both directions with 40 non-equidistant levels in the vertical up to an height of 20 km and the simulated period is 22 May, 00:00 UTC till 30 May, 00:00 UTC. The boundary and initial conditions for all prognostic variables are taken from the simulation of the coarse grid for domain D0, which includes the concentration of dust transported from North Africa. The first four days (22 May till 25 May 2008) of the simulation are used to build up the aerosol concentration based on direct emissions and secondary formation. The analysis of the results focuses on the dust event

(26 May till 29 May 2008). The individual nested simulations differ in the setup used for the dust-atmosphere interaction.

In simulation REF the interaction of dust particles with clouds and radiation was not allowed. To investigate the impact of the dust particles due to their interaction with clouds we carried out simulation C which includes the impact of the dust particles on cloud formation via activation of dust particles and heterogeneous nucleation of cloud ice on the dust particles. In simulation C it is assumed that the dust particles have no hygroscopic coating. Therefore the FHH adsorption theory is used for the activation of the dust particles using $A_{\mathrm{FHH}} = 2.5$, and $B_{\mathrm{FHH}} = 1.2$ (Kumar et al., 2011). Aged dust particles can potentially have hygroscopic coatings which decreases the supersaturation needed for their activation. To quantify the impact of this effect, simulation C* is carried out, assuming that the dust particles are coated by 10 % (in volume) ammonium sulfate. In this case the activation of the dust particles is calculated with the unified approach of Kumar et al. (2011). In simulation CR, the direct interaction of the dust particles with long and shortwave radiation is considered additionally to their impact on cloud formation (with the conditions of simulation C). Table 6.2 gives an overview of the individual simulations and their abbreviations.

In all simulations a detailed data set for anthropogenic emissions, which includes traffic emissions, emissions by large point sources, and area sources such as households and industrial areas, is used. The emission data has an hourly resolution and includes the emission of SO_2, CO, NO_x, NH_3, 32 individual classes of VOC, and the direct emission of elemental carbon particles (Pregger et al., 2007).

6.2. The Saharan Dust Event

During 26 to 30 May 2008 Europe was affected by a strong Saharan dust event. A persistent trough reaching from Iceland to Morocco dominated the synoptic situation during these days. Due to steady southerly winds over the Mediterranean dust particles were transported efficiently from the emission sources in the Sahara to Central Europe. Figure 6.3 shows the measured and simulated aerosol mass concentration of particles with a diameter below 10 μm (PM_{10}) at Hohenpeissenberg, Germany (H. Flentje 2010, DWD, personal communication). Please note that the vertical axis is in $\log_{10}$-scale to take the large variation of PM_{10} during the dust event into account. The measurements

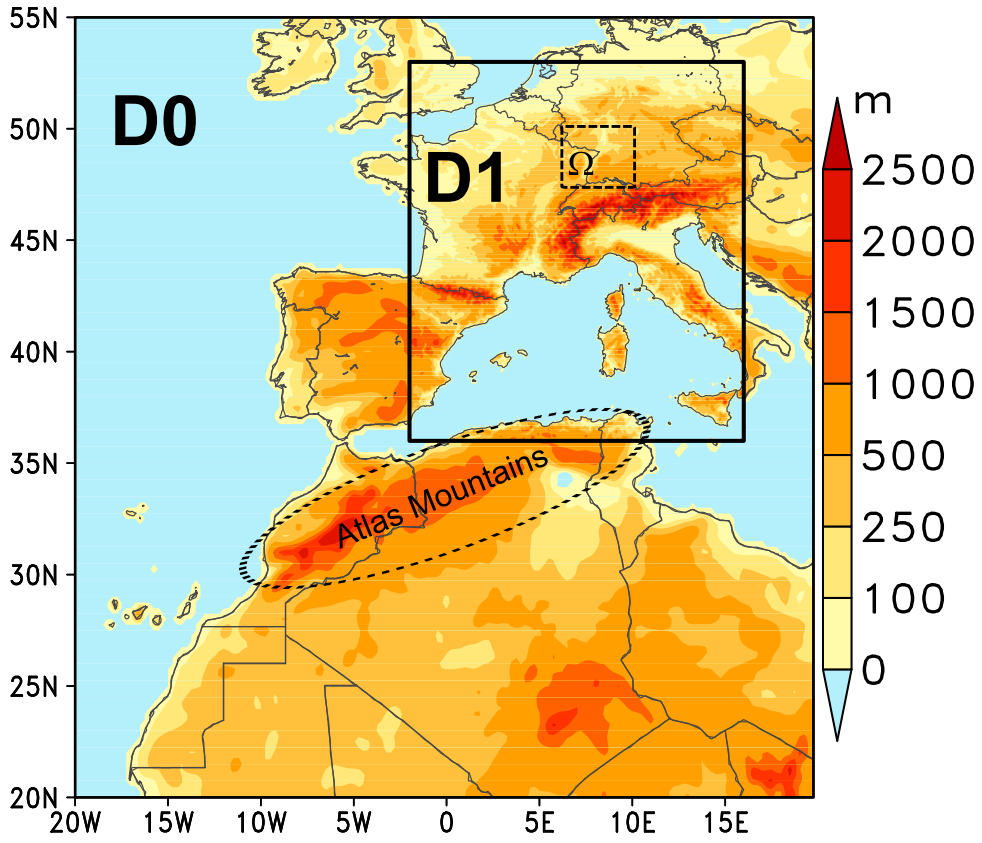

Fig. 6.2.: Terrain height within the model domains.

Tab. 6.2.: Overview of the setup for the nested simulations. The interaction involving aerosol include anthropogenic (if, ic, jf, jc, and s) and sea salt (sa, sb, and sc) modes, whereas dust refers to the dust modes (da, db, and dc) only.

Interactions	REF	R	C	C*	CR
Cloud–radiation	•	•	•	•	•
Aerosol–radiation	•	•	•	•	•
Aerosol–water clouds	•	•	•	•	•
Aerosol–ice clouds	•	•	•	•	•
Dust–water clouds (FFH theory)			•		•
Dust–water clouds (Unified theory)				•	
Dust–ice clouds			•	•	•
Dust–radiation		•			•

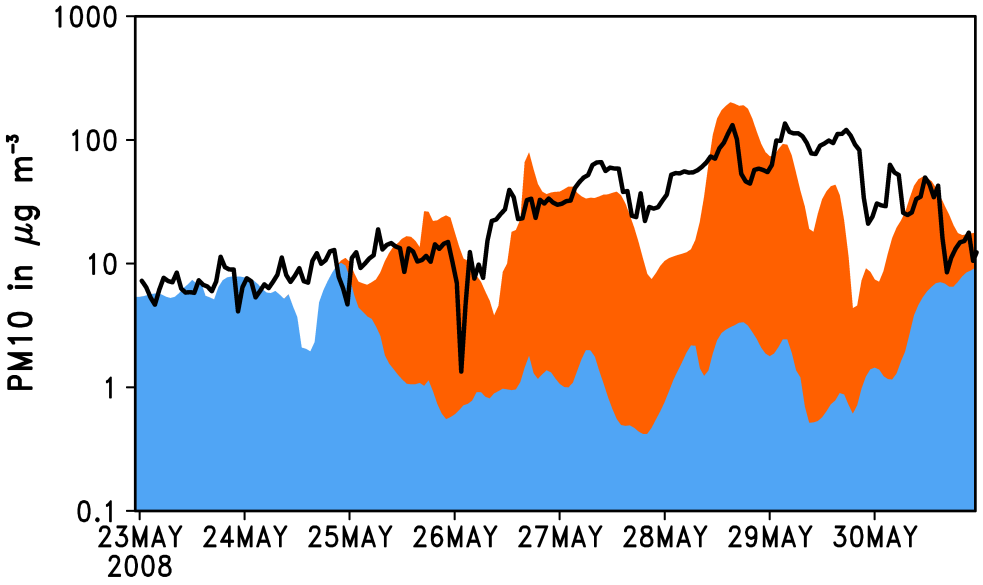

Fig. 6.3.: Measured aerosol mass concentration, PM_{10}, at Hohenpeissenberg (Flentje, 2010, DWD, personal communication) (solid line) and simulated PM_{10} (shadings) of the coarse simulation for domain D0. Total aerosol mass concentration of dust particles of mode da and db (orange shading), total aerosol mass concentration of all other modes including anthropogenic aerosol particles and sea salt (blue shading).

show a strong increase of the aerosol mass starting at 26 May and lasting till 30 May. The simulation attributes this to the arrival of mineral dust transported from the Sahara. The model reproduces the measured PM_{10} concentrations reasonably well during the dust event and captures the existing aerosol background before the arrival of the dust which is dominated by particles from anthropogenic sources. Upon the arrival of the dust, the simulated PM_{10} concentration of anthropogenic and biogenic particles decrease from $6\,\mu g\,m^{-3}$ to $1\,\mu g\,m^{-3}$ and increase again after the dust event. This indicates that the aerosol population during a Saharan dust event over Europe differs strongly from the simple assumption of adding additional dust particles to a typical (continental) aerosol population. Therefore aerosol particles have to be simulated explicitly on the basis of anthropogenic and natural emissions in studies, which address the interaction of dust events with the atmosphere.

A comparison of the distribution of simulated and measured PM_{10} concentrations (EEA, 2011) is shown in Figure 6.4 for the main days of the dust event. The distribution of the dust plume (characterized by PM_{10} concentrations higher than $20\,\mu g\,m^3$) is cap-

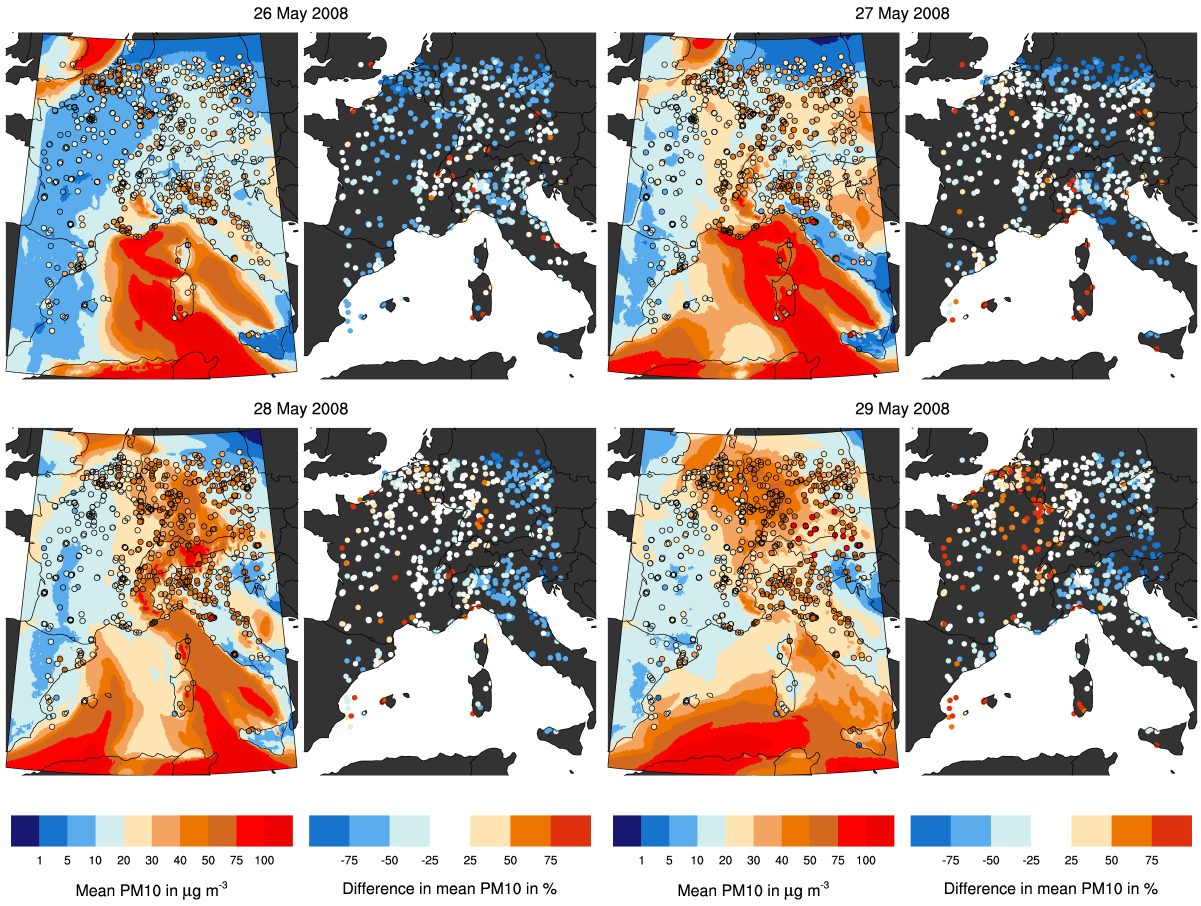

Fig. 6.4.: Simulated average PM_{10} concentrations in the lowest model layer (case CR) in comparison to AIRBASE surface PM10 measurements (EEA, 2011).

tured well in the simulations. A strong gradient in PM_{10} between France and Germany is found in both the simulation and the measurements. On the 29 May, the maximum of the dust plume is shifted slightly to the North West in the simulation in comparison to the observed distribution. In the northern part of of the model domain and in the Po Valley the simulated PM_{10} concentrations are systematically lower, which is most likely caused by uncertainties in the anthropogenic emission inventory and unresolved local effects.

At the Atlas mountains the transported dust particles were lifted to the upper troposphere. This ascending air flow on the one hand enabled the long range transport of the dust particles to Central Europe and on the other hand caused conditions favorable of heterogeneous and homogeneous ice cloud formation. Additionally, warm and mixed phase clouds were formed over the whole domain.

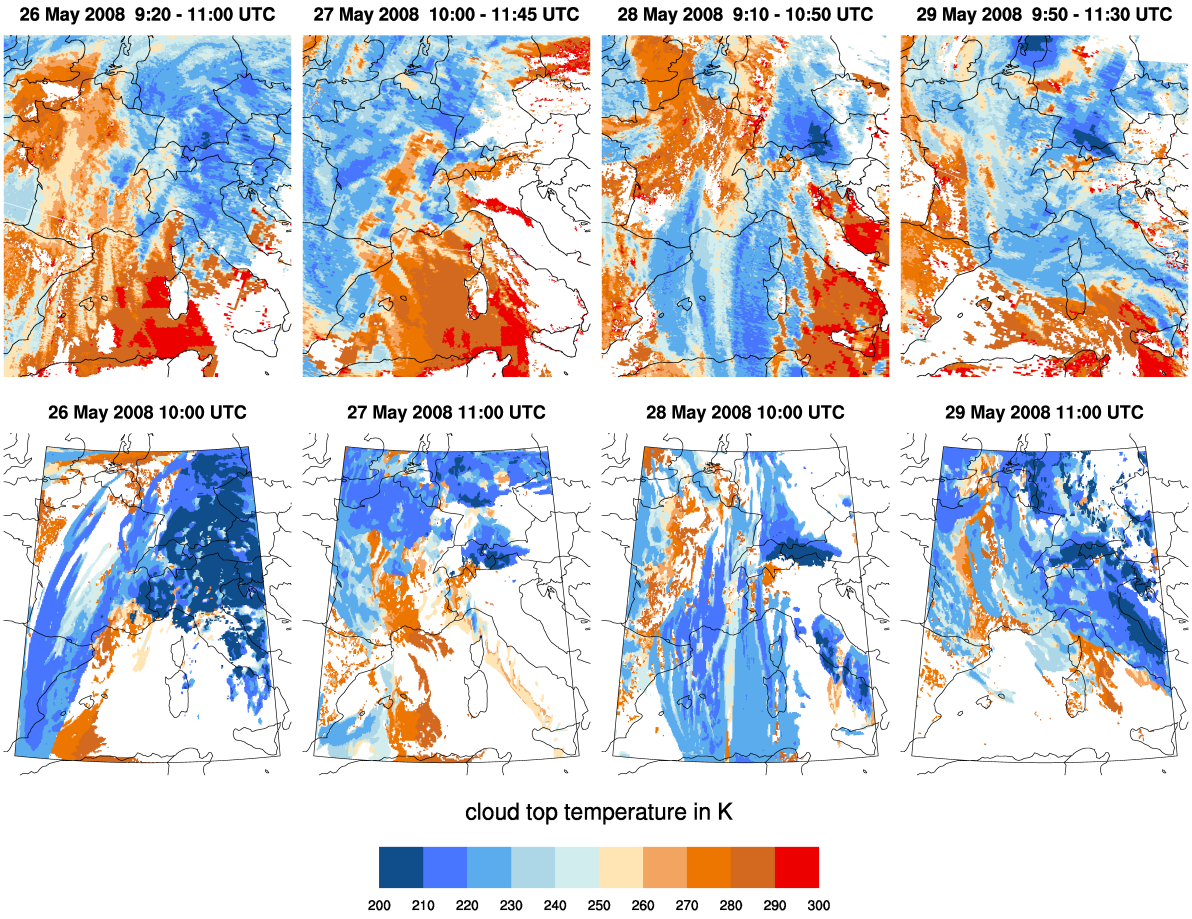

Fig. 6.5.: Composites of cloud top temperatures measured with MODIS (top) and simulated cloud top temperature (case C, bottom).

Figure 6.5 presents satellite retrievals of MODIS (Menzel et al., 2008) and calculated cloud top temperatures on basis of simulation C during the morning hours. The cloud top temperature at the individual grid points are calculated as the temperature of the highest model layer in which the grid scale cloud optical thickness exceeds 0.05. Even though both cloud top temperatures are derived in very different ways, a comparison allows to check if the main features of the observed cloud distribution are represented in the simulation. On the morning of the 26 May 2008 the high clouds in the eastern part of the model domain are well captured, whereas the high clouds in the South Western part are not found in the satellite data. On 27 May 2008, the north western part of the model domain is covered by high clouds which are reproduced by the simulation. The distribution of high clouds on 28 May 2008 shows an eye-catching pattern over the Mediterranean. The high clouds over Eastern France and North Italy on the 29

May 2008 are also reproduced by the simulation. The main differences on all days occur in warm low level clouds which are detected by the MODIS retrieval e.g. over the Mediterranean but are not reproduced by the simulations. This difference is partly due to a misinterpretation of the MODIS retrieval algorithm which classifies the optical thick dust layers over water as clouds (Frey, 2011, CIMSS/SSEC/UW-Madison, personal communication). Differences in the absolute value of cloud top temperatures at very low temperatures most likely arise from the coarse vertical resolution of the model at these heights.

The main dust plume affecting Europe originated in Algeria where steady moderate winds caused an effective emission of mineral dust into the atmosphere. Due to south easterly winds, the dust particles were transported to the North where they were lifted into the middle to upper troposphere at the Atlas Mountains.

Figure 6.6 presents the simulated daily mean dust number concentrations N_d for the nested model domain during the period of the dust event. N_d is calculated for three different temperature ranges, each of them favorable for a different process of aerosol cloud interaction. In the lowest layer, which reaches from the ground up to the freezing level, liquid clouds can form, with N_d being highest, up to more than $50\,\mathrm{cm}^{-3}$ inside the plume over the Mediterranean. From 27 May till 29 May 2008 wide areas of Eastern France and Western Germany were affected by dust concentrations above $25\,\mathrm{cm}^{-3}$.

In the middle layer, which reaches from the freezing level up to the level of homogeneous freezing ($T \approx 235\,\mathrm{K}$) and hence is favorable of heterogeneous freezing, dust number concentrations are in the order of 10 to $50\,\mathrm{cm}^{-3}$ with maxima over the eastern part of France.

The upper layer, which reaches from the level of homogeneous freezing up to 15 km height and hence is favorable of combined homogeneous and heterogeneous freezing, has mean dust concentrations in the order of $1\,\mathrm{cm}^{-3}$ over Europe.

6.3. Impact on Cloud Droplet and Ice Crystal Number Concentration

Owing to their size and surface properties dust particles can act as CCN. High dust concentrations can therefore modify the cloud droplet size distribution and consequently the microphysical processes in the warm cloud phase. Dust particles are found to be very efficient ice crystal nuclei in several lab and field studies (Field et al., 2006; Möhler et al.,

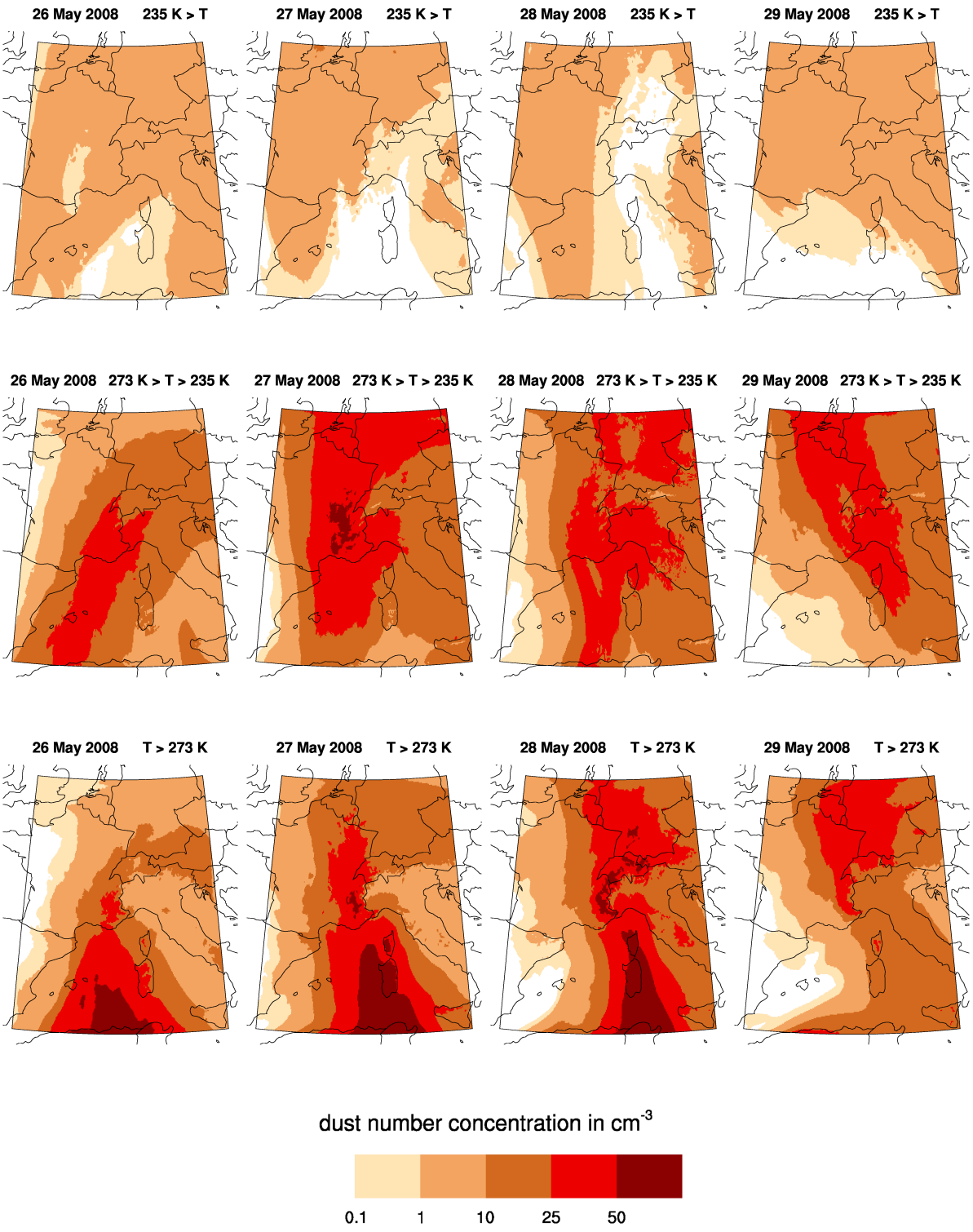

Fig. 6.6.: Simulated daily means of dust number concentrations for atmospheric layers below freezing level (bottom), layers favorable of heterogeneous freezing (middle), and layers favorable of homogeneous freezing (top) for 26–29 May 2008.

2006). Ice nucleation due to immersion freezing of dust particles starts at temperature around 263 K with a freezing fraction on the order of 0.1 %. At temperature around 253 K, the freezing fraction of dust particles was found to be in the order of 1 % (Phillips et al., 2008). At temperatures below 235 K ice crystal nucleation due to homogeneous freezing of aerosol droplets sets in. At this temperature range heterogeneous freezing of the dust particles has to compete with homogeneous freezing for water vapor.

In the following, joint histograms of cloud droplet and ice crystal number, N_c and N_i, and mass concentrations, m_c and m_i, are shown for different temperature ranges for simulation REF and C (Fig. 6.7, Fig. 6.10, and Fig. 6.11). The histograms are calculated for all grid points and the whole period of the dust event (26–29 May 2008). With the help of the joint histograms, systematic differences in the distribution of N_c, N_i, m_c, and m_i between the simulations can be identified together with difference in the overall number of grid points containing cloud water and ice crystals in the individual simulations.

For temperatures above freezing level, the domain-wide joint histograms of cloud droplets in simulation REF and C show small differences (Fig. 6.7). This is because the overall number concentration of available CCN is dominated by sea salt and secondary aerosol particles. The number concentrations of activated dust particles, N_d^*, is mostly below 3 cm^{-3} and higher number concentrations up to 20 cm^{-3} occurred only for total activated number concentrations, N_a^*, below 200 cm^{-3}. The fraction of N_d^* to N_a^* is mostly below 10 %.

Despite the fact that the coated dust particles can be activated at lower supersaturations than the uncoated particles, the domain wide joint histogram of cloud droplets in simulation C* shows only slightly higher N_c in comparison with simulation C (Fig. 6.7). One reason is that even though much more dust particles get activated in simulation C* in comparison to simulation C the number is still low in comparison to the total number of activated particles for most of the grid points (Fig. 6.8). Nevertheless, there are more cloudy grid points in simulation C* where N_d^* contributes to 10 % or more of N_a^* at values of N_a^* below 200 cm^{-3}. Hence the dust particles can have a significant impact on individual clouds for conditions with low number concentrations of other aerosol particles. Another reason for the low impact of coated dust particles on N_c is that the increased number of activated dust particles causes lower maximum supersaturations, s_{max}, due to the growth of the dust particles. This lower supersaturation can result in a decrease

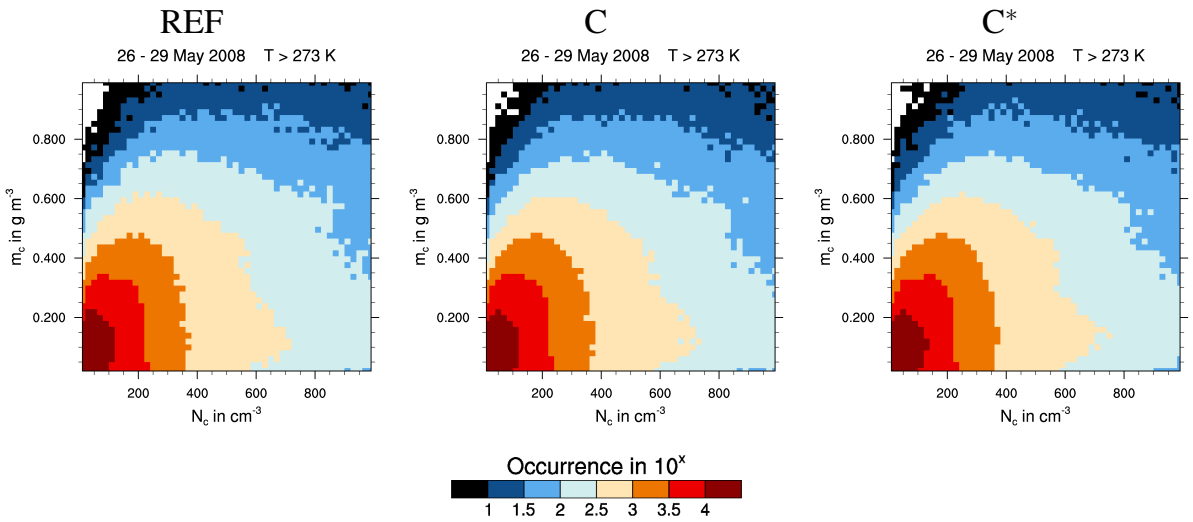

Fig. 6.7.: Domain wide joint histogram of number and mass concentrations for cloud droplets calculated for grid points with $N_\mathrm{d} \geq 1\,\mathrm{cm}^{-3}$ and temperatures above 273 K for 26–29 May 2008 for simulation REF, C and C*.

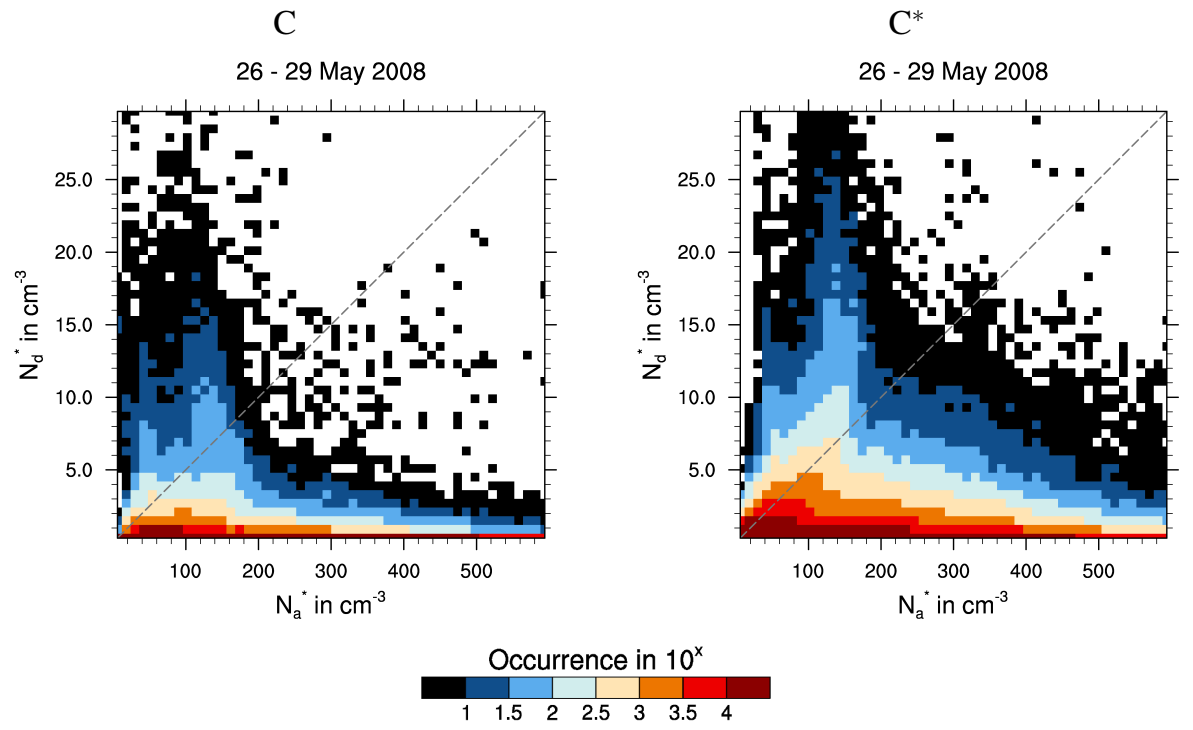

Fig. 6.8.: Domain wide joint histogram of activated dust particles, N_d^*, and total number of activated aerosol particles, N_a^*, calculated for grid points with $N_\mathrm{d} \geq 1\,\mathrm{cm}^{-3}$ for 26–29 May 2008 for simulation C and C*.

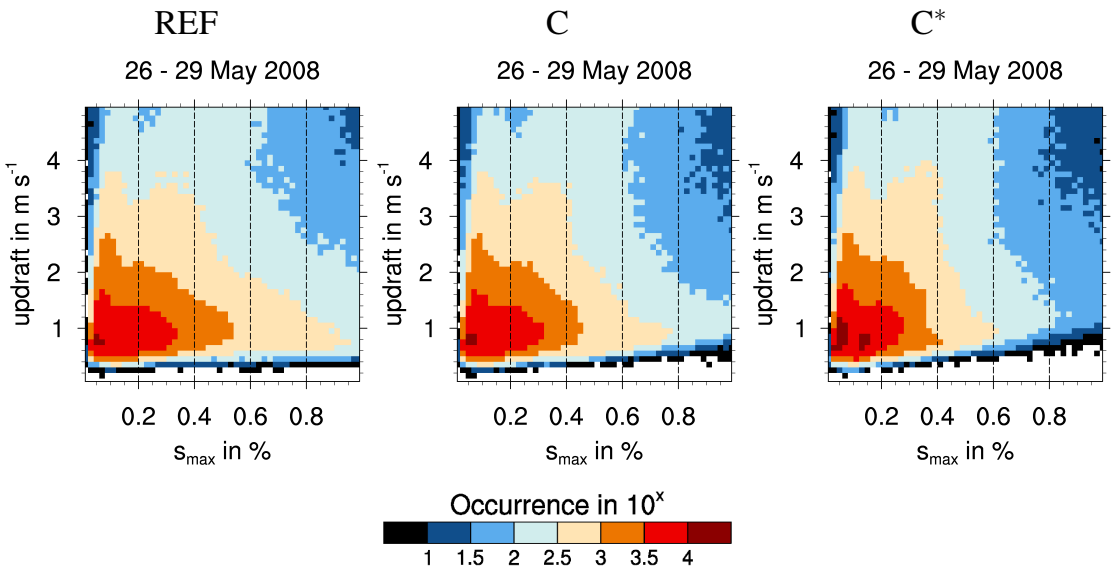

Fig. 6.9.: Joint histogram of updraft and maximum supersaturation, $s_{\max}$, during activation of particles calculated for grid points with $N_d \geq 20\,\mathrm{cm}^{-3}$ for simulation REF, C, and C*. The updraft is calculated as $w + \sqrt{TKE}$. $s_{\max}$ is the average of the corresponding updraft PDF (see Eq. (4.39)).

of the activated droplets from aerosols other than dust. This can buffer the impact of the increased number of activated dust particles on N_c (Kumar et al., 2009) and can be another reason of why total droplet number does not increase significantly in simulation C*. In Fig. 6.9 the joint histogram of the maximum supersaturation and the updraft during the activation process are shown for the cases REF, C, and C*. The impact on $s_{\max}$ is strongest in case C*, with significantly lower $s_{\max}$ in comparison to case REF. For uncoated dust particles (case C) the impact on $s_{\max}$ is lower, because of the small amounts of water required for FHH activation (Kumar et al., 2009), in comparison to the Köhler activation of hygroscopic particles.

The impact of the dust particles on number and mass concentration of cloud droplets and ice crystals for atmospheric layers with temperatures in the range of 273 to 235 K is dominated by the heterogeneous nucleation of ice crystals from dust particles. The joint histogram of number concentrations of ice crystals, N_i, and mass concentrations of ice crystals, m_i, show a systematic increase in N_i of $30\,\mathrm{L}^{-1}$ which corresponds to an increase of N_i in the order of 100 % (Fig. 6.10). An increase of N_i in the order $30\,\mathrm{L}^{-1}$ corresponds to roughly 1 % of N_d which nucleate to ice crystals in the considered temperature range.

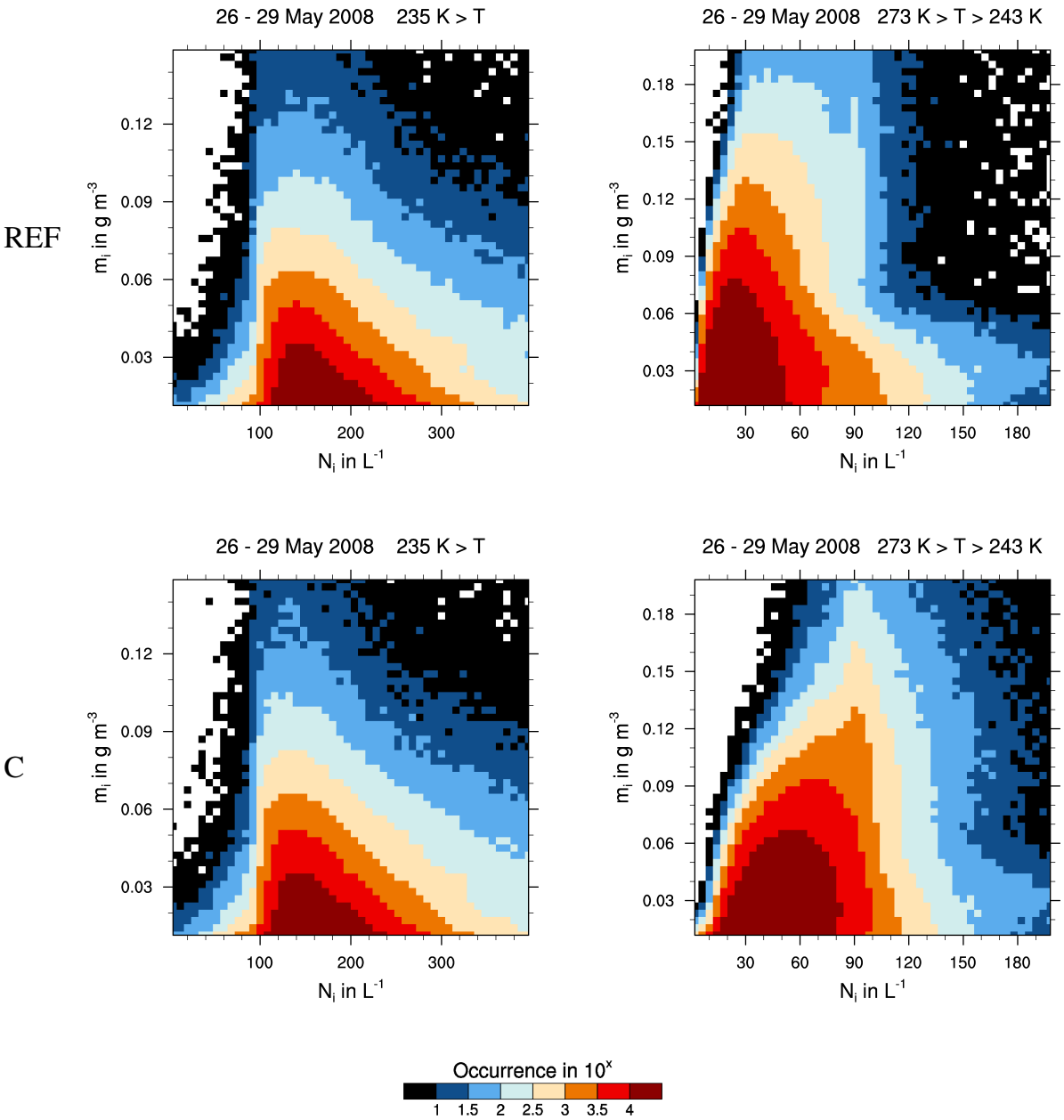

Fig. 6.10.: Domain wide joint histogram of number and mass concentrations for ice crystals calculated for grid points with $N_d \geq 1\,\mathrm{cm}^{-3}$ and two temperatures ranges above and below 235 K for 26–29 May 2008. The top row shows results from simulation REF. The bottom row shows results from simulations C.

Additionally, the distribution of N_i is broadening from a narrow distribution of N_i in case REF centered at low N_i in the order of $15\,L^{-1}$ to a wide distribution centered at N_i in the order of $60\,L^{-1}$. This can be explained by the more variable distribution of N_d in comparison to the distribution of soot particle IN in case REF.

The more efficient ice nucleation in the temperature range between 273 to 235 K from heterogeneous freezing of the dust particles has an impact on the glaciation of mixed phase clouds. Though the freezing of cloud droplets in the realized simulations is independent of the simulated aerosol particles, the enhanced ice nucleation involving the dust particles is able to modify the cloud droplet distribution for temperature below 263 K (Fig. 6.11). The total number of grid points with $m_c > 0$ is significantly reduced in case C with respect to case REF. In particular, grid points with low m_c and N_c are strongly decreased in number. This is due to the Bergeron-Findeisen process, where ice crystals grow at the expense of the existing water droplets due to the difference in saturation ratio with respect to water and ice. The total number of grid points containing cloud water decreased by 61 % in simulation C with respect to simulation REF in the temperature range between 263 to 235 K.

For atmospheric layers above the level of homogeneous freezing ($T < 235\,K$), the joint histograms of m_i and N_i are very similar in both simulations (Fig. 6.10). At this temperature, the heterogeneous freezing of the dust particles has to compete with the homogeneous freezing of the aerosol droplets for water vapor during the ice nucleation. An increasing number of heterogeneous freezing particles, N_{het}, will at first decrease the maximum ice supersaturation during the nucleation event and therefore decrease the total number of nucleated ice crystals because homogeneous freezing is less effective. The value for which N_{het} completely inhibits homogeneous freezing is defined as N_{lim} (Sect. 4.2). For N_{het} greater than N_{lim}, heterogeneous freezing is the only contributor to ice crystal number concentration and will increase with increasing N_d (Barahona and Nenes, 2009a).

In Fig. 6.12 the joint histogram of N_{het} and N_{lim} is shown for simulation REF and C. In the former, N_{het} is mostly lower than $10\,L^{-1}$ with only few grid points where N_{het} exeeds N_{lim} for conditions with N_{lim} lower than $60\,L^{-1}$. In the latter simulation, N_{het} is generally much higher due to the heterogeneous freezing of the dust particles, but rarely exceeds $100\,L^{-1}$. Therefore N_{het} is mostly below N_{lim} and is not able to significantly

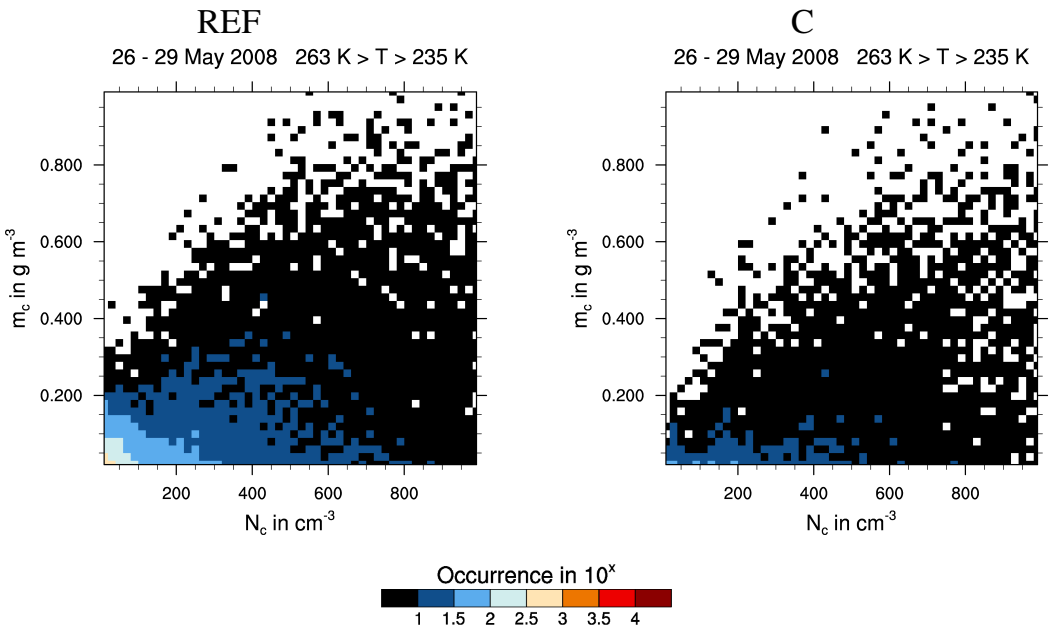

Fig. 6.11.: Domain wide joint histogram of number and mass concentrations for cloud droplets calculated for grid points with $N_\mathrm{d} \geq 1\,\mathrm{cm}^{-3}$ and temperatures between 263 K and 235 K for 26–29 May 2008 and simulation REF and C.

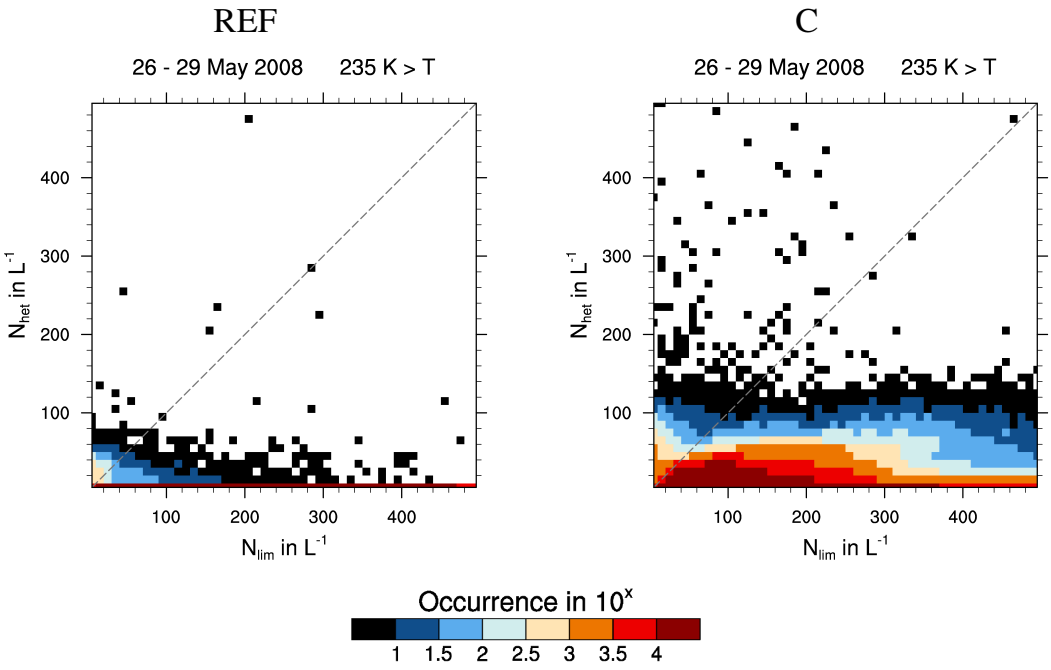

Fig. 6.12.: Joint histogram of heterogeneously nucleated ice crystals and N_lim, calculated for grid points with $N_\mathrm{d} \geq 0.1\,\mathrm{cm}^{-3}$. The dashed line highlights the limit between combined heterogeneous-homogeneous freezing (below the line) and pure heterogeneous freezing only (above the line).

impact N_i. For relatively few conditions (with N_{lim} lower than $100\,L^{-1}$) N_{het} is able to exceed N_{lim}.

6.4. Impact on Cloud Properties and Radiation

The previous section focused on the net impact of the dust particles on cloud droplet and ice crystal number concentration for the whole model domain during the simulation period. Systematically higher values in ice crystal number concentration were found for atmospheric layers between freezing level and the level of homogeneous freezing in case C in comparison to case REF. This has numerous consequences on cloud properties. For instance, the more effective glaciation of mixed phase clouds in simulation C, which has potential consequences on the vertical distribution of the latent heat release and the dynamic development of the clouds. The higher number concentrations in N_i (but similar values for m_i) in both simulations causes difference in the size of the ice crystals and therefore has consequences on the sedimentation velocity of the ice crystals and on the optical properties of the ice clouds. Shortwave radiation is scattered more efficiently by smaller ice crystals, which results in optically thicker clouds. In Fig. 6.13 the difference in the net surface shortwave radiation flux, F_{sw}, around noon at the 26 to 29 May and the difference in the net surface longwave radiation flux, F_{lw}, around midnight at the 26 to 29 May between simulation C and REF is shown as a function of the vertically averaged N_d at cloud ice containing grid cells in case C. During noon, the distribution of the differences in F_{sw} show a decrease as a function of N_d reaching $-75\,W\,m^{-2}$ at $N_d = 100\,cm^{-3}$. The distribution of differences in F_{lw} show a slight increase as a function of N_d. This can be explained by the less effective sedimentation of the smaller ice crystals which can cause a slight increase in the ice water path.

The temporal evolution of the median effective radii of cloud droplets, r_c, and ice crystals, r_i, calculated for domain $D1$, in simulation C and REF is shown in Fig. 6.14. For r_c slightly lower values occur in case C with maximum differences to case REF mostly lower than $1\,\mu m$. In contrast, r_i is significantly lower in simulation C in the order of $10\,\mu m$ to $25\,\mu m$. The difference in r_i scales with the time evolution of the magnitude of r_i. Small r_i indicate that ice clouds occur mainly at greater heights, where the difference in r_i is much smaller due to the controlling influence of homogeneous freezing.

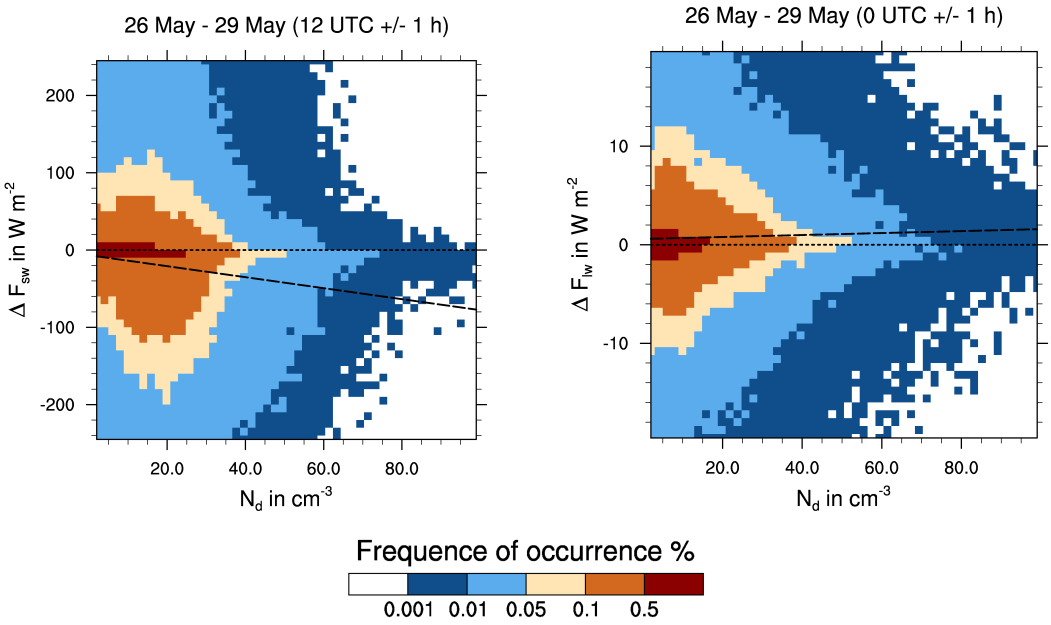

Fig. 6.13.: Joint PDFs of differences (C minus REF) in surface net shortwave radiation flux around noon (left) and in surface net longwave radiation flux around midnight (right) compared with the average dust concentration at grid points containing cloud ice (C). The dashed line is the result of a linear regression fit of the data.

Figure 6.15 shows the temporal evolution of domain averaged cloud properties and radiation fluxes in simulation C and REF. The temporal evolution of averaged vertical integrated cloud water content, LWP, and ice water content, IWP, shows values of similar magnitude in simulation C and REF with positive and negative difference of a few percent. Whereas LWP shows most of the time slightly lower values and IWP slightly higher values in case C. Differences in LWP and IWP are mainly caused by differences in the dynamics of the cloud systems. The average in-cloud vertical velocity, w_{cloud}, shows slightly higher values in case C during the first three days of the dust event. This can be explained by more effective glaciation of mixed phase clouds in case C and the additional release of latent heat. On the last day w_{cloud} is lower in simulation C which is also reflected in a lower LWP. In general, differences in dynamics can be driven by different processes, e.g. changes in radiation and consequently temperature caused by modified cloud properties, and are hard to relate directly with a specific individual process.

In both simulations, the average hourly precipitation rate, R_{1h}, is almost identical. Difference in R_{1h} scale mostly with the differences in LWP and IWP, e.g. during the

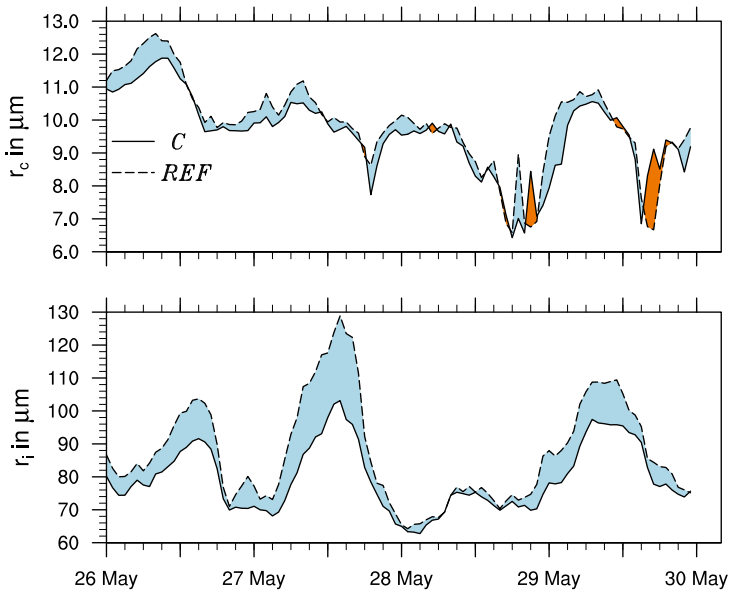

Fig. 6.14.: Time series of the average effective radii of cloud droplets r_c and ice crystal r_i of domain D1. Solid lines are results from simulation C and dashed lines are results from simulation REF. r_c is calculated for gridpoints with a cloud water mass mixing ratio greater than $0.05\,\mathrm{g\,kg^{-1}}$ and r_i for ice crystal mass mixing ratios of more than $0.001\,\mathrm{g\,kg^{-1}}$.

last two days of the dust event were the largest differences occur. Despite the almost identical R_{1h}, the local differences can be large due to spatial shifts in the distribution of precipitation.

The domain average F_{sw} shows systematic differences between simulation C and REF with lower values in simulation C. The maximum F_{sw} is reduced significantly in case C by 10 to $20\,\mathrm{W\,m^{-2}}$. The largest difference in F_{sw} occurs on 27 May with $20\,\mathrm{W\,m^{-2}}$ lower values in case C. During this day the dust amount is highest in the model domain. Because LWP and IWP are almost identical in both simulations, the difference in F_{sw} can be directly related to the impact of the dust particles on the radiative properties of the ice clouds in case C (Fig. 6.13). The temporal evolution of the average F_{lw} shows only small differences between simulation C and REF with a maximum of $+1.5\,\mathrm{W\,m^{-2}}$.

The difference in the net radiation fluxes at the surface have an impact on the simulated temperatures. The domain averaged daily temperature maximum of the temperature in a height of 2 m above ground, $T_{2\,\mathrm{m}}$ is up to 0.3 K lower in case C than in case REF. $T_{2\,\mathrm{m}}$ is lower in case C until the daily temperature minimum is reached in the early

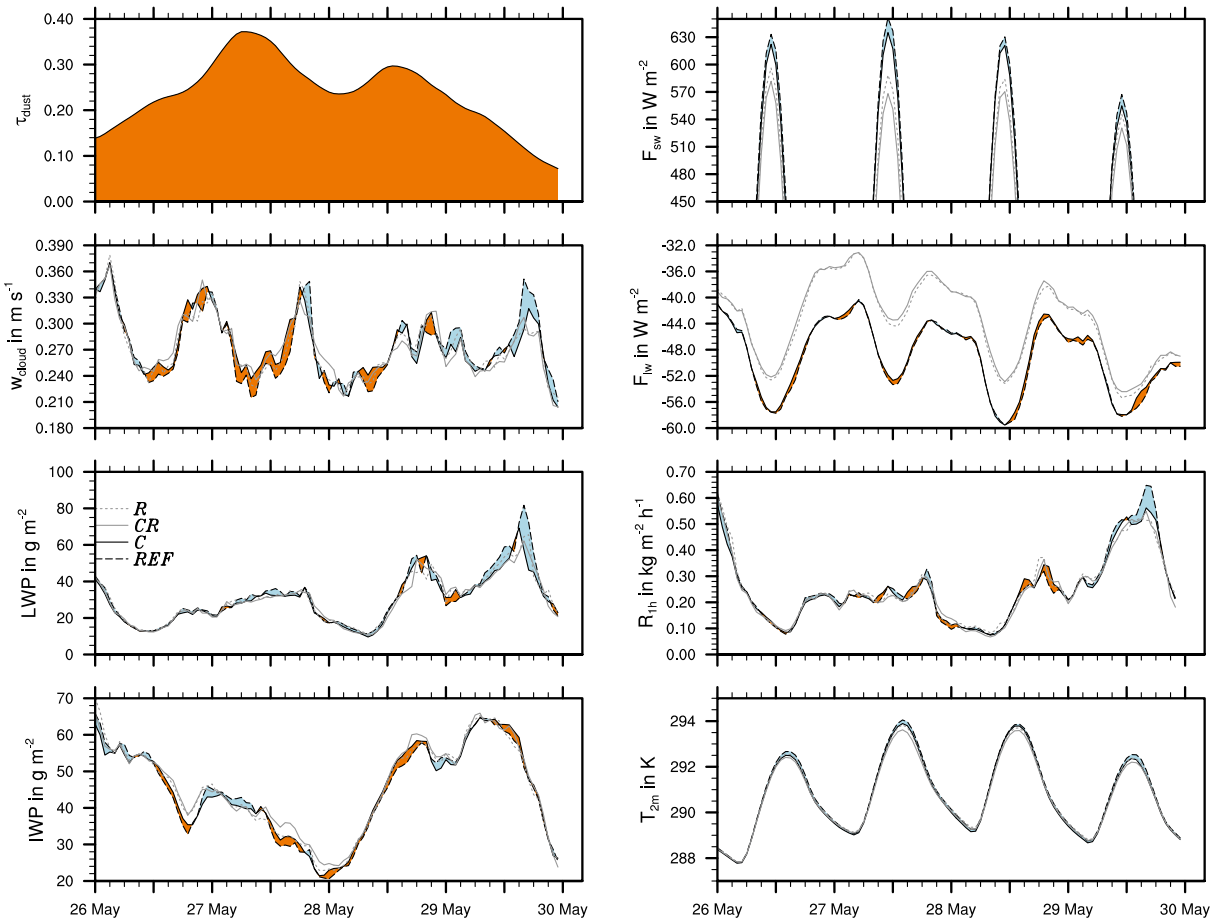

Fig. 6.15.: Time series of dust optical thickness (τ_{dust}), cloud properties (w_{cloud}, LWP, and IWP), precipitation rate (R_{1h}), net surface radiation fluxes (F_{sw} and F_{lw}), and temperature ($T_{2\,\text{m}}$) averaged for domain D1 for simulation C (black solid lines), REF (black dashed lines), CR (gray dashed lines), and R (dotted gray lines). Differences between simulation C and REF are highlighted with shadings.

morning, where $T_{2\,\text{m}}$ in both simulations converge again. Despite the small difference in the domain average $T_{2\,\text{m}}$, the differences are locally much larger. This will be discussed in Sect. 6.6.

6.5. Direct Dust Impact on Radiation

Until now, only the impact of dust on the atmospheric state due to the interaction of dust particles with cloud microphysical and optical properties was investigated. During the dust event the dust particles interact also directly with the radiative fluxes due to scattering and absorption of short and longwave radiation. Results of simulation R, which

considers only the direct interaction of dust particles with radiation, and simulation CR, which includes additionally to the interaction with the clouds also the direct interaction of dust particles with radiation, are shown together with the results of simulation C and REF in Fig. 6.15.

The domain averaged dust optical depth at a wavelength of 550 nm, τ_{dust}, increases during the dust event up to 0.36 at the 27 May. During the last two days of the dust event τ_{dust} decreases again to 0.1. The additional direct interaction of the dust particles with radiation in case CR causes lower values of F_{sw} of up to $-80\,W\,m^{-2}$ in maximum at 27 May in comparison to case REF. On the other days of the dust event the maximum F_{sw} is 40 to $60\,W\,m^{-2}$ lower in case CR with respect to case REF. Due to the interaction of the dust particles with the longwave radiation fields F_{lw} is in the order of 3 to $10\,W\,m^{-2}$ higher in case CR in comparison to the cases C and REF.

The differences in F_{sw} and F_{lw} between case CR and case C and the differences between case R and case REF are consistent. This shows that changes in cloud cover and cloud properties induced by the direct interaction of the dust with radiation are negligible in the presented case.

The direct impact of the dust particles in simulation CR causes lower daily maxima of $T_{2\,m}$ when compared to simulation C. The domain averaged $T_{2\,m}$ is 0.5 K lower in CR in comparison to REF at the 27 May. During the night $T_{2\,m}$ converge in the different simulations and get even slightly higher values of $T_{2\,m}$ in case CR in comparison to C due to the higher values of F_{lw}.

The temperature decreases during the day in R in comparison with REF (by the direct radiative impact of dust) and in C (by the interaction of dust with the cloud properties) in comparison to REF are comparable in magnitude. The sum of both effects is comparable with the temperature decrease in CR in comparison to REF (by the combined direct radiative impact of dust and the interaction of dust with the cloud properties).

Whether the direct impact on the radiation or the interaction with the clouds has the larger impact on the domain averaged $T_{2\,m}$ varies from day to day depending on the spatial distribution of clouds and dust particles.

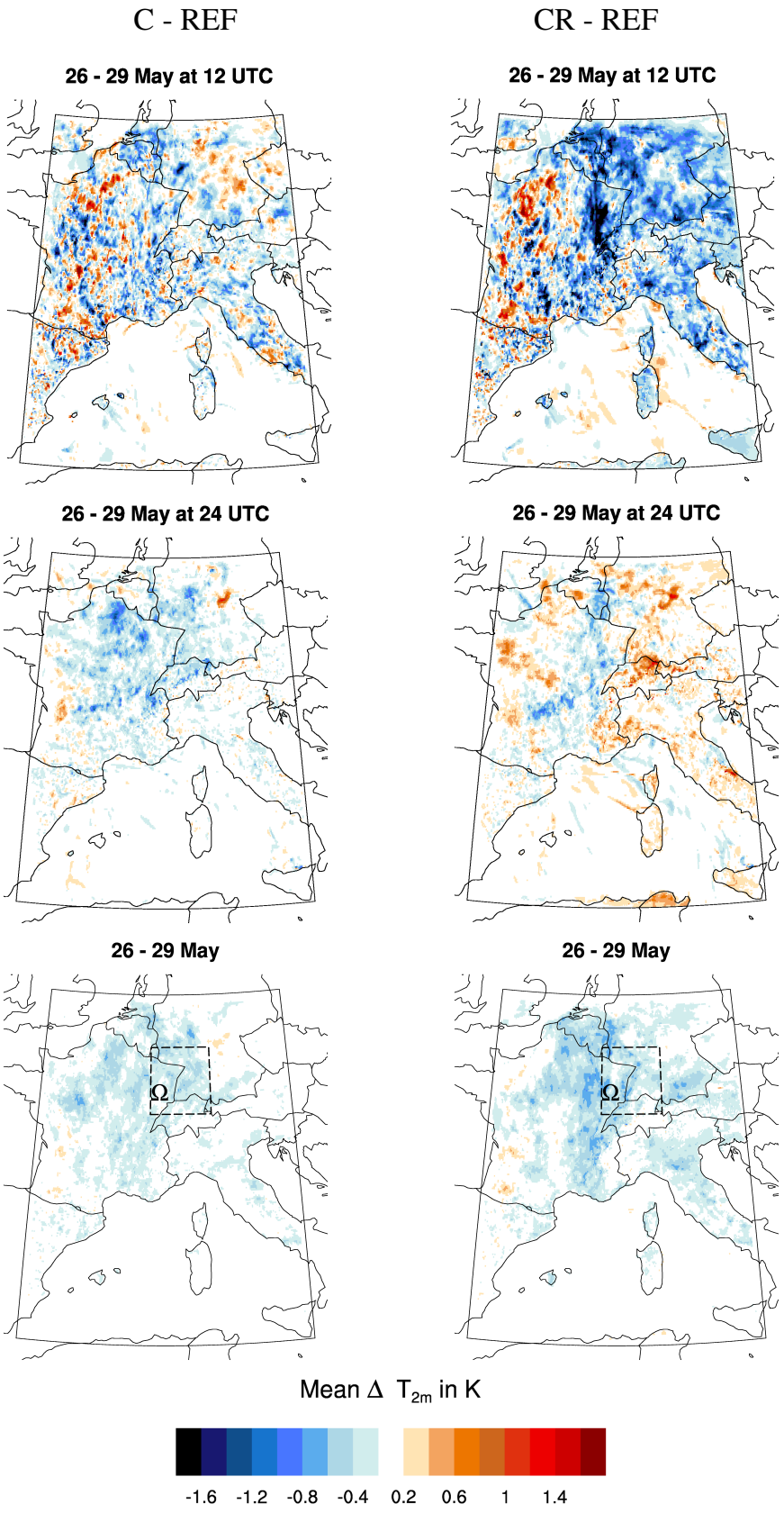

Fig. 6.16.: Mean difference in $T_{2\,\mathrm{m}}$ at 12:00 UTC and 24:00 UTC from 26–29 May 2008 and total mean difference in $T_{2\,\mathrm{m}}$ from 26–29 May 2008 between simulation C and REF (left column) and simulation CR and REF (right column).

6.6. Impact on $T_{2\,m}$

In Fig. 6.16 the impact of the dust on average $T_{2\,m}$ is depicted for interaction with cloud properties only (C minus REF) and for direct interaction with radiation together with the interaction with cloud properties (CR minus REF) for the whole model domain. The $T_{2\,m}$ for case C at noon is systematically lower over the continent by -0.2 to -1 K. Isolated areas where $T_{2\,m}$ in case C is higher than in case REF can be attributed to small spatial and temporal differences in the distribution of the clouds. The difference in $T_{2\,m}$ at midnight is lower in comparison to noon time. The $T_{2\,m}$ at midnight in case C is lower by -0.1 to -0.4 K over the continent. The maximum difference is in the eastern part of France. On average over the whole dust event (26–29 May) $T_{2\,m}$ in case C is systematically lower than in case REF by -0.2 to -0.5 K over the continent. The maximum differences in $T_{2\,m}$ are in the areas of the maximum average dust concentrations (Fig. 6.6).

The average difference in $T_{2\,m}$ from combined interaction of dust with clouds and radiation (difference between simulation CR and REF) shows negative values during noon time of up to -1.8 K in the areas of the maximum dust concentrations. During midnight, the average difference in $T_{2\,m}$ is only negative in the areas with a high negative difference during daytime. In all other areas the difference is slightly positive with values up to $+1$ K locally. The average difference in $T_{2\,m}$ between the simulations CR and REF calculated for the whole period of the dust event shows systematically negative values in the order of -0.2 K for the whole continent with maxima up to -1 K locally.

As mentioned before, an analysis of the weather forecast results for SW-Germany showed too high $T_{2\,m}$ (by up to $+2$ K) in comparison with station observations in the afternoon during the dust event. In the early morning hours, the predicted $T_{2\,m}$ were almost identical with the observations (Fig. 6.1).

In Fig. 6.17 the temporal evolution of the simulated $T_{2\,m}$ averaged over an area including SW-Germany, Ω, is shown for REF, C, R, and CR. The differences in $T_{2\,m}$ between C, R, and CR and REF reaches the maximum values in the afternoon. In the early morning hours $T_{2\,m}$ in the different simulations converge and are almost identical. This is in agreement with the daily evolution of the bias between operational forecast and observations. Beside the 28 May, $T_{2\,m}$ in case R is higher (+0.1 K to +0.3 K) during the night in comparison to REF due to the higher incoming longwave radiation at the surface (Fig.

6.15). The average difference is -0.28 K between C and REF, -0.15 K between R and REF, and -0.32 K between CR and REF during the 26–29 May 2008. The differences between C and REF, and R and REF are of similar magnitude during day time, whereas the impact of dust on $T_{2\,\mathrm{m}}$ was dominated by the interaction of dust with clouds at the 26 May and 29 May and by the direct interaction of dust with radiation at the 27 May and 28 May. The difference between CR and REF reaches -0.65 K to -1 K at the afternoon, which is consistent with the sum of the differences between R and REF, and C and REF most of the time. This shows that the additional direct radiation impact of dust in CR does not significantly modify the simulated clouds. This indicates that so-called semi-direct effects of the dust, which describe the modification of cloudiness caused by an increase in temperature due to absorption of particles in the cloud layers for instance, are of minor importance in this case.

The simulation results presented in this study indicate that the bias in the operational weather forecast can be attributed to the missing interaction of the dust particles with clouds and radiation. Although the observed bias of $T_{2\,\mathrm{m}}$ in the weather forecast is two times larger than the simulated maximum difference in $T_{2\,\mathrm{m}}$ in the area Ω; the daily cycles are comparable. The differences in the magnitude can be explained by uncertainties in the cloud cover and in the exact position of the dust plume; e.g. the differences in $T_{2\,\mathrm{m}}$ in Eastern France reach magnitudes comparable to the observed bias.

Both processes (the interaction with clouds and the direct interaction with the radiation) contribute in a similar magnitude to the simulated differences in $T_{2\,\mathrm{m}}$. Whether the direct impact on the radiation or the interaction with the clouds has the bigger impact on $T_{2\,\mathrm{m}}$ depends on the spatial distribution of clouds and dust particles.

6.7. Conclusions

The impact of mineral dust particles on clouds, radiation, and atmospheric state during a strong Saharan dust event over Europe in May 2008 was investigated, applying a comprehensive online-coupled regional model framework that explicitly treats particle microphysics and chemical composition. Sophisticated parameterizations for aerosol activation and ice nucleation, together with two-moment cloud microphysics are used to calculate the interaction of the different particles with clouds depending on their physical and chemical properties.

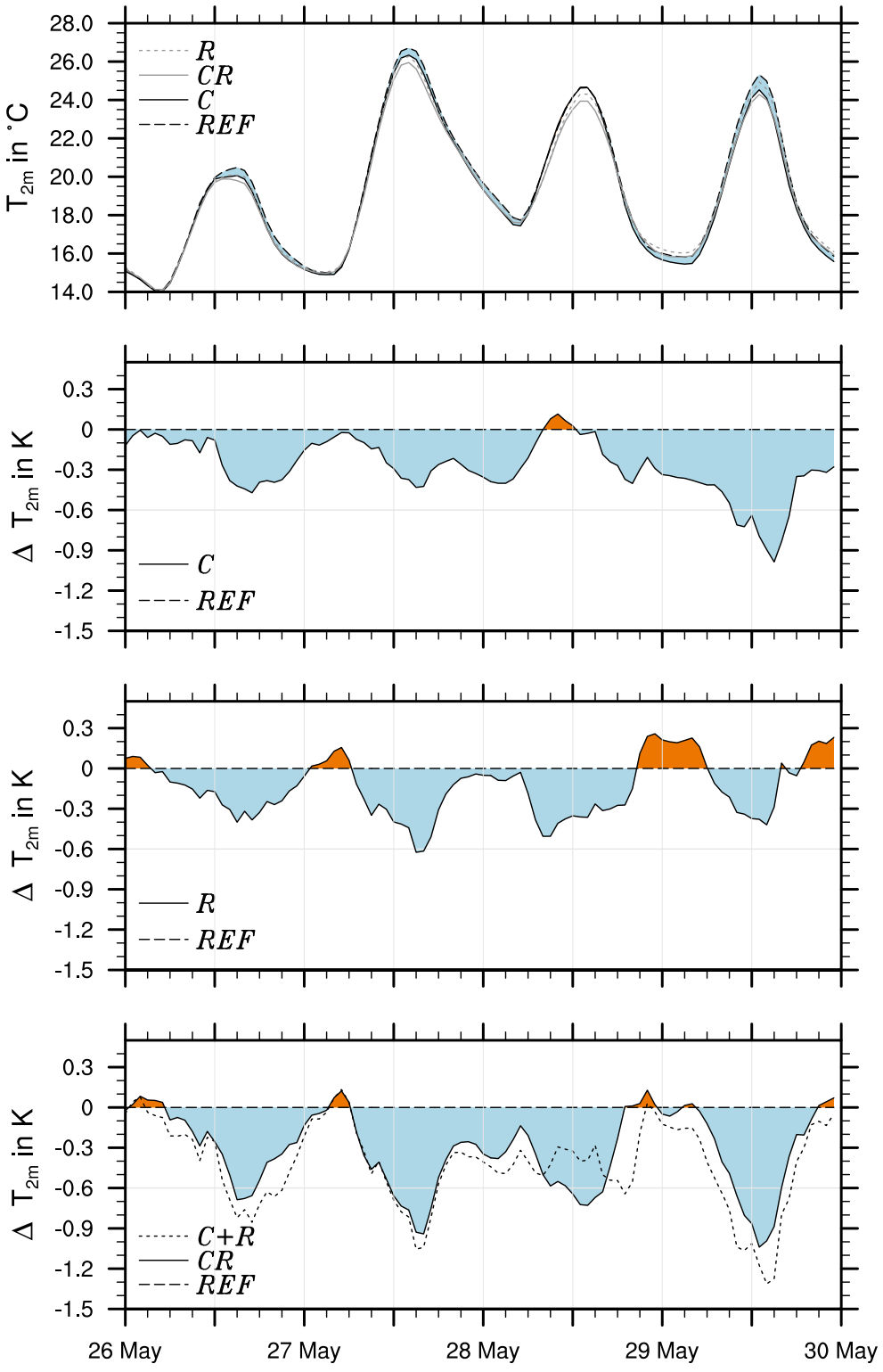

Fig. 6.17.: Temporal evolution of $T_{2\,\mathrm{m}}$ for the individual simulations (top) and differences in $T_{2\,\mathrm{m}}$ of the individual simulations with respect to case REF for area Ω (see Fig. 6.16). Additionally to the difference between CR and REF (bottom) the sum of the differences between R and REF, and between C and REF is shown (dotted line, C+R).

It was shown that the model framework is able to reproduce the measured aerosol mass concentrations during the dust event reasonably well and capture the aerosol background before the arrival of the dust, as well as the spatial distributions of the clouds in comparison with satellite measurements. Dust particles act as CCN and IN in the atmosphere and can interact with clouds in several ways depending on the atmospheric conditions and cloud type.

For temperatures lower than the level of homogeneous freezing the dust particles have to compete with the homogeneous freezing of liquid aerosol particles for water vapor during the ice nucleation. Though the concentration of frozen dust particles is up to $100\,\mathrm{L}^{-1}$ during the ice nucleation events no significant impact on the number and mass concentration of ice crystals was found in this temperature range.

The impact of the dust on cloud droplet number concentration was found to be low, with just a slight increase in cloud droplet number concentration for both uncoated and coated dust. The number of activated dust particles was found to be in the order of 1 to $20\,\mathrm{cm}^{-3}$, with higher numbers in the case of the coated dust particles. The additional activation of dust particles caused lower maximum supersaturations during the activation process, especially in the case of the coated dust particles.

Mineral dust particles are found to have the largest impact on clouds in a temperature range between freezing level and the level of homogeneous freezing, where they determine the number concentration of ice crystals due to efficient heterogeneous freezing of the dust particles and modify the glaciation of mixed phase clouds. Our simulations show that during the dust events ice crystals concentrations were increased twofold in this temperature range in comparison to a reference simulations which neglects the interaction of the dust with the atmosphere. As a consequence the liquid water fraction was reduced significantly with 60 % less grid points containing cloud water in the temperature range between 263 K to 235 K.

The strong increase in ice crystal number concentration has an influence on the optical properties of the ice clouds during the time of the dust event due to a significant decrease of effective radii of the ice crystals in the order of up to $-25\,\mu\mathrm{m}$ on average. It was shown that depending on the number concentration of dust available for ice nucleation the incoming short-wave radiation at the surface was reduced up to $-75\,\mathrm{W\,m}^{-2}$ at $N_\mathrm{d} = 100\,\mathrm{cm}^{-3}$. Consequently, a reduction in surface temperature in the order of up to 1 K over Europe during the day time arises from aerosol-cloud interactions. In the

morning hours, the surface temperatures agree again between the different simulations. On average over the whole period of the dust event a reduction in surface temperature in the order of $-0.2\,\mathrm{K}$ to $-0.4\,\mathrm{K}$ was found in the eastern part of France and Western Germany.

The simulated aerosol optical thickness of the dust particles was found to be in the order of 0.2 to 0.5 on average during the dust event over Europe. This caused an additional reduction in the incoming short-wave radiation which was found to be in the order of $-80\,\mathrm{W\,m^{-2}}$ on 27 May. On the other days of the event the reduction was found to be in the order of -40 to $-60\,\mathrm{W\,m^{-2}}$. In contrast to the aerosol-cloud interaction only, the incoming long-wave radiation at the surface was increased significantly in the order of $+10\,\mathrm{W\,m^{-2}}$.

The direct impact on radiation together with the impact on the clouds caused lower surface temperatures of up to $-1.8\,\mathrm{K}$ in the areas of the maximum dust concentrations during the daytime. Due to the enhanced incoming long-wave radiation a temperatures increase was found for most parts of Europe during the night time. Only in the areas with the maximum temperature difference during the day the night temperatures were still below the ones simulated neglecting the interaction of dust with the atmosphere.

On average the overall impact of the dust caused a reduction in surface temperature in the order of -0.2 to $-0.5\,\mathrm{K}$ for most parts of France, Germany, and Italy during the dust event. The maximum difference in surface temperature was found in the East of France, the Benelux, and Western Germany with up to $-1\,\mathrm{K}$.

The simulations suggest that the bias which was found in numerical weather forecast during the period of the dust event can be explained by the missing aerosol cloud interaction in current weather forecast simulations. Weather forecast models use climatological aerosol conditions to represent the aerosol optical thickness and calculate ice crystal and clouds droplet number concentrations. Hence they are not able to represent conditions which differ significantly from the climatological values, which is the case during strong dust events over Europe.

7. Summary and Conclusions

In this thesis a new comprehensive model framework for the investigation of the interaction of atmospheric aerosol particles with clouds on the regional scale was presented, which is able to simulate gas-phase, aerosol, and cloud processes with a comparable level of complexity. New aspects of aerosol-cloud interaction resulting from the explicit simulation of the aerosol chemical and physical properties were highlighted. The impact of natural and anthropogenic aerosol particles on cloud properties and precipitation was studied and quantified for Western Europe in two case studies focusing on different aspects of aerosol-cloud interaction.

Aerosol particles interact with clouds by acting as condensation or freezing nuclei during cloud formation with numerous consequences for cloud properties and cloud development. The regional model-framework COSMO-ART was extended to consider the activation of aerosol particles, homogeneous and heterogeneous freezing of aerosol particles, the impact on cloud microphysics and precipitation, and the impact on cloud optical properties. For the representation of activation and freezing of aerosol particles, new comprehensive parameterizations were included to consider the physical and chemical properties of the simulated aerosol population as well as the competition of the different aerosol particles for water vapor. To analyze the complex feedback mechanisms related to the cloud microphysical processes, a comprehensive cloud scheme was included in the model framework to simulate mass and number concentrations of cloud droplets, ice crystals, rain, snow, graupel, and hail. To consider the impact of the varying cloud droplet and ice crystal size on cloud optical properties, new parameterizations were introduced in the radiation scheme of COSMO-ART to calculate optical properties of cloud droplets and crystals as a function of their effective radius. As a result, COSMO-ART is a unique and powerful tool to investigate the interaction of aerosol particles with clouds and to quantify the impact of aerosol particles on precipitation, radiation, and the state of the atmosphere.

In the first study presented in this thesis the model framework was applied to Europe for a period in August 2005, which was characterized by cloudy conditions and precipitation in large parts of the domain. This study focused on correlating the aerosol and cloud distribution and the impact of aerosol particles acting as CCN on cloud number concentration and precipitation.

It was found that the mean cloud droplet number concentration depends on the structure of the terrain. The orographically induced vertical velocities have a significant impact on the activation of aerosol particles, resulting in a higher susceptibility of the cloud droplet number concentration to CCN in more structured terrain. A terrain slope parameter TS was presented to classify this dependency, and a simple parameterization was presented to consider the relation of in-cloud updrafts and TS in large-scale models.

It was demonstrated that the distribution of CCN and clouds are strongly correlated. In cloudy areas the concentration of CCN is increased in comparison to cloud-free areas, especially at higher altitudes. It was shown that this is caused partly by an efficient nucleation of secondary aerosol particles in the cloudy areas. As a consequence, the explicit treatment of gas-phase photochemical processes is crucial to the simulation of CCN distributions and, hence, to the quantification of processes related to the aerosol-cloud interaction.

By giving a fixed aerosol distribution, the changes in cloud properties and precipitation caused by aerosol variations were investigated. It was shown that the changes in cloud droplet number concentration and cloud droplet radii are clearly correlated with the change in the CCN concentration. The impact of aerosol variations on precipitation was shown to be more complex, with a slightly enhanced precipitation in the maritime stratus because of less CCN and spatial and temporal shifts in the precipitation over the continent where mixed-phase clouds are dominant. To investigate the response of precipitation formation to aerosol changes in more detail, the precipitation susceptibility parameter, which relates the magnitude and sign of changes in the precipitation to changes in the CCN concentration, was calculated for the whole model domain with an hourly resolution. Thus, different clouds types and different development stages of the individual clouds were considered contrary to previous studies. It was shown that the hourly precipitation susceptibility has a broad range of values, with positive and negative values occurring almost in the same amount. This suggests that the aerosol impact on precipitation of individual clouds may differ substantially and that the aerosol-precipitation

system is buffered well on the regional scale. The mean precipitation susceptibility was slightly positive in the simulation, which indicates that at least for some specific conditions, for instance in the early stage of cloud development and for ice-free stratus clouds, an increase in CCN systematically slows down precipitation formation and vice versa. By relating the absolute precipitation susceptibility to the cloud liquid water path, it was shown that precipitation formation in clouds with a liquid water path in the order of 0.85 $\mathrm{kg\,m^{-2}}$ is most susceptible to aerosol changes.

In the second study presented in this thesis, the impact of mineral dust particles on clouds, radiation, and atmospheric state during a strong Saharan dust event over Europe in May 2008 was investigated. Using the new extended model framework, the competition of dust particles with anthropogenic and sea-salt particles during activation and freezing could be simulated explicitly. Several simulations addressing different aspects of the interaction of dust particles with clouds and radiation were presented to quantify the impact of the individual processes on cloud properties, radiation, and 2-meter temperature depending on the physical and chemical properties of the particles.

During the period of the dust event, a temperature bias was identified by operational weather forecast. Weather forecast models use climatological aerosol conditions to represent the aerosol optical thickness and calculate ice crystal and cloud droplet number concentrations. Hence, they are not able to represent conditions differing significantly from the climatological values, which is the case during strong dust events over Europe. It was investigated whether the temperature bias observed during the dust event can be explained by the interaction of the dust particles with clouds and the state of the atmosphere.

It was found that the simulated dust plume as well as the simulated anthropogenic and natural aerosol background was captured well spatially and temporally in the simulations in comparison to surface aerosol measurements. It was shown that the model framework is able to capture the spatial distribution of clouds reasonably well compared to satellite measurements.

The impact of dust particles on the cloud droplet number concentrations was investigated for coated and uncoated dust particles. In both cases, the impact on the cloud droplet number concentrations was low with a slight increase in the cloud droplet number concentrations only. The number of activated dust particles reached 1 to $20\,\mathrm{cm^{-3}}$, with higher numbers in the case of the coated dust particles. This contributes a few per-

cent only to the total number of activated particles. Additionally, the maximum supersaturation with respect to water reached during cloud formation is lower, if dust particles are present. This buffers the impact of the additional dust particles on the cloud droplet number concentration especially in the case of coated dust particles, because fewer small particles are activated at lower supersaturations. Both the low relative contribution to the total number of activated particles and the feedback with the maximum supersaturation explain the low impact of the dust particles on the cloud droplet number concentration over Europe.

Dust particles are known to be efficient nuclei for ice formation in the atmosphere. For temperatures below the level of homogeneous freezing ($\approx 235\,\mathrm{K}$), no significant impact of the dust on the ice crystal number concentrations was found. At these temperatures, the freezing of dust competes with the homogeneous freezing of liquid aerosol droplets. Although the number concentrations of freezing dust particles reached values of up to $100\,\mathrm{L}^{-1}$, homogeneous freezing of droplets was the dominant process in this temperature range.

The dust particles were found to significantly increase the ice crystal number concentration by a factor of two for temperatures above the homogeneous freezing level during the dust event. As a consequence, the glaciation of mixed-phase clouds was modified with 60 % less grid points containing cloud water in the temperature range between 263 K and 235 K compared to the reference simulation, which neglects the interaction of dust with the atmosphere.

The impact of dust-cloud interaction on the average cloud water path and average ice water path was low, with changes of a few percent only. Whereas the average cloud water path showed slightly lower values for the most of the time, the average ice water path exhibited slightly higher values when the interaction of dust with clouds was included.

The increase in ice crystal number concentrations was found to have a significant impact on the optical properties of the clouds due to a decrease of the effective radii of the ice crystals of up to $-25\,\mu\mathrm{m}$ on the average. It was shown that the net shortwave radiation flux at the surface was reduced depending on the average dust number concentration at ice-containing grid points, with the values reaching up to $-75\,\mathrm{W\,m^{-2}}$ for a dust number concentration of $100\,\mathrm{cm^{-3}}$. The impact on the net longwave radiation flux at the surface was less pronounced with a slight increase as a function of the average dust concentration at ice-containing grid points.

The impact of the dust particles on clouds and their optical properties caused a reduction of the 2-meter temperature during the dust event of up to -1 K. On the average, a reduction of 2-meter temperature in the order of $-0.2\,\mathrm{K}$ to $-0.4\,\mathrm{K}$ was found in the eastern part of France and Western Germany over the whole period of the dust event.

Besides their impact on clouds, dust particles modify the atmospheric radiation budget directly by scattering and absorption of radiation. A simulation considering the direct radiation impact of the dust particles only was presented and compared to the simulation that included the interaction of dust with clouds only. It was shown that the direct impact of dust significantly reduces the net shortwave radiation during the dust event by up to $-80\,\mathrm{W\,m^{-2}}$. In contrast to the interaction with clouds, however, also the net longwave radiation at the surface is increased by $10\,\mathrm{W\,m^{-2}}$. As a result, the 2-meter temperatures increase during the night, if the direct impact of dust on radiation is considered. Both the dust impact on cloud properties and the direct dust impact on radiation caused differences in the 2-meter temperature of similar magnitude during daytime. Depending on the spatial distribution of clouds and dust particles, direct impact on radiation was larger or smaller than the interaction with the clouds.

An additional simulation was carried to consider the direct impact on radiation together with the impact on the clouds. It was shown that the overall impact of the dust particles caused lower 2-meter temperatures of up to $-1.8\,\mathrm{K}$ in the areas of the maximum dust concentrations during daytime. At night, a temperature increase was found in most parts of Europe due to the enhanced incoming long-wave radiation. Only in the areas with the maximum temperature difference during daytime were the temperatures at night still below those simulated by neglecting the interaction of dust with the atmosphere.

An analysis of the temperature differences in the area where the temperature bias had been detected by the operational weather forecast revealed that the direct impact of the dust particles on radiation and the impact of the dust particles on clouds contributed almost equally to the reduction of the 2-meter temperature in this area. A comparison of the simulations treating both processes separately with the simulation including all processes together showed that feedbacks between the direct radiation impact of dust and clouds are of minor importance in this case.

The presented results suggest that the bias found in the operational weather forecast simulations during the time of the dust event can be explained by the missing aerosol-cloud-radiation interaction in the current weather forecast simulations.

7.1. Overall Conclusions

The aim of this thesis was to improve our understanding of the aerosol-cloud interaction by using a new sophisticated model framework. In the introduction general scientific questions relating to the aerosol-cloud interaction were formulated.
Are there systematic patterns in the distributions of aerosol number and mass concentration as well as cloud droplet number concentration? Are there close links between them?

> No direct correlation between the aerosol number concentration or aerosol mass concentration and the cloud droplet number concentration was found. This suggests that the aerosol size distribution and chemical composition or directly the CCN concentration at a suitable supersaturation have to be measured or simulated explicitly in studies focusing on the aerosol-cloud interaction and cannot be replaced by, for instance, correlations of CCN with the aerosol number or mass concentration only. It was shown that the cloud droplet number concentrations correlate well with the CCN concentrations at 0.1 % supersaturation. (Sect. 5.2)
>
> The aerosol number concentrations and CCN concentrations are significantly enhanced in the vicinity of clouds in the presented simulations. The nucleation of aerosol particles is enhanced in the vicinity of clouds. This indicates that photochemical processes strongly influence the CCN distribution in cloudy areas. (Sect. 5.4)

Is there a relation among the aerosol, topography, and cloud droplet number concentrations?

> The simulated mean in-cloud updrafts were shown to be higher in structured terrain than in flat terrain for Europe. As a consequence, the cloud droplet number concentrations over structured terrain are more susceptible

to variations of the CCN concentrations. This relationship of in-cloud updraft, aerosol concentration, and cloud droplet number concentration can be used to improve the representation of sub-grid scale activation in large-scale models. (Sect. 5.3)

How are precipitation patterns altered when the interactions of the aerosol particles and cloud processes are taken into account on the regional scale? Are there any systematic effects?

In the case study presented variations of the aerosol concentration caused spatial and temporal shifts in the precipitation distribution over Europe and the precipitation was slightly reduced over the ocean when aerosol concentration was increased. By an analysis of the hourly precipitation susceptibility to CCN concentrations for Europe, it was found that clouds with a liquid water path of approximately $0.85\,\mathrm{kg\,m^{-2}}$ are most susceptible to the CCN concentration. It was shown that both increases and decreases in the precipitation rate are triggered by CCN changes of almost the same amount, with a slight tendency to an increase in precipitation for a reduction in the CCN concentration and vice versa. (Sect. 5.5)

Is there any significant aerosol impact on cloud properties and the radiation budget on short time scales, especially during extraordinary aerosol events like dust storms?

The simulations of a dust event in May 2008 demonstrated that dust storms modify cloud properties and the radiation budget over Europe significantly. This is mainly due to the dust acting as nuclei for the formation of ice crystals. The impact of coated and uncoated dust particles on cloud droplet number concentrations was shown to be low because of the high number concentrations of anthropogenic and sea salt particles. (Sect. 6.3)

The net shortwave radiation at the surface was decreased as a consequence of the strongly decreased mean effective radius of the ice crystals and the direct radiation impact of the dust. The net longwave radiation at the surface was increased in both cases, with the direct impact of the dust being much more pronounced. (Sect. 6.4 and Sect. 6.5)

How strong is the impact of Saharan dust events on the 2-meter temperature and the state of the atmosphere over Europe? Are there consequences for operational weather forecast?

The analyzed Saharan dust event caused a systematic decrease of the 2-meter temperature by -1 K in the dust-affected regions in Europe. The simulated impact on 2-meter temperature is consistent with a bias detected in the operational temperature forecast. This implies that aerosol conditions which strongly deviate from climatological values cause systematic uncertainties in the current operational weather forecast. For this reason, the simulation of aerosol particles and their impact on clouds and radiation should be included in future operational weather forecast models. (Sect. 6.6)

A. Bibliography

Abdul-Razzak, H. and S. Ghan, 2000: A parameterization of aerosol activation 2. Multiple aerosol types. *J. Geophys. Res.-Atmos.*, **105 (D5)**, 6837–6844, doi:10.1029/1999JD901161.

———, 2002: A parameterization of aerosol activation - 3. Sectional representation. *J. Geophys. Res.-Atmos.*, **107 (D3)**, 4026, doi:10.1029/2001JD000483.

Aitken, J., 1880: On dust, fogs, and clouds. *Trans. Roy. Soc. Edn.*, **30**, 337–368.

Albrecht, B. A., 1989: Aerosols, cloud microphysics, and fractional cloudiness. *Science*, **245 (4923)**, 1227–1230, doi:10.1126/science.245.4923.1227.

Baldauf, M., A. Seifert, J. Förstner, D. Majewski, M. Raschendorfer, and T. Reinhardt, 2011: Operational convective-scale numerical weather prediction with the COSMO model: description and sensitivities. *Mon. Weather Rev.*, doi:10.1175/MWR-D-10-05013.1, e-View.

Bangert, M., 2006: Eine Parametrisierung für die Berechnung von Photolysefrequenzen in Chemie-Transport-Modellen. Seminararbeit (in German), Institute for Meteorology and Climate Research, University of Karlsruhe (TH), Karlsruhe.

———, 2008: Berücksichtigung des Einflusses von anthropogenem Aerosol auf warme Wolken in COSMO-ART. Diplomarbeit (in German), Institute for Meteorology and Climate Research, University of Karlsruhe (TH), Karlsruhe.

Bangert, M., C. Kottmeier, B. Vogel, and H. Vogel, 2011: Regional scale effects of the aerosol cloud interaction simulated with an online coupled comprehensive chemistry model. *Atmos. Chem. Phys.*, **11 (9)**, 4411–4423, doi:10.5194/acp-11-4411-2011.

Bangert, M., A. Nenes, B. Vogel, H. Vogel, D. Barahona, V. A. Karydis, P. Kumar, C. Kottmeier, and U. Blahak, 2012: Saharan dust event impacts on cloud formation

and radiation over Western Europe. *Atmos. Chem. Phys.*, **12 (9)**, 4045–4063, doi: 10.5194/acp-12-4045-2012.

Barahona, D. and A. Nenes, 2008: Parameterization of cirrus cloud formation in large-scale models: Homogeneous nucleation. *J. Geophys. Res.-Atmos.*, **113 (D11)**, D11 211, doi:10.1029/2007JD009355.

———, 2009a: Parameterizing the competition between homogeneous and heterogeneous freezing in cirrus cloud formation - monodisperse ice nuclei. *Atmos. Chem. Phys.*, **9 (2)**, 369–381, doi:10.5194/acp-9-369-2009.

———, 2009b: Parameterizing the competition between homogeneous and heterogeneous freezing in ice cloud formation - polydisperse ice nuclei. *Atmos. Chem. Phys.*, **9 (16)**, 5933–5948, doi:10.5194/acp-9-5933-2009.

Barahona, D., J. Rodriguez, and A. Nenes, 2010a: Sensitivity of the global distribution of cirrus ice crystal concentration to heterogeneous freezing. *J. Geophys. Res.-Atmos.*, **115**, D23 213, doi:10.1029/2010JD014273.

Barahona, D., R. E. L. West, P. Stier, S. Romakkaniemi, H. Kokkola, and A. Nenes, 2010b: Comprehensively accounting for the effect of giant ccn in cloud activation parameterizations. *Atmos. Chem. Phys.*, **10 (5)**, 2467–2473, doi:10.5194/acp-10-2467-2010.

Beheng, K. D., 1982: A numerical study on the combined action of coagulation, ice particle riming and the splintering process concerning maritime cumuli. *Beitr. Phys. Atm.*, **55**, 201–214.

Bergeron, T., 1935: On the physics of cloud and precipitation. *Proc. 5th Assembly UGGI Lisbon*, Vol. 2, 156.

Blahak, U., 2008: Towards a better representation of high density ice particles in a state-of-the-art two-moment bulk microphysical scheme. Extended Abstract, International Conference on Clouds and Precipitation, Cancun, 7.7. – 11.7.2008, URL `http://cabernet.atmosfcu.unam.mx/ICCP-2008/abstracts/Program_on_line/Poster_07/Blahak_extended_1.pdf`.

Boucher, O. and U. Lohmann, 1995: The sulfate-ccn-cloud albedo effect - a sensitivity study with 2 general-circulation models. *Tellus*, **47 (3)**, 281–300, doi:10.1034/j.1600-0889.47.issue3.1.x.

Cantrell, W. and A. Heymsfield, 2005: Production of ice in tropospheric clouds - A review. *B. A.M. Meteorol. Soc.*, **86 (6)**, 795+, doi:10.1175/BAMS-86-6-795.

Cavazos, C., M. C. Todd, and K. Schepanski, 2009: Numerical model simulation of the Saharan dust event of 6-11 March 2006 using the Regional Climate Model version 3 (RegCM3). *J. Geophys. Res.-Atmos.*, **114**, D12 109, doi:10.1029/2008JD011078.

Chaboureau, J.-P., E. Richard, J.-P. Pinty, C. Flamant, P. Di Girolamo, C. Kiemle, A. Behrendt, H. Chepfer, M. Chiriaco, and V. Wulfmeyer, 2011: Long-range transport of Saharan dust and its radiative impact on precipitation forecast: a case study during the Convective and Orographically-induced Precipitation Study (COPS). *Q. J. Roy. Meteor. Soc.*, **137**, 236–251, doi:10.1002/qj.719.

Chapman, E. G., W. I. Gustafson Jr., R. C. Easter, J. C. Barnard, S. J. Ghan, M. S. Pekour, and J. D. Fast, 2009: Coupling aerosol-cloud-radiative processes in the WRF-Chem model: Investigating the radiative impact of elevated point sources. *Atmos. Chem. Phys.*, **9 (3)**, 945–964, doi:10.5194/acp-9-945-2009.

Charlson, R. J., S. E. Schwartz, J. M. Hales, R. D. Cess, J. Coakley, J. E. Hansen, and D. J. Hofmann, 1992: Climate forcing by anthropogenic aerosols. *Science*, **255**, 423–430, doi:10.1126/science.255.5043.423.

Cheng, C.-T., W.-C. Wang, and J.-P. Chen, 2007: A modelling study of aerosol impacts on cloud microphysics and radiative properties. *Q. J. Roy. Meteor. Soc.*, **(623)**, 283–297, doi:10.1002/qj.25.

———, 2010: Simulation of the effects of increasing cloud condensation nuclei on mixed-phase clouds and precipitation of a front system. *Atmos. Res.*, **96 (2-3)**, 461–476, doi:10.1016/j.atmosres.2010.02.005.

Coulier, P. J. and E. Mascart, 1875: Note sur une nouvelle proprieté de l' air. *J. de Pharmacie et de Chimie*, **22**, 165–173.

DeMott, P., D. Rogers, and S. Kreidenweis, 1997: The susceptibility of ice formation in upper tropospheric clouds to insoluble aerosol components. *J. Geophys. Res.-Atmos.*, **102 (D16)**, 19 575–19 584, doi:10.1029/97JD01138.

DeMott, P. J., 1990: An exploratory-study of ice nucleation by soot aerosols. *J. Appl. Meteorol.*, **29 (10)**, 1072–1079, doi:10.1175/1520-0450(1990)029<1072:AESOIN>2.0.CO;2.

Doms, G., 2011: A Description of the Nonhydrostatic Regional COSMO-Model, Part I: Dynamics and Numerics. Tech. rep., Deutscher Wetterdienst, Offenbach.

Doms, G., J. Förstner, E. Heise, H.-J. Herzog, D. Mironov, M. Raschendorfer, T. Reinhardt, B. Ritter, R. Schrodin, J.-P. Schulz, and G. Vogel, 2011: A Description of the Nonhydrostatic Regional COSMO-Model, Part II: Physical Parameterization. Tech. rep., Deutscher Wetterdienst, Offenbach.

Dufour, L. and R. Defay, 1963: *Thermodynamics of clouds*. Academic Press New York, New York, 255 p.

DWD, 2012: available online, URL `http://www.dwd.de/bvbw/generator/DWDWWW/Content/Oeffentlichkeit/FE/Bilder/ASFU__NM__Phys__Par__skalentrennung__580,property=default.jpg`, cited jan. 2012.

Edwards, J. M., S. Havemann, J.-C. Thelen, and A. J. Baran, 2007: A new parametrization for the radiative properties of ice crystals: Comparison with existing schemes and impact in a gcm. *Atmos. Res.*, **83 (1)**, 19 – 35, doi:10.1016/j.atmosres.2006.03.002.

EEA, 2011: Airbase - the european air quality database. Tech. rep., European Environment Agency, Copenhagen, URL `www.eea.europa.eu/data-and-maps/data/airbase-the-european-ai%r-quality-database`.

Emmons, L. K., S. Walters, P. G. Hess, J.-F. Lamarque, G. G. Pfister, D. Fillmore, C. Granier, A. Guenther, D. Kinnison, T. Laepple, J. Orlando, X. Tie, G. Tyndall, C. Wiedinmyer, S. L. Baughcum, and S. Kloster, 2010: Description and evaluation of the Model for Ozone and Related chemical Tracers, version 4 (MOZART-4). *Geosci. Model Dev.*, **3 (1)**, 43–67, doi:10.5194/gmd-3-43-2010.

Engstrom, A. and A. M. L. Ekman, 2010: Impact of meteorological factors on the correlation between aerosol optical depth and cloud fraction. *Geophys. Res. Lett.*, **37**, L18 814, doi:10.1029/2010GL044361.

Field, P. R., O. Möhler, P. Connolly, M. Krämer, R. Cotton, A. J. Heymsfield, H. Saathoff, and M. Schnaiter, 2006: Some ice nucleation characteristics of Asian and Saharan desert dust. *Atmos. Chem. Phys.*, **6 (10)**, 2991–3006, doi:10.5194/acp-6-2991-2006.

Findeisen, W., 11938: Die kolloidmeteorologischen Vorgange bei der Niederschlagsbildung. *Meteorol. Z.*, **55**, 121–131.

Fletcher, N., P. Squires, and E. G. Bowen, 1962: *The physics of rainclouds*. University press Cambridge, London, 389 p.

Flossmann, A. I., 1998: Interaction of aerosol particles and clouds. *J. Atmos. Sci.*, **55 (5)**, 879–887, doi:10.1175/1520-0469(1998)055<0879:IOAPAC>2.0.CO;2.

Forkel, R., J. Werhahn, A. Hansen, S. McKeen, S. Peckham, G. Grell, and P. Suppan, 2011: Effect of aerosol-radiation feedback on regional air quality-A case study with WRF/Chem. *Atmos. Environ.*, **(0)**, 1352–2310, doi:10.1016/j.atmosenv.2011.10.009.

Fountoukis, C. and A. Nenes, 2005: Continued development of a cloud droplet formation parameterization for global climate models. *J. Geophys. Res.-Atmos.*, **110 (D11)**, doi:10.1029/2004JD005591.

Fountoukis, C., A. Nenes, N. Meskhidze, R. Bahreini, W. C. Conant, H. Jonsson, S. Murphy, A. Sorooshian, V. Varutbangkul, F. Brechtel, R. C. Flagan, and J. H. Seinfeld, 2007: Aerosol-cloud drop concentration closure for clouds sampled during the International Consortium for Atmospheric Research on Transport and Transformation 2004 campaign. *J. Geophys. Res.-Atmos.*, **112 (D10)**, D10S30, doi:10.1029/2006JD007272.

Fukuta, N. and L. A. Walter, 1970: Kinetics of hydrometeor growth from a vapor-spherical model. *J. Atmos. Sci.*, **27**, 1160–1172, doi:10.1175/1520-0469(1970)027<1160:KOHGFA>2.0.CO;2.

Ghan, S., H. Abdul-Razzak, A. Nenes, Y. Ming, X. Liu, M. Ovchinnikov, B. Shipway, N. Meskhidze, J. Xu, and X. Shi, 2011: Droplet nucleation: Physically-based parameterizations and comparative evaluation. *J. Adv. Model. Earth Syst.*, **3 (10)**, M10 001, doi:10.1029/2011MS000074.

Hänel, G., 1976: The properties of atmospheric aerosol particles as functions of the relative humidity at thermodynamic equilibrium with the surrounding moist air. *Adv. in Geophys.*, **19**, 73–188.

Hegg, D. A., L. F. Radke, and P. V. Hobbs, 1990: Particle-production associated with marine clouds. *J. Geophys. Res.-Atmos.*, **95 (D9)**, 13 917–13 926, doi:10.1029/JD095iD09p13917.

Hoffer, T., 1961: A laboratory investigation of droplet freezing. *J. Meteorol.*, **18 (6)**, 766–778, doi:10.1175/1520-0469(1961)018<0766:ALIODF>2.0.CO;2.

Hoose, C., J. E. Kristjansson, and S. M. Burrows, 2010a: How important is biological ice nucleation in clouds on a global scale? *Environ. Res. Lett.*, **5 (2)**, 024 009, doi:10.1088/1748-9326/5/2/024009.

Hoose, C., J. E. Kristjansson, J.-P. Chen, and A. Hazra, 2010b: A Classical-Theory-Based Parameterization of Heterogeneous Ice Nucleation by Mineral Dust, Soot, and Biological Particles in a Global Climate Model. *J. Atmos. Sci.*, **67 (8)**, 2483–2503, doi:10.1175/2010JAS3425.1.

Hoose, C., U. Lohmann, R. Erdin, and I. Tegen, 2008: The global influence of dust mineralogical composition on heterogeneous ice nucleation in mixed-phase clouds. *Environ. Res. Lett.*, **3 (2)**, 025 003, doi:10.1088/1748-9326/3/2/025003.

Houze, R., 1994: *Cloud dynamics*, International geophysics series, Vol. 53. Academic Press, london, 573 p.

———, 2004: Mesoscale convective systems. *Rev. Geophys.*, **42 (4)**, RG4003, doi:10.1029/2004RG000150.

Hu, Y. X. and K. Stamnes, 1993: An accurate parameterization of the radiative properties of water clouds suitable for use in climate models. *J. Climate*, **6 (4)**, 728–742.

IPCC, 2007: Climate Change 2007: Physical Science Basis. Contribution of Working Group I to the Fourth Assessment Report of the Intergovernmental Panel on Climate Change. Tech. rep., Cambridge, New York.

Ivanova, I. T. and H. G. Leighton, 2008: Aerosol-cloud interactions in a mesoscale model. Part I: Sensitivity to activation and collision-coalescence. *J. Atmos. Sci.*, **65**, 289–308, doi:10.1175/2007JAS2207.1.

Jacobson, M. Z., 2005: *Fundamentals of atmospheric modeling*. Cambridge Univ. Press, New York, 672 p.

Jimenez, J. L., M. R. Canagaratna, N. M. Donahue, A. S. H. Prevot, Q. Zhang, J. H. Kroll, P. F. DeCarlo, J. D. Allan, H. Coe, N. L. Ng, A. C. Aiken, K. S. Docherty, I. M. Ulbrich, A. P. Grieshop, A. L. Robinson, J. Duplissy, J. D. Smith, K. R. Wilson, V. A. Lanz, C. Hueglin, Y. L. Sun, J. Tian, A. Laaksonen, T. Raatikainen, J. Rautiainen, P. Vaattovaara, M. Ehn, M. Kulmala, J. M. Tomlinson, D. R. Collins, M. J. Cubison, E. J. Dunlea, J. A. Huffman, T. B. Onasch, M. R. Alfarra, P. I. Williams, K. Bower, Y. Kondo, J. Schneider, F. Drewnick, S. Borrmann, S. Weimer, K. Demerjian, D. Salcedo, L. Cottrell, R. Griffin, A. Takami, T. Miyoshi, S. Hatakeyama, A. Shimono, J. Y. Sun, Y. M. Zhang, K. Dzepina, J. R. Kimmel, D. Sueper, J. T. Jayne, S. C. Herndon, A. M. Trimborn, L. R. Williams, E. C. Wood, A. M. Middlebrook, C. E. Kolb, U. Baltensperger, and D. R. Worsnop, 2009: Evolution of Organic Aerosols in the Atmosphere. *Science*, **326 (5959)**, 1525–1529, doi:10.1126/science.1180353.

Karydis, V., P. Kumar, D. Barahona, and A. Nenes, 2011: On the effect of insoluble dust particles on global ccn and droplet number. *J. Geophys. Res.*, **116**, D23 204, doi:10.1029/2011JD016283.

Keil, A. and M. Wendisch, 2001: Bursts of Aitken mode and ultrafine particles observed at the top of continental boundary layer clouds. *J. Atmos. Sci.*, **32 (5)**, 649–660, doi:10.1016/S0021-8502(00)00102-6.

Kerminen, V. M. and A. S. Wexler, 1994: Post-fog nucleation of h2so4-h2o particles in smog. *Atmos. Environ.*, **28 (15)**, 2399–2406, doi:10.1016/1352-2310(94)90391-3.

Khain, A. P., 2009: Notes on state-of-the-art investigations of aerosol effects on precipitation: a critical review. *Environ. Res. Lett.*, **4**, 015 004, doi:10.1088/1748-9326/4/1/015004.

Khain, A. P., N. BenMoshe, and A. Pokrovsky, 2008: Factors determining the impact of aerosols on surface precipitation from clouds: An attempt at classification. *J. Atmos. Sci.*, **65 (6)**, 1721–1748, doi:10.1175/2007JAS2515.1.

Klein, H., S. Nickovic, W. Haunold, U. Bundke, B. Nillius, M. Ebert, S. Weinbruch, L. Schuetz, Z. Levin, L. A. Barrie, and H. Bingemer, 2010: Saharan dust and ice nuclei over Central Europe. *Atmos. Chem. Phys.*, **10 (21)**, 10 211–10 221, doi:10.5194/acp-10-10211-2010.

Knote, C., D. Brunner, H. Vogel, J. Allan, A. Asmi, M. Äijälä, S. Carbone, H. D. van der Gon, J. L. Jimenez, A. Kiendler-Scharr, C. Mohr, L. Poulain, A. S. H. Prévôt, E. Swietlicki, and B. Vogel, 2011: Towards an online-coupled chemistry-climate model: evaluation of trace gases and aerosols in cosmo-art. *Geosci. Model Dev.*, **4 (4)**, 1077–1102, doi:10.5194/gmd-4-1077-2011.

Koch, D. and A. D. Del Genio, 2010: Black carbon semi-direct effects on cloud cover: review and synthesis. *Atmos. Chem. Phys.*, **10 (16)**, 7685–7696, doi:10.5194/acp-10-7685-2010.

Köhler, H., 1936: The nucleus in and the growth of hygroscopic droplets. *Trans. Faraday Soc.*, **32**, 1152–1161.

Koop, T., B. P. Luo, A. Tsias, and T. Peter, 2000: Water activity as the determinant for homogeneous ice nucleation in aqueous solutions. *Nature*, **406 (6796)**, 611–614, doi:10.1038/35020537.

Koren, I. and G. Feingold, 2011: Aerosol-cloud-precipitation system as a predator-prey problem. *P. Natl. Acad. Sci. USA*, **108 (30)**, 12 227–12 232, doi:10.1073/pnas.1101777108.

Koren, I., G. Feingold, and L. A. Remer, 2010: The invigoration of deep convective clouds over the Atlantic: aerosol effect, meteorology or retrieval artifact? *Atmos. Chem. Phys.*, **10 (18)**, 8855–8872, doi:10.5194/acp-10-8855-2010.

Kraus, E. B. and P. Squires, 1947: Experiments on the stimulation of clouds to produce rain. *Nature*, **159**, 489–491, doi:10.1038/159489a0.

Kumar, P., I. N. Sokolik, and A. Nenes, 2009: Parameterization of cloud droplet formation for global and regional models: including adsorption activation from insoluble ccn. *Atmos. Chem. Phys.*, **9 (7)**, 2517–2532, doi:10.5194/acp-9-2517-2009.

———, 2011: Cloud condensation nuclei activity and droplet activation kinetics of wet processed regional dust samples and minerals. *Atmos. Chem. Phys.*, **11 (16)**, 8661–8676, doi:10.5194/acp-11-8661-2011.

Lebo, Z. J. and J. H. Seinfeld, 2011: Theoretical basis for convective invigoration due to increased aerosol concentration. *Atmos. Chem. Phys.*, **11 (11)**, 5407–5429, doi:10.5194/acp-11-5407-2011.

Levin, Z. and W. R. Cotton, (Eds.) , 2009: *Aerosol Pollution Impact on Precipitation: A Scientific Review*. Springer, Dordrecht, 386 p.

Levin, Z., E. Ganor, and V. Gladstein, 1996: The effects of desert particles coated with sulfate on rain formation in the eastern Mediterranean. *J. Appl. Meteorol.*, **35 (9)**, 1511–1523.

Levine, J., 1950: Statistical explanation of spontaneous freezing of water droplets. Tech. Rep. NACA-TN-2234, National Advisory Committee for Aeronautics.

Li, G., Y. Wang, K.-H. Lee, Y. Diao, and R. Zhang, 2009: Impacts of aerosols on the development and precipitation of a mesoscale squall line. *J. Geophys. Res.-Atmos.*, **114**, D17 205, doi:10.1029/2008JD011581.

Lohmann, U. and K. Diehl, 2006: Sensitivity studies of the importance of dust ice nuclei for the indirect aerosol effect on stratiform mixed-phase clouds. *J. Atmos. Sci.*, **63 (3)**, 968–982.

Lohmann, U. and J. Feichter, 2005: Global indirect aerosol effects: a review. *Atmos. Chem. Phys.*, **5**, 715–737, doi:10.5194/acp-5-715-2005,2005.

Lohmann, U., J. Feichter, C. Chuang, and J. Penner, 1999a: Prediction of the number of cloud droplets in the ECHAM GCM. *J. Geophys. Res.-Atmos.*, **104 (D8)**, 9169–9198, doi:10.1029/1999JD900046.

Lohmann, U. and C. Hoose, 2009: Sensitivity studies of different aerosol indirect effects in mixed-phase clouds. *Atmos. Chem. Phys.*, **9 (22)**, 8917–8934, doi:10.5194/acp-9-8917-2009.

Lohmann, U., N. McFarlane, L. Levkov, K. Abdella, and F. Albers, 1999b: Comparing different cloud schemes of a single column model by using mesoscale forcing and nudging technique. *J. Climate*, **12 (2)**, 438–461, doi:10.1175/1520-0442(1999)012<0438:CDCSOA>2.0.CO;2.

Lowell, S., J. E. Shields, M. A. Thomas, and M. Thommes, 2004: *Characterization of Porous Solids and Powders: Surface Area, Pore Size and Density*, Particle Technology Series, Vol. 16. Kluwer Academic Publishers, Dordrecht, 347 p.

Lundgren, K., 2010: Direct radiative effects of sea salt on the regional scale. Ph.D. thesis, Karlsruhe Institute of Technology, Karlsruhe.

Menzel, W. P., R. A. Frey, H. Zhang, D. P. Wylie, C. C. Moeller, R. E. Holz, B. Maddux, B. A. Baum, K. I. Strabala, and L. E. Gumley, 2008: MODIS global cloud-top pressure and amount estimation: Algorithm description and results. *J. Appl. Meteorol. Clim.*, **47 (4)**, 1175–1198, doi:10.1175/2007JAMC1705.1.

Meyers, M. P., P. J. DeMott, and W. R. Cotton, 1992: New primary ice-nucleation parameterizations in an explicit cloud model. *J. Appl. Meteorol.*, **31 (7)**, 708–721, doi:10.1175/1520-0450(1992)031<0708:NPINPI>2.0.CO;2.

Min, Q. and R. Li, 2010: Longwave indirect effect of mineral dusts on ice clouds. *Atmos. Chem. Phys.*, **10 (16)**, 7753–7761, doi:10.5194/acp-10-7753-2010.

Min, Q.-L., R. Li, B. Lin, E. Joseph, S. Wang, Y. Hu, V. Morris, and F. Chang, 2009: Evidence of mineral dust altering cloud microphysics and precipitation. *Atmos. Chem. Phys.*, **9 (9)**, 3223–3231, doi:10.5194/acp-9-3223-2009.

Möhler, O., S. Buttner, C. Linke, M. Schnaiter, H. Saathoff, O. Stetzer, R. Wagner, M. Kramer, A. Mangold, V. Ebert, and U. Schurath, 2005: Effect of sulfuric acid coating on heterogeneous ice nucleation by soot aerosol particles. *J. Geophys. Res.-Atmos.*, **110 (D11)**, D11 210, doi:10.1029/2004JD005169.

Möhler, O., P. J. DeMott, G. Vali, and Z. Levin, 2007: Microbiology and atmospheric processes: the role of biological particles in cloud physics. *Biogeosciences*, **4 (6)**, 1059–1071.

Möhler, O., P. R. Field, P. Connolly, S. Benz, H. Saathoff, M. Schnaiter, R. Wagner, R. Cotton, M. Krämer, A. Mangold, and A. J. Heymsfield, 2006: Efficiency of the deposition mode ice nucleation on mineral dust particles. *Atmos. Chem. Phys.*, **6 (10)**, 3007–3021, doi:10.5194/acp-6-3007-2006.

Morales, R. and A. Nenes, 2010: Characteristic updrafts for computing distribution-averaged cloud droplet number, autoconversion rate and effective radius. *J. Geophys. Res.*, **115**, D18 220, doi:10.1029/2009JD013233.

Mühlbauer, A. and U. Lohmann, 2009: Sensitivity Studies of Aerosol-Cloud Interactions in Mixed-Phase Orographic Precipitation. *J. Atmos. Sci.*, **66**, 2517–2538, doi: 10.1175/2009JAS3001.1.

Nenes, A., S. Ghan, H. Abdul-Razzak, P. Chuang, and J. Seinfeld, 2001: Kinetic limitations on cloud droplet formation and impact on cloud albedo. *Tellus*, **53 (2)**, 133–149, doi:10.1034/j.1600-0889.2001.d01-12.x.

Nenes, A. and J. Seinfeld, 2003: Parameterization of cloud droplet formation in global climate models. *J. Geophys. Res.-Atmos.*, **108 (D14)**, 4415, doi:10.1029/2002JD002911.

Niedermeier, D., R. A. Shaw, S. Hartmann, H. Wex, T. Clauss, J. Voigtländer, and F. Stratmann, 2011: Heterogeneous ice nucleation: exploring the transition from stochastic to singular freezing behavior. *Atmos. Chem. Phys.*, **11 (16)**, 8767–8775, doi:10.5194/acp-11-8767-2011.

Noppel, H., U. Blahak, K. D. Beheng, and A. Seifert, 2006: A two-moment cloud microphysics scheme with two process-separated modes of graupel. 12. AMS Conference

on Cloud Physics, 10. – 14.7.2006, Madison, Wisconsin, URL http://ams.confex.com/ams/pdfpapers/113532.pdf.

Ntelekos, A. A., J. A. Smith, L. Donner, J. D. Fast, W. I. Gustafson, Jr., E. G. Chapman, and W. F. Krajewski, 2009: The effects of aerosols on intense convective precipitation in the northeastern United States. *Q. J. Roy. Meteor. Soc.*, **135**, 1367–1391, doi:10.1002/qj.476.

Perez, C., S. Nickovic, G. Pejanovic, J. M. Baldasano, and E. Oezsoy, 2006: Interactive dust-radiation modeling: A step to improve weather forecasts. *J. Geophys. Res.-Atmos.*, **111 (D16)**, doi:10.1029/2005JD006717.

Petty, G. W., 2004: *A First Course in Atmospheric Radiation*. Sundog Publishing, Madison, 459 p.

Phillips, V. T. J., P. J. DeMott, and C. Andronache, 2008: An empirical parameterization of heterogeneous ice nucleation for multiple chemical species of aerosol. *J. Atmos. Sci.*, **65 (9)**, 2757–2783, doi:10.1175/2007JAS2546.1.

Pinsky, M., A. Khain, and M. Shapiro, 2001: Collision efficiency of drops in a wide range of Reynolds numbers: Effects of pressure on spectrum evolution. *J. Atmos. Sci.*, **58 (7)**, 742–764, doi:10.1175/1520-0469(2001)058<0742:CEODIA>2.0.CO;2.

Pradelle, F. and G. Cautenet, 2002: Radiative and microphysical interactions between marine stratocumulus clouds and Saharan dust - 2. Modeling. *J. Geophys. Res.-Atmos.*, **107 (D19)**, doi:10.1029/2000JD000156.

Pregger, T., B. Thiruchittampalam, and R. Friedrich, 2007: Ermittlung von Emissionsdaten zur Untersuchung der Klimawirksamkeit von Rußpartikeln in Baden-Württemberg. Final report, IER Universität Stuttgart, Stuttgart.

Pruppacher, H. R. and J. D. Klett, 1997: *Microphysics of Clouds and Precipitation*. 2d ed., Kluwer Academic Publishers, Dordrecht, Boston, London, 954 p.

Quaas, J., Y. Ming, S. Menon, T. Takemura, M. Wang, J. E. Penner, A. Gettelman, U. Lohmann, N. Bellouin, O. Boucher, A. M. Sayer, G. E. Thomas, A. McComiskey,

G. Feingold, C. Hoose, J. E. Kristjansson, X. Liu, Y. Balkanski, L. J. Donner, P. A. Ginoux, P. Stier, B. Grandey, J. Feichter, I. Sednev, S. E. Bauer, D. Koch, R. G. Grainger, A. Kirkevag, T. Iversen, O. Seland, R. Easter, S. J. Ghan, P. J. Rasch, H. Morrison, J. F. Lamarque, M. J. Iacono, S. Kinne, and M. Schulz, 2009: Aerosol indirect effects - general circulation model intercomparison and evaluation with satellite data. *Atmos. Chem. Phys.*, **9 (22)**, 8697–8717, doi:10.5194/acp-9-8697-2009,2009.

Radke, L. F. and P. V. Hobbs, 1991: Humidity and particle fields around some small cumulus clouds. *J. Atmos. Sci.*, **48 (9)**, 1190–1193, doi:10.1175/1520-0469(1991)048<1190:HAPFAS>2.0.CO;2.

Reisner, R. M., J.and Rasmussen and R. T. Bruintjes, 1998: Explicit forecasting of supercooled liquid water in winter storms using the MM5 mesoscale model. *Q. J. Roy. Meteor. Soc.*, **124 (548, Part b)**, 1071–1107, doi:10.1256/smsqj.54803.

Reutter, P., H. Su, J. Trentmann, M. Simmel, D. Rose, S. S. Gunthe, H. Wernli, M. O. Andreae, and U. Pöschl, 2009: Aerosol- and updraft-limited regimes of cloud droplet formation: influence of particle number, size and hygroscopicity on the activation of cloud condensation nuclei (ccn). *Atmos. Chem. Phys.*, **9 (18)**, 7067–7080, doi:10.5194/acp-9-7067-2009.

Riemer, N., B. Vogel, H. Vogel, and F. Fiedler, 2003: Modeling aerosols on the mesoscale-γ: Treatment of soot aerosol and its radiative effects. *J. Geophys. Res.*, **108**, 4601, doi:10.1029/2003JD003448.

Riemer, N., H. Vogel, and B. Vogel, 2004: Soot aging time scales in polluted regions during day and night. *Atmos. Chem. Phys.*, **4 (7)**, 1885–1893, doi:10.5194/acp-4-1885-2004.

Ritter, B. and J. F. Geleyn, 1992: A comprehensive radiation scheme for numerical weather prediction models with potential applications in climate simulations. *Mon. Weather Rev.*, **120 (2)**, 303–325, doi:10.1175/1520-0493(1992)120<0303:ACRSFN>2.0.CO;2.

Roberts, G. C., M. V. Ramana, C. Corrigan, D. Kim, and V. Ramanathan, 2008: Simultaneous observations of aerosol-cloud-albedo interactions with three stacked un-

manned aerial vehicles. *P. Natl. Acad. Sci. USA*, **105 (21)**, 7370–7375, doi:10.1073/pnas.0710308105.

Rosenfeld, D., U. Lohmann, G. B. Raga, C. D. O'Dowd, M. Kulmala, S. Fuzzi, A. Reissell, and M. O. Andreae, 2008: Flood or drought: How do aerosols affect precipitation? *Science*, **321**, 1309–1313, doi:10.1126/science.1160606.

Rosenfeld, D., Y. Rudich, and R. Lahav, 2001: Desert dust suppressing precipitation: A possible desertification feedback loop. *P. Natl. Acad. Sci. USA*, **98 (11)**, 5975–5980, doi:10.1073/pnas.101122798.

Sandu, I., J.-L. Brenguier, O. Geoffroy, O. Thouron, and V. Masson, 2008: Aerosol impacts on the diurnal cycle of marine stratocumulus. *J. Atmos. Sci.*, **65 (8)**, 2705–2718, doi:10.1175/2008JAS2451.1.

Sandu, I., J.-L. Brenguier, O. Thouron, and B. Stevens, 2009: How important is the vertical structure for the representation of aerosol impacts on the diurnal cycle of marine stratocumulus? *Atmos. Chem. Phys.*, **9 (12)**, 4039–4052, doi:10.5194/acp-9-4039-2009.

Schell, B., I. Ackermann, H. Hass, F. Binkowski, and A. Ebel, 2001: Modeling the formation of secondary organic aerosol within a comprehensive air quality model system. *J. Geophys. Res.-Atmos.*, **106 (D22)**, 28 275–28 293, doi:10.1029/2001JD000384.

Seifert, A., 2008: A Revised Cloud Microphysical Parameterization for COSMO-LME. Tech. rep., Deutscher Wetterdienst, Offenbach.

Seifert, A. and K. Beheng, 2001: A double-moment parameterization for simulating autoconversion, accretion and selfcollection. *Atmos. Res.*, **59**, 265–281, doi:10.1016/S0169-8095(01)00126-0.

Seifert, A. and K. D. Beheng, 2006a: A two-moment cloud microphysics parameterization for mixed-phase clouds. Part 2: Maritime vs. continental deep convective storms. *Meteorol. Atmos. Phys.*, **92 (1-2)**, 67–82, doi:10.1007/s00703-005-0113-3.

———, 2006b: A two-moment cloud microphysics parameterization for mixed-phase clouds. part 1: Model description. *Meteorol. Atmos. Phys.*, **92**, 45–66, doi:10.1007/s00703-005-0112-4.

Seifert, A., A. Khain, A. Pokrovsky, and K. D. Beheng, 2006: A comparison of spectral bin and two-moment bulk mixed-phase cloud microphysics. *Atmos. Res.*, **80**, 46–66.

Seifert, A., C. Köhler, and K. D. Beheng, 2011: Aerosol-cloud-precipitation effects over Germany as simulated by a convective-scale numerical weather prediction model. *Atmos. Chem. Phys.*, **11 (7)**, 20 203–20 243, doi:10.5194/acpd-11-20203-2011.

Seifert, P., A. Ansmann, I. Mattis, U. Wandinger, M. Tesche, R. Engelmann, D. Mueller, C. Perez, and K. Haustein, 2010: Saharan dust and heterogeneous ice formation: Eleven years of cloud observations at a central European EARLINET site. *J. Geophys. Res.*, **115**, D20 201, doi:10.1029/2009JD013222.

Seinfeld, J. H. and S. N. Pandis, 2006: *Atmospheric Chemistry and Physics*. 2d ed., John Wiley & Sons, Inc, Hoboken, 1203 p.

Small, J. D., P. Y. Chuang, G. Feingold, and H. Jiang, 2009: Can aerosol decrease cloud lifetime? *Geophys. Res. Lett.*, **36**, L16 806, doi:10.1029/2009GL038888.

Solomos, S., G. Kallos, J. Kushta, M. Astitha, C. Tremback, A. Nenes, and Z. Levin, 2011: An integrated modeling study on the effects of mineral dust and sea salt particles on clouds and precipitation. *Atmospheric Chemistry and Physics*, **11 (2)**, 873–892, doi:10.5194/acp-11-873-2011.

Sorjamaa, R. and A. Laaksonen, 2007: The effect of H2O adsorption on cloud drop activation of insoluble particles: a theoretical framework. *Atmos. Chem. Phys.*, **7 (24)**, 6175–6180.

Sorooshian, A., G. Feingold, M. D. Lebsock, H. Jiang, and G. L. Stephens, 2009: On the precipitation susceptibility of clouds to aerosol perturbations. *Geophys. Res. Lett.*, **36**, L13 803, doi:10.1029/2009GL038993.

———, 2010: Deconstructing the precipitation susceptibility construct: Improving methodology for aerosol-cloud precipitation studies. *J. Geophys. Res.-Atmos.*, **115**, D17 201, doi:10.1029/2009JD013426.

Squires, P., 1958: The microstructure and colloidal stability of warm clouds. 2. The causes of the variations in microstructure. *Tellus*, **10**, 262–271.

Stanelle, T., B. Vogel, H. Vogel, D. Bäumer, and C. Kottmeier, 2010: Feedback between dust particles and atmospheric processes over West Africa during dust episodes in March 2006 and June 2007. *Atmos. Chem. Phys.*, **10 (22)**, 10 771–10 788, doi:10.5194/acp-10-10771-2010.

Stevens, B. and G. Feingold, 2009: Untangling aerosol effects on clouds and precipitation in a buffered system. *Nature*, **461**, 607–613, doi:10.1038/nature08281.

Stockwell, W. R., P. Middleton, J. S. Chang, and X. Y. Tang, 1990: The 2nd generation regional acid deposition model chemical mechanism for regional air-quality modeling. *J. Geophys. Res.-Atmos.*, **95 (D10)**, 16 343–16 367, doi:10.1029/JD095iD10p16343.

Storelvmo, T., J. E. Kristjansson, S. J. Ghan, A. Kirkevag, O. Seland, and T. Iversen, 2006: Predicting cloud droplet number concentration in Community Atmosphere Model (CAM)-Oslo. *J. Geophys. Res.-Atmos.*, **111 (D24)**, D24 208, doi:10.1029/2005JD006300.

Storelvmo, T., J. E. Kristjansson, and U. Lohmann, 2008: Aerosol influence on mixed-phase clouds in CAM-Oslo. *J. Atmos. Sci.*, **65 (10)**, 3214–3230, doi:10.1175/2008JAS2430.1.

Sullivan, R. C., S. A. Guazzotti, D. A. Sodeman, and K. A. Prather, 2007: Direct observations of the atmospheric processing of asian mineral dust. *Atmos. Chem. Phys.*, **7 (5)**, 1213–1236, doi:10.5194/acp-7-1213-2007.

Thomson, W. L. K., 1871: On the equilibrium of vapour at a curved surface of liquids. *Phil. Mag.*, **42**, 448.

Tonttila, J., E. J. O'Connor, S. Niemela, P. Raisanen, and H. Jarvinen, 2011: Cloud base vertical velocity statistics: a comparison between an atmospheric mesoscale model and remote sensing observations. *Atmos. Chem. Phys.*, **(17)**, 9207–9218, doi:10.5194/acp-11-9207-2011.

Twohy, C., M. Petters, J. Snider, B. Stevens, W. Tahnk, M. Wetzel, L. Russell, and F. Burnet, 2005: Evaluation of the aerosol indirect effect in marine stratocumulus clouds: Droplet number, size, liquid water path, and radiative impact. *J. Geophys. Res.-Atmos.*, **110 (D8)**, D08 203, doi:10.1029/2004JD005116.

Twohy, C. H., C. F. Clement, B. W. Gandrud, A. J. Weinheimer, T. L. Campos, D. Baumgardner, W. H. Brune, I. Faloona, G. W. Sachse, S. Vay, and D. Tan, 2002: Deep convection as a source of new particles in the midlatitude upper troposphere. *J. Geophys. Res.-Atmos.*, **107 (D21)**, 4560, doi:10.1029/2001JD000323.

Twomey, S., 1959: The nuclei of natural cloud formation part ii: The supersaturation in natural clouds and the variation of cloud droplet concentration. *Pure Appl. Geophys.*, **43**, 243–249, doi:10.1007/BF01993560.

———, 1974: Pollution and the planetary albedo. *Atmos. Environ.*, **8 (12)**, 1251–1256, doi:10.1016/0004-6981(74)90004-3.

———, 1977: Influence of pollution on shortwave albedo of clouds. *J. Atmos. Sci.*, **34 (7)**, 1149–1152, doi:10.1175/1520-0469(1977)034<1149:TIOPOT>2.0.CO;2.

Twomey, S. and P. Squires, 1959: The influence of cloud nucleus population on the microstructure and stability of convective clouds. *Tellus*, **11**, 408–411.

van den Heever, S. C., G. G. Carrio, W. R. Cotton, P. J. DeMott, and A. J. Prenni, 2006: Impacts of nucleating aerosol on Florida storms. Part I: Mesoscale simulations. *J. Atmos. Sci.*, **63 (7)**, 1752–1775, doi:10.1175/JAS3713.1.

Vogel, B., H. Vogel, D. Bäumer, M. Bangert, K. Lundgren, R. Rinke, and T. Stanelle, 2009: The comprehensive model system COSMO-ART - Radiative impact of aerosol on the state of the atmosphere on the regional scale. *Atmos. Chem. Phys.*, **9 (22)**, 8661–8680, doi:10.5194/acp-9-8661-2009.

Waliser, D. E., J. L. F. Li, T. S. L'Ecuyer, and W. T. Chen, 2011: The impact of precipitating ice and snow on the radiation balance in global climate models. *Geophys. Res. Lett.*, **38**, L06 802, doi:10.1029/2010GL046478.

Wegener, A., 1911: *Thermodynamik der Atmosphäre*. J. A. Barth, 311 p.

Weigelt, A., M. Hermann, P. F. J. van Velthoven, C. A. M. Brenninkmeijer, G. Schlaf, A. Zahn, and A. Wiedensohler, 2009: Influence of clouds on aerosol particle number concentrations in the upper troposphere. *J. Geophys. Res.-Atmos.*, **114**, D01 204, doi:10.1029/2008JD009805.

Whitby, E. and P. McMurry, 1997: Modal aerosol dynamics modeling. *Aerosol Sci. Tech.*, **27 (6)**, 673–688, doi:10.1080/02786829708965504.

Whitby, K., 1978: The physical characteristics of sulfur aerosols. *Atmos. Environ.*, **12 (1)**, 135–159, doi:10.1016/0004-6981(78)90196-8.

Wiacek, A., T. Peter, and U. Lohmann, 2010: The potential influence of asian and african mineral dust on ice, mixed-phase and liquid water clouds. *Atmos. Chem. Phys.*, **10 (18)**, 8649–8667, doi:10.5194/acp-10-8649-2010.

Wood, R., 2007: Cancellation of aerosol indirect effects in marine stratocumulus through cloud thinning. *J. Atmos. Sci.*, **64 (7)**, 2657–2669, doi:10.1175/JAS3942.1.

Yin, Y. and L. Chen, 2007: The effects of heating by transported dust layers on cloud and precipitation: a numerical study. *Atmos. Chem. Phys.*, **7 (13)**, 3497–3505, doi:10.5194/acp-7-3497-2007.

Zhang, Y., 2008: Online-coupled meteorology and chemistry models: history, current status, and outlook. *Atmos. Chem. Phys.*, **8 (11)**, 2895–2932, doi:10.5194/acp-8-2895-2008.

Zhang, Y., X.-Y. Wen, and C. J. Jang, 2010: Simulating chemistry-aerosol-cloud-radiation-climate feedbacks over the continental US using the online-coupled Weather Research Forecasting Model with chemistry (WRF/Chem). *Atmos. Environ.*, **44**, 3568–3582, doi:10.1016/j.atmosenv.2010.05.056.

Zubler, E. M., D. Folini, U. Lohmann, D. Luethi, C. Schaer, and M. Wild, 2011a: Simulation of dimming and brightening in Europe from 1958 to 2001 using a regional climate model. *J. Geophys. Res.-Atmos.*, **116**, D18 205, doi:10.1029/2010JD015396.

Zubler, E. M., D. Folini, U. Lohmann, D. Lüthi, A. Muhlbauer, S. Pousse-Nottelmann, C. Schär, and M. Wild, 2011b: Implementation and evaluation of aerosol and cloud microphysics in a regional climate model. *J. Geophys. Res.-Atmos.*, **116**, D02 211, doi:10.1029/2010JD014572.

B. Symbols

Indices

w	water
v	water vapor
cloud hydrometeors	
c	cloud water
r	rain
i	cloud ice
s	snow
g	graupel
h	hail
aerosol particles	
a	total aerosol
if	inernally mixed Aitken mode
jf	internally mixed Accumulation mode
ic	internally mixed Aitken mode with soot core
jc	internally mixed accumulation mode with soot core
so	soot
da	smallest dust mode
db	medium dust mode
dc	largest dust mode
sa	smallest sea salt mode
sb	medium sea salt mode
sc	largest sea salt mode

Variables

α $= \frac{l_{wv}M_w g}{c_p RT^2} - \frac{gM_a}{RT}$

α_c accommodation coefficient

α_i $= \frac{l_{iv}M_w g}{c_p RT^2} - \frac{gM_a}{RT}$

α_w water activity

β precipitation susceptibility

$\beta_{e,x}$ extinction coefficient of x

$\beta_{x/y}$ rate at which a critical cluster (phase x) gains a molecule by collision with molecules of phase y

Δs_{char} $= \min\left[\left(\frac{d\ln N_{\text{het}}(s_i)}{ds_i}\right)^{-1}, s_i\right]$

Δs^*_{char} $= \frac{\Delta s_{\text{char}}\left[\frac{4}{3}\Delta s_{\text{char}} + 2(s_i - \Delta s_{\text{char}})\right]}{(1 + s_i - \Delta s_{\text{char}})}$

Δ $= \left(s^4_{\max} - \frac{16A\alpha w}{9\Lambda}\right)$ (Nenes and Seinfeld, 2003)

$\delta^b_a(y, y_1, y_2)$ equals a at $y \leq y_1$ and equals b for $y \geq y_2$ with a cubic interpolation in between ($y_1 < y < y_2$)

ε_i insoluble volume fraction of a particle, $\varepsilon_i = V_i/V_p$

ε_s soluble volume fraction of a particle, $\varepsilon_s = 1 - \varepsilon_i$

ε_s soluble volume fraction of a particle

γ $= \frac{pM_a}{e^\circ M_w} + \frac{l^2_{wv}M_w}{c_p RT^2}$

γ_i $= \frac{pM_a}{e^\circ_i M_w}\left(+\frac{l^2_{iv}M_w}{c_p RT^2}\right)$

κ	proportionality constant of w_{PDF} and TS
Λ	$= 4\left(\frac{\rho_w RT}{e^{\circ} D_v' M_w} + \frac{l_{wv}\rho_w}{k_a T}\left(\frac{l_{w,v} M_w}{TR} - 1\right)\right)^{-1}$
λ	$= \sqrt{\frac{\Lambda_{i,1}}{\alpha_i w \Lambda_{i,2}^2}}$
Λ_i	$= \frac{1}{\Lambda_{i,1} D^2 + \Lambda_{i,2} D}$
$\overline{\Lambda_i}$	effective Λ_i for ice crystal growth (Barahona and Nenes, 2008, Eq. 25)
$\Lambda_{i,1}$	$= \frac{\rho_i RT}{4 e_i^{\circ} D_v M_w} + \frac{l_{iv}\rho_i}{4 k_a T}\left(\frac{l_{iv} M_w}{TR} - 1\right)$
$\Lambda_{i,2}$	$= \frac{\rho_i RT}{2 e_i^{\circ} M_w \alpha_d}\sqrt{\frac{2\pi M_w}{RT}}$
μ	cosine of the solar zenith angle
μ_x	chemical potential of component x
$\mu_x^{\diamond}$	standard chemical potential of x
$\overline{\nu_s}$	average dissociation factor of the soluble particle fraction
ν_s	dissociation factor of a solute
Ω_c	diameter of the collision cross section formed by the grazing tracks of two falling drops
Ω_x	baseline surface area mixing ratios given in (Phillips et al., 2008)
ω_x	single scattering albedo of x
$\overline{\rho_s}$	average density of the soluble particle fraction
ρ_x	density of x
σ_x	geometrical standard deviation of mode x
$\sigma_{x,y}$	surface tension of the x–y interface
τ	point in time when the critical supersaturation of a particle is reached.
τ_x	optical depth of x

Θ number of adsorbed layers of water molecules

υ_x mole volume of x

ξ $\delta_1^0(T, 268.15, 271.15)$

A $= \frac{4\sigma_{v,w}M_w}{RT\rho_w}$

a constant in the CCN spectrum of Twomey (1959)

A_{FHH} empirical constant in FHH adsorption theory

B $= \frac{\nu_s D_p^3 \rho_s M_w}{\rho_w M_s}$

b constant in the CCN spectrum of Twomey (1959)

B_{FHH} empirical constant in FHH adsorption theory

C empirical constant depending on A_{FHH} and B_{FHH}

c exponent depending on the hygroscopicity of a particle

c_p specific heat capacity of air

$\mathrm{CCN}(s)$ CCN spectrum of an aerosol population

D diameter of an aerosol droplet

$\overline{D_{p,x}}$ median diameter of the dry number size distribution function of mode x

$\hat{D}_w$ diameter of a water molecule

$\overline{D_{\mathrm{sat}}}$ mean droplet diameter at saturation of particles with $s_{\mathrm{crit}} < s_{\mathrm{part}}$

D^* droplet/cluster diameter at the maximum of ΔG

D_p dry diameter of a particle

D_v diffusivity of water vapor in air neglecting non-continuum effects

D_v' diffusivity of water vapor in air onto a droplet

D_{crit} critical droplet diameter for activation, $D_{\mathrm{crit}} = D(s_{\mathrm{crit}})$

E	collection efficiency
e	water vapor pressure
e°	water vapor pressure in chemical equilibrium with a water surface
e_s°	water vapor pressure in equilibrium with a solution droplet
$e^{\diamond}$	standard water vapor pressure, $e^{\diamond} = 1013.25\,\mathrm{hPa}$
e_{eq}	water vapor pressure in equilibrium with a water droplet
$\mathbf{F_y}$	turbulent flux of $y = \{N_x, m_x\}$ of x
f_x	geometric factor for heterogeneous nucleation of x
G	Gibbs free energy
$\Delta G^*_{x,y}$	Gibbs free energy change accompanying the formation of a cluster (phase$x$) with diameter D^* in phase y
$\Delta G^{\ddagger}$	Change in Gibbs-free energy associated with breaking the water-water- bounds and formation of water-ice- bounds
g_x	asymmetry factor of x
h	Planck's constant
$h(i,j)$	terrain slope parameter at gridpoint (i,j)
h_x	$= 0.5\delta_1^{h_x^{\diamond}}(T, T_0^x, T_0^x + \Delta T)\delta_0^1(S_i, S_{i,0}^x, S_{i,0}^x + \Delta S_i)$, $h_x^{\diamond}$, T_0^x, and $S_{i,0}^x$ are given in (Phillips et al., 2008)
$H_x(s_i, T)$	$= \min\left(h_x + (1-h_x)\delta_0^1[S_w(S_i,T), S_{w,0}, 1], 1\right)$ (Phillips et al., 2008)
$I(x,y)$	condensation integral, where the parameters in the parentheses indicate the supersaturation limits of the integration
$I_{\mathrm{FHH}}(0, s_{\max})$	contribution of activated insoluble particles to the condensation integral
J_x	nucleation rate of x per unit time and per unit volume

k	Boltzmann constant
k_a	thermal conductivity of air
K_c	collection kernel
k_e	mass specific extinction coefficient
k_{hom}	$= \ln \frac{J_{\text{hom}}(s_{\text{hom}})}{J_{\text{hom}}(s_i)} (s_{\text{hom}} - s_i)^{-1}$, J_{hom} from Koop et al. (2000)
$l_{x,y}$	latent heat of phase change (x to y)
LWP	liquid water path of clouds
$\acute{m}_c$	mass of a single cloud drop
$\dot{m}_x$	mass of a single molecule of x
$\overline{m}_i^{\max}$	maximum mean ice crystal mass in the COSMO cloud scheme
$\overline{M_s}$	average molar mass of the soluble particle fraction
M_x	molar mass of x
m_x	mass concentration of x
M_y^x	y-th moment of the number density size distribution of x
$\dot{N}$	total number concentration of molecules in a system
$\dot{N}^{\ddagger}$	number of water molecules in contact with unit area of the ice surface
$\dot{N}_s$	number of water molecules in contact with unit area of a solid aerosol particle
$N^{\diamond}$	$= \sqrt{2}(\alpha_i w \Lambda_{i,1})^{3/2} \left(\gamma_i \frac{\pi}{2} \frac{\rho_i}{\rho_a}\right)^{-1}$
$N^e_{x/y}$	number concentration of molecule clusters (phase x) in a metastable equilibrium with phase y, $\Delta G_{x/y} = \Delta G^*_{x/y}$
N_0^i	$= 100\,\text{m}^{-3}$
n_β	relative distribution function of β

N_i^*	number concentration of nucleating ice crystals
N_x	number concentration of x
n_x	number of moles of component x
N_{het}	number concentration of ice crystals formed by heterogeneous freezing
$N'_{\text{het}}(s_i, T)$	base heterogeneous freezing spectrum used in Phillips et al. (2008)
N_{hom}	number concentration of ice crystals formed by homogeneous freezing
N_{lim}	IN concentration that completely inhibits homogeneous nucleation
N_{sat}	number concentration of droplets with $s_{\text{crit}} < s_{\text{part}}$
n_{w}	distribution of vertically averaged grid-scale vertical velocities inside cloud
$n_{N,c}(\acute{m}_c)$	droplet number mass distribution
$n_N(D_p)$	number density size distribution
$n_N^*(s_{\text{crit}})$	number density distribution with respect to s_{crit})
O_x	surface concentration of x
p	air pressure
P_1	$= \frac{2A}{3}\left(\frac{\alpha w}{\Lambda}\right)^{\frac{1}{2}}$ (Abdul-Razzak and Ghan, 2000)
$P_{2,x}$	$=\frac{(\alpha w/\Lambda)^{\frac{3}{2}}}{2\pi\rho_w\gamma N_x}$ (Abdul-Razzak and Ghan, 2000)
$P_{3,x}$	$= 0.5e^{(2.5\ln^2\sigma_x)}$ (Abdul-Razzak and Ghan, 2000)
$P_{4,x}$	$= 1 + 0.25\ln\sigma_x$ (Abdul-Razzak and Ghan, 2000)
Q_e	extinction efficiency
R	universal Gas constant
r_x	radius of x
$r_{x,\text{eff}}$	effective radius of a distribution of x

S	saturation ratio of air with respect to water, $S = e/e^{\circ}$
s	supersaturation of air with respect to water
$S^{\text{rim}}_{m_c}$ $s+c \rightarrow s$	rate of change of m_c due to collection of cloud water by snow (riming)
$\overline{s_{crit,x}}$	critical supersaturation for activation of a particle with the median diameter of mode x
$S^{\text{sc}}_{N_c}$ $c \rightarrow c$	rate of change of N_c by self-collection of cloud droplets
$S^{\text{freez}}_{N_c}$ $c \rightarrow i$	rate of change of N_c by freezing of cloud droplets
$S^{\text{au}}_{m_c}$ $c \rightarrow r$	rate of change of m_c due to formation of rain drops by collision and coalescence
$S^{\text{melt}}_{N_c}$ $i \rightarrow c$	rate of change of N_c by melting of ice crystals
$S^{\text{acc}}_{m_c}$ $r+c \rightarrow r$	rate of change of m_c due to accretion of cloud droplets by raindrops
$S^{\text{shed}}_{m_c}$ $s+c \rightarrow r$	rate of change of m_c due to collection of cloud water by wet snow to form rain (shedding)
$S^{\text{coag}^{\circ}}_{N_x}$	rate of change of N_x due to intramodal coagulation
S^{coag}_{y}	rate of change of $y = \{N_x, m_x\}$ due to intermodal coagulation
S^{cond}_{y}	rate of change of m_x due to condensation
S^{conv}_{y}	rate of change of $y = \{N_x, m_x\}$ due to sub-grid-scale convective transport
S^{nuc}_{y}	source rate of $y = \{N_x, m_x\}$ due to nucleation from the gas phase
S^{wash}_{y}	rate of change of $y = \{N_x, m_x\}$ due to particles scavenging by precipitation
S_i	saturation ratio of air with respect to ice
s_i	supersaturation of air with respect to ice
s_{crit}	critical supersaturation of an aerosol droplet with respect to water

S_{eq}	equilibrium saturation ratio of a droplet with respect to water, $S_{\mathrm{eq}} = e_{\mathrm{eq}}/e^{\circ}$
s_{eq}	equilibrium supersaturation of a droplet with respect to water, $s_{\mathrm{eq}} = S_{\mathrm{eq}} - 1$
s_{hom}	homogeneous freezing threshold of the supersaturation with respect to ice
s_{max}	maximum supersaturation of the air reached during cloud formation
s_{part}	partitioning critical supersaturation (Nenes and Seinfeld, 2003)
$s_{i,\mathrm{max}}$	maximum supersaturation of air with respect to ice reached during cloud formation
S_{y_x}	rate of change of y for x due to parameterized processes
T	temperature
T_0	freezing point (273.15 K)
t_c	transmittance of a liquid cloud layer
t_{max}	point in time when the maximum supersaturation is reached
TS	terrain slope parameter
$\mathbf{v}$	three-dimensional wind vector
$\mathbf{v}'$	sub-grid scale component of $\mathbf{v}$
V_i	volume of the insoluble part of a particle
V_p	total particle volume
V_x	volume concentration of x
w	vertical velocity
$\overline{w_x^{\mathrm{sed}}}$	average sedimentation velocity of x
w_{PDF}	center of a PDF of sub-grid scale vertical velocities
Δx	horizontal grid size

x_i	ice mass mixing ratio
x_y	mole fraction of y
y'_x	sub-grid scale component of $y = \{N_x, m_x\}$
z	vertical coordinate
z_{cb}	height of cloud base
z_{ct}	height of the cloud top
$Z_{x/y}$	Zeldovich factor for the nucleation of phase x in phase y

Acknowledgment

I would like to express my gratitude to my supervisor Prof. Christoph Kottmeier for his constant support and mentoring. Likewise, I am very grateful to Prof.Thomas Leisner for kindly accepting to co-supervise this thesis.

I am deeply grateful to Bernhard Vogel for supporting me in so many ways. His positive energy and scientific curiosity encouraged me a lot during the last years. I am very grateful to Heike Vogel, especially for always taking time to help me. I want to thank you both for creating a motivating and warm atmosphere at every working day. Without you this thesis would not exist.

I want to thank Kristina Lundgren, Andrew Ferrone and all other members of our working group for the fruitful scientific and non-scientific discussions. Many thanks to Samiro Khodayar for the nice time during we shared the office, Gabi for her kind support with the technical equipment, Julia Keller for her support during the last weeks, Christian Grams, Romi Sasse, and all other colleagues at the institute for creating a kind atmosphere. I want to thank Christoph Knote for the good collaboration and the support.

I am deeply grateful to Prof. Athanasios Nenes and his group for the fruitful collaboration and for having a great time at Georgia Tech. Special thanks to Alexandra Tsimpidi and Vlassis Karydis for the great trip to Chicago and the opportunity to experience a wonderful Greek wedding. Many thanks to Donifan Barahona for the scientific discussions and his support with the ice nucleation parameterization.

I am very grateful to Axel Seifert (DWD) and Ulrich Blahak (DWD) for their support with the cloud microphysics. I thank H. Flentje (DWD) for providing the PM10 measurement data and U. Damrath (DWD) for providing the forecast validation information. I gratefully acknowledge E. Zubler (ETH) for providing the code for the improved parametrization of cloud optical properties, and R. Frey (UW-Madison) for his information on the MODIS cloud product.

I am very grateful to the Karlsruhe House of Young Scientists at KIT for the financial support of a 3-month research stay in the USA (Auslandsaufenthalt wurde vom Karlsruhe House of Young Scientists (KHYS) gefördert)

Finally, I wish to thank my family and especially my wife Julika for their love, support, patience and understanding.

Karlsruhe, May 2012 *Max Bangert*